

**UNIVERSITÀ DEGLI STUDI DI GENOVA**



---

**DIME - DIPARTIMENTO DI INGEGNERIA MECCANICA, ENERGETICA, GESTIONALE E  
DEI TRASPORTI**

**DOTTORATO DI RICERCA IN INGEGNERIA DELLE MACCHINE E DEI SISTEMI  
PER L'ENERGIA, L'AMBIENTE E I TRASPORTI**

**CURRICULUM: INGEGNERIA DELLE MACCHINE E DEI SISTEMI PER L'ENERGIA,  
L'AMBIENTE E LA PROPULSIONE**

## **Tesi di Dottorato**

***Progettazione multidisciplinare ottimizzata nelle  
microturbine a gas***

Tutor: Prof. Ing. Pietro Zunino  
Prof. Ing. Massimiliano Avalor  
Prof. Ing. Margherita Monti

Autore: Andrea Perrone

---

# UNIVERSITÀ DEGLI STUDI DI GENOVA



---

**DIME - DIPARTIMENTO DI INGEGNERIA MECCANICA, ENERGETICA, GESTIONALE E  
DEI TRASPORTI**

DOTTORATO DI RICERCA IN INGEGNERIA DELLE MACCHINE E DEI SISTEMI  
PER L'ENERGIA, L'AMBIENTE E I TRASPORTI

CURRICULUM: INGEGNERIA DELLE MACCHINE E DEI SISTEMI PER L'ENERGIA,  
L'AMBIENTE E LA PROPULSIONE

## **Ph. D. Thesis**

***Optimized multidisciplinary design in micro-gasturbines***

Tutor: Prof. Ing. Pietro Zunino  
Prof. Ing. Massimiliano Avalor  
Prof. Ing. Margherita Monti

Candidate: Andrea Perrone

---

## Sommario

1	Nomenclature .....	6
2	Introduction .....	11
2.1	Type of fuels .....	12
2.2	Micro-gas turbine .....	13
2.2.1	Commercial powerplants .....	14
3	Thermodynamic cycle .....	19
4	Combustion chamber .....	23
4.1	Preliminary design procedure .....	24
4.2	Primary zone analysis .....	25
4.3	Cooling and dilution zone .....	25
4.4	Injector .....	25
5	Recuperator .....	27
5.1	Recuperator configuration choice .....	27
5.2	Recuperator design calculations .....	30
5.3	Results and discussion .....	31
6	Bearings .....	33
6.1	Bearing choice considering operating conditions .....	33
6.2	Bearing external loads .....	34
6.3	Bearing requirements .....	35
6.4	Bearing comparison .....	36
6.4.1	Operating speed .....	37
6.4.2	Operating temperature .....	39
6.5	Load carrying capacity and life .....	41
6.6	Innovative support system .....	45
6.6.1	Layout and components .....	45
6.6.2	Main thrust bearing relief .....	49
6.6.3	Load partition .....	50
6.6.4	Law of load distribution .....	51
6.6.5	Design of the support system .....	53

7	Radial inflow turbine design through multi-disciplinary optimization technique.....	57
7.1	Multidisciplinary optimization .....	57
7.2	Introduction .....	57
7.3	Micro-gas turbine thermodynamic cycle .....	58
7.4	Methodology.....	60
7.4.1	Radial inflow turbine overall performance evaluation.....	60
7.4.2	Preliminary design approach .....	60
7.4.3	3D model parameterization and meshing .....	64
7.5	Optimization strategy.....	67
7.5.1	Aerodynamic optimization process .....	67
7.5.2	Geometrical constraints.....	68
7.5.3	Database generation.....	68
7.5.4	Aerodynamics objective function .....	69
7.6	Structural analysis .....	70
7.6.1	Procedure description .....	70
7.6.2	Thermal analysis .....	70
7.6.3	Thermomechanical analysis.....	71
7.6.4	Modal analysis .....	73
7.7	Results .....	76
8	Multi-disciplinary optimization of a centrifugal compressor for micro-turbine applications.....	83
8.1	Introduction .....	83
8.2	1d design approach.....	85
8.3	Parameterization of the 3d geometrical model.....	87
8.3.1	Meridional channel parameterization .....	87
8.3.2	Impeller row definition .....	89
8.3.3	Diffuser row definition.....	90
8.4	Fluid mesh generation and CFD analysis .....	92
8.5	Solid mesh generation and structural analysis .....	93
8.5.1	Automated solid mesh generation procedure .....	93

8.5.2	Material selection .....	94
8.5.3	Thermomechanical analysis.....	94
8.5.4	Modal analysis .....	95
8.6	Optimization algorithm .....	96
8.6.1	Optimization strategy .....	96
8.7	Results .....	98
9	Global optimization results.....	109
10	Conclusions .....	111
11	Appendix: modal analysis of bladed wheels.....	113
11.1	Theory.....	113
12	References .....	117

# 1 Nomenclature

---

$b$	Channel width [m]
$c$	Absolute velocity [m/s]
$C_1, C_2$	Constant values
$c_p$	Pressure coefficient: $(p_{t1}-p)/(p_{t1}-p_1)$ [dimensionless]
$D$	Diameter[mm]
EDB	Electro Dynamic Bearings
$f$	Equivalence ratio [dimensionless]
$f_{NPF}$	Nozzle passing frequency [Hz]
$f_{ROT}$	Rotation frequency [Hz]
$f_{eigfr}$	Eigenfrequency [Hz]
GT	Gas Turbine
$K$	Load coefficient
$L$	Excitation harmonic number [dimensionless]
$L_{1-2}$	Specific work [J/kg]
$\dot{m}$	Mass flow rate [kg/s]
$m$	Meridional coordinate [m]
$M$	Nodal diameter [dimensionless]
$Ma$	Absolute Mach number [dimensionless]
$Ma_r$	Relative Mach number [dimensionless]
$N$	Rotation speed [rpm]
$n_s$	Specific speed based on machine outlet density
$\bar{n}_s$	Specific speed based on impeller inlet density
$N_{rotor}$	Number of rotor blades

$N_{vane}$	Number of vane blades
$N_{sw}$	Swirl number [dimensionless]
Nu	Nusselt number [dimensionless]
T	Temperature [°C]
TIT	Turbine inlet total temperature [°C]
P	Net power output or aerodynamic load carrying capacity
p	Static pressure [bar]
$P_{Aero}$	Aerodynamic penalty function [dimensionless]
$P_{Freq\_low}$	Low frequency penalty function [dimensionless]
$P_{Freq\_high}$	High frequency penalty function [dimensionless]
$P_{\dot{m}}$	Mass flow rate penalty function [dimensionless]
$P_{MAX\alpha_{OUT,i}}$	Maximum outlet relative flow angle penalty function [dimensionless]
$P_{Struc}$	Structural penalty function [dimensionless]
$P_{MIN\alpha_{OUT,i}}$	Minimum outlet relative flow angle penalty function [dimensionless]
$P_{MAX\eta_{t-t}}$	Total to total efficiency penalty function [dimensionless]
$P_{Stress}$	Stress penalty function [dimensionless]
$P_{\eta_{is\ tt}}$	Efficiency penalty function
$P_{\beta_{tt}}$	Total pressure ratio penalty function
R, r	Radius [m]
Re	Reynolds number [dimensionless]
s	Flame speed [m/s]
S'	Sommerfeld modified number
U	Peripheral speed [m/s]
V	Velocity [m/s]
$W_t$	Total external load

$\omega$	Rotation speed [m/s]
$W$	Weight term for penalty function [dimensionless]
$y^+$	Dimensionless wall distance

*Greeks*

$\alpha$	Absolute flow angle [deg]
$\beta$	Relative flow angle from axial [deg]
$\beta_t$	Pressure ratio [dimensionless]
$\beta_b$	Impeller metallic angle [deg]
$\delta$	Displacement thickness [m]
$\eta$	Efficiency [dimensionless]
$\rho$	Density [kg/m <sup>3</sup> ]
$\mu$	Dynamic viscosity [MPa]
$\delta_v$	Weight term referred to value v [dimensionless]
$\Delta x$	Machine axial width [m]
$\gamma$	Camber angle from axial [deg]
$\vartheta$	Tangential coordinates [rad]
$\rho$	Density [kg/m <sup>3</sup> ]
$\psi$	Loading coefficient [dimensionless]
$\sigma$	Stress [MPa]

*Subscripts*

0	Standard value
A	Air
A <sub>d</sub>	Dilution air

$A_p$	Primary zone air
A	Axial
F	Fuel
G	Global
L	Laminar
t	Turbolent or tangential
t-t	Total to total
Turb	Turbine
y	Yielding
0	Referred to stator inlet section
1'	Referred to stator outlet section
1	Referred to rotor inlet section
2	Referred to rotor outlet section
<i>all</i>	Allowable
<i>eig</i>	Referred to eigenfrequencies
<i>exc</i>	Exciting
<i>max</i>	Maximum
<i>min</i>	Minimum
out	Referred to rotor outlet section
<i>ref</i>	Reference
stress	Von Mises stress
$t - t$	Total to total
<i>b</i>	Blade
<i>i</i>	Inner
<i>o</i>	Outer

<i>r</i>	Rotor
<i>v</i>	Vane

### Acronyms

AMB	Active Magnetic Bearing
ANN	Multi Layer Perceptron Artificial Neural Network
CFD	Computational Fluid Dynamics
CHP	Combined Heat and Power
DoE	Design of Experiments
EO	Engine Order
FEA	Finite Element Analysis
GA	Genetic Algorithm
MGT	Micro gas turbine
NPF	Nozzle Passing Frequency
PMB	Passive Magnetic Bearing
RANS	Reynolds Averaged Navier-Stokes
STL	STereoLithography
URANS	Unsteady Reynolds Averaged Navier-Stokes

## 2 Introduction

---

The distributed generation of energy is becoming more and more interesting from the economical and environmental point of view for the possibility of installing, nearby the site of use, small generation units that can provide at the same time electric and thermal energy that can be used directly for civil heating, cooling or for industrial processes. This is called microcogeneration. In a few words, three fundamental characteristics of the microcogeneration are:

- long, heavy, expensive, environmentally impacting high voltage electric grid are avoided;
- efficient use of fuel with more than 30% (state of the art) electric energy plus more than 45% of thermal energy from the 100% fuel chemical energy. Large global energy generated for 1 kg of  $CO_2$  produced;
- location of the small generation units in proximity of the civil, rural or industrial settlements requires low pollution combustion. Small GT units with gaseous fuel premixed combustion guarantee low emissions.

In the last years micro gas turbines used in cogeneration power plants have been proved to be a promising technical solution for distributed combined production of electricity and heat, especially due to their low emissions and fuel flexibility. In fact the main characteristics of this kind of power plants are:

- Large global efficiency ( $\eta_G > 75\%$ )
- Very low emissions ( $NO_x < 15$  ppm,  $CO < 15$  ppm)
- Long useful life ( $> 60.000$  hours)
- Simple installation
- Simple maintenance
- Simple operation
- Simple and remote control
- High reliability

An effort should be made to improve performance of the micro-gas turbine in order to enhance plant efficiency, taking it closer to other technologies widely employed in this field. In particular, components efficiency heavily affects plant performance and aerodynamic design of novel geometries has to consider mechanical constraints in order to pursue this target without compromising machine integrity [1], [2].

## 2.1 Type of fuels

At present, the world's energy demand is 90% satisfied by the use of non-renewable fossil fuels. These primary energy sources have been used since the times of the industrial revolution with increasing demand. At the same time, the greater awareness of institutions and large industrial groups about environmental issues and sustainability has led to large capital investment in the research and development of alternative systems, so as to get rid of the ever-increasing costs of primary energy and ensure a sustainable energy supply model.

Given these assumptions, the first horizon that offers the concrete possibility of lowering consumption and emissions is the use of natural gas which, although non-renewable, is cleaner than other hydrocarbons. Technological development for commercial purposes of new highly performing machines has led to a re-evaluation of gas for energy production. This type of fuel is already widely used in large thermal power plants, usually with a net power output greater than 10 MW. In this application field, the use of Brayton-Joule gas cycles has reached significant efficiency thresholds. For example, the first developed gas turbine models were just self-evolving, while nowadays gas turbine systems in combined cycles are able to reach up to 60%.

This kind of machines have high performance, but also a high cost of management, installation and maintenance. The answer to the problem of the cost of installation and production has been found in the technological evolution of the components that has led to the appearance on the market of gas turbine plants of smaller size and weight and therefore suitable for use in scenarios with more modest demands than the previous ones. They keep high performance thresholds and sustainable operating costs. On these assumptions, the development of micro- gas turbine for energy production has been increasing in the last 50 years with increasing speed, as evidenced by the rate of increase in the use of natural gas as fuel.

Indeed, the power generated by naturally-fueled gas turbine in Europe is undoubtedly growing, starting from around 570 GW in 1999 to 2035 GW in 2020, with an increase of 6% per year. Whether it is usual to replace more carbon intensive fossil fuels and to use it as reserve capacity to ensure reliable integration of renewable electricity, natural gas is a viable option in the process of gradual decarbonisation of the energy system.

With an increase in consumption by 50%, this source shows the highest growth rate among fossil fuels [3].

## 2.2 Micro-gas turbine

The first studies on this type of technology date back to 1970 and were aimed at the use in the automotive sector for the purpose of replacing the internal combustion engines. The first experiments have been carried out for civil buses. However, the use of micro-gas turbine for such use remained minor for a number of reasons, such as the production costs of propulsion units and their maintenance. With the increase in energy demand between 1980 and 1990, micro-gas turbine studies were resumed in a different perspective with the aim of using them for the production of energy for hybrid vehicles or directly for the production of electricity to the distribution network, according to the increasingly appreciated "distributed generation" scheme.

The first uses for generic purposes date back to 1978 when Allison developed MGT-based generator sets for the power supply of missile raid systems to the US Army. The use of micro-gas turbine proved to be of great logistic validity, as fuel consumption decreased by 180 l/h of traditional diesel generators at only 60 l/h. Together with this benefit, we could notice the actual reduction in noise pollution, operating regime stability and the possibility of using different fuels. The research and evolution of MGT constructive materials was a significant boost because it enabled a much lower weight/power ratio than MCI-based generating sets. Between 1980 and 2000, Allison went ahead with the 200 units installed in 1981 to over 2,000 micro-gas turbine, most of them engaged in the military field to provide power to Patriot-type surface-to-air missiles.

A civil application of the high portability and exploitation of MGT's installations are the numerous installations on mining and processing oil platforms. The isolation of these plants and therefore the need for reliable energy supply is responsive to the use of MGT co-generation plants. High availability of fuel, such as methane gas on site, has made the MGT solution economically very viable for companies. Figure 1 illustrates the installation of a Capstone C30 micro-gas turbine in a natural gas extraction platform in the North Sea. The mining plant uses four 30 kW units as the primary source of energy, having the ability to vary the load of the individual units while they operate in synchrony. Given the hostile scenario for temperatures and salinity, the units are under "marine cold weather".



**Figure 1: gas turbine plant on platform, Wintershall Holding GmbH**

A major boost in the spread of MGT plants was undoubtedly the liberalization of the energy market, which has allowed leading companies in the field of gas generation to increase their growth in the face of increased marketability. These types of plants offer the possibility to attract even small consumers. Indeed, many small and medium-sized industrial establishments could recognize MGTs as a valid alternative to traditional network connectivity, which results in a severe downturn in energy distribution costs.

To date, several companies already offer complete packages consisting of small-medium power plants destined for energy production. Among the companies that have invested more in research and development on micro-gas turbine, we include AlliedSignal, Elliot Energy Systems, Capstone, Ingersoll-Rand Energy System, Turbec, Browman Power, ABB Distributed Generation, Volvo Aero Corporation. Literature suggests that the name "Micro-gas turbine" should be assigned to plants with powers up to 150-300 kWe, reserving to those up to 1 MWe the definition of "Mini- gas turbine ". The following concepts can be found for both categories, which will generally be referred to as Micro- gas turbine, or MGT.

### 2.2.1 Commercial powerplants

Below it is reported an example of MGT machines currently on the market, with their highlights and performance. With the choice of three precise models of three different manufacturers, the aim is to provide an overview of the current offer and evaluate its competitiveness with existing traditional systems.



**Figure 2: commercial micro-gas turbines**

As it can be seen from Figure 2, the size and configuration of these ready-to-operate systems is quite modest when compared with those of others, and this shows the logistic ease of use of MGTs, which are easily transportable on wheels that are on the rail, with very slow handling times. Below, in Table 1, the distinctive features of the systems presented.

	<b>Capstone C600S</b>	<b>Elliot TA100CHP</b>	<b>Ingersoll-Rand MT250</b>
Electric power	<u>600 kW</u>	<u>100 kW</u>	<u>250 kW</u>
Efficiency	33 %	29 %	30 %
Weight	12565 kg	2040 kg	5440 kg
Main dimensions	2,4 x 2,9 x 9,1 m	2,25 x 0,85 x 3,25 m	2,13 x 2,28 x 3,72 m
Emissions	NO <sub>x</sub> @ 15% O <sub>2</sub> 9 pmvd	NO <sub>x</sub> @ 15% O <sub>2</sub> 14 ppmvd	NO <sub>x</sub> @ 15% O <sub>2</sub> 5 ppmvd

**Table 1: performance and general features**

A micro-gas turbine system offers the user the ability to generate electrical or thermal energy or even pushing through a plant type that has high strength portability and operational flexibility without neglecting high performance. The components of these systems are designed to minimize weights and dimensions without having to compromise on reliability, performance, consumption and emissions.

The volumes needed for installation are quantifiable below 6-10 cubic meters per 100 kW installed. This guarantees the possibility of use in the most disparate scenarios, such as the aforementioned offshore mining platforms, mining and mining facilities in isolated areas and generally in all those places that are difficult to reach and thus worse from conventional distribution networks.

The weight reduction of a micro-gas turbine plant compared to a traditional gas turbine is considerable, in the order of thousands of kilograms if the civil engineering works are included in the calculation. An operating and complete auxiliary MGT plant weighs only 16.000 kg in the case of a 600 kW machine, below 3.000 kg for a 100 kW plant (Figure 2 b). At installation this allows a substantial reduction in costs for civil engineering works, contributing to a reduction in the environmental impact of the plant. Not least, noise emissions also fall far below those achieved by traditional machines. A 600 kW plant (Figure 2 a) with its full power emits acoustic noise of only 65 dBA, a value hardly achievable by axial machines due to performance, flow rates and much higher fuel consumption.

The portability feature perfectly blends the "distributed generation" phenomenon, where there is a lack of large production sites in the narrower points of a given network, but there are many small nodes that are both users and manufacturers. The ability to provide energy within a short-term network in both start-up and load-changing conditions also reflects the ability to withstand the most diverse conditions of use. This flexibility is also seen from the point of view of adaptation to the user.

Turbomachines of this type can be used for generating electricity in different ways:

- "stand-alone", at user-set frequency for specialist jobs, usually between 10 and 60 Hz;
- "grid" if one or more units are connected and energize in a wider and branched network;
- "dual-mode", if the system is required to quickly switch from "stand-alone" to "grid";
- "multiple units", if the MGT, connected in parallel with other units, forms a single power node. The load in this case is split between the interconnected units, assigned directly by the integrated electronic control of the plant, or manually by the user for process applications, also based on the cogeneration capacity installable on each unit.

In this regard, it is good to remember that several micro-gas turbines connected in parallel are already in operation. It is interesting to note that network-connected MGTs can use an internal control unit that ensures the appropriate frequency to the network (typically 50/60 Hz) and can make significant variations on the operating mode of the machine itself in order to follow the instantaneous load, or cut the peaks, depending on the user's needs. The integrated control unit also has a protective function for the machine, helping to control its operation so it does not deviate too much from project conditions, where maximum performance is guaranteed. In the case of stand-alone generation, the same internal control unit maintains the voltage constant produced by the machine, ensuring its proper operation without the need for auxiliary plant components. For stand-alone applications, a large built-in battery is provided inside the machine to ensure a number of start-ups without a network connection and at the same time accommodate any transients that may occur during system

setup. In addition to the production of electricity in the form of electricity, it is not uncommon for MGTs to be used for cogeneration cycles or production of electricity together with heat for the operation of industrial plants or even more simply for civilian environmental conditioning.

The use of a micro-gas turbine plant is also interesting to evaluate cogeneration, although the discharge temperature does not exceed 300 ° C. The energy recovery carried out on a 100 kWe plant, can generate a thermal power of 172 kW capable of heating from 40 °C to 60 °C a flow rate of 3.8 l/s of water per industrial applications (Figure 2 b).

In terms of emissions, micro-gas turbine plants are able to comply with the limits imposed by the EU Directive 2009/29/CE with a large, in some cases extremely wide, safety margin in the case of the use of natural gas. All MGT manufacturers guarantee the operation of their machines with different types of fuels, both gaseous as methane and propane, or liquids such as naphtha, kerosene, avio, biodiesel or the less refined diesel. Recently, due to the growing demand for fossil hydrocarbons and the consequent increase in prices, research is being expanded to ensure that MGT plants also work properly with sustainable fuels such as alcohol, ethanol and bio-ethanol from renewable sources treatment of organic waste and biomass, or even fermentation of agricultural waste. In these latest operating conditions, there is an increase in emissions compared to those measured using natural gas, but the absolute value is acceptable. Relevant data regarding fuel is calorific power, whose variation from one fuel to another significantly influences the dynamics and temperatures that can be reached in the combustion chamber. In Table 2 are reported the different values of the lower calorific value of the mentioned fuels.

<b>Metane</b>	50,0 MJ/kg	<b>Propane</b>	46,35 MJ/kg
<b>Natural Gas</b>	47,7 MJ/kg	<b>GPL</b>	46,1 MJ/kg
<b>Kerosene</b>	43,1 MJ/kg	<b>Fuel oil</b>	40,2 MJ/kg
<b>Ethanol</b>	27,1 MJ/kg	<b>Methanol</b>	19,7 MJ/kg
<b>Gasoline</b>	43,6 MJ/kg	<b>Diesel</b>	44,4 MJ/kg

**Table 2: LHV of fuels used in MGT plants**

Many commercial models are offered in different versions to better exploit the possibility of using different fuels.

Although the performance and the aerodynamic characteristics of the machines (turbine and compressor) do not change by varying the type of fuel, more attention is required to the combustors, which certainly need to be adapted to the injection mode and ignition when forced to work with different fuels for viscosity and density. These parameters mainly affect the diffusion rate of the flame front inside the combustion chamber.

It is estimated that the cost of a micro-gas turbine plant at current date is quantifiable at about \$ 500/kW for installation and has an average operating cost of 45-50 \$/MWh in the face of maintenance intervals every 2000 hr about. Some of the on-trade facilities have already exceeded 25000 hours of operation, including shutdown times for maintenance, which is a very small percentage of this value.

As an example, the installation cost of the MGT Turbec T100 plant dedicated to the cogeneration of 100 kW electric and 165 kW heat as hot water can be quantified in approximately 500.000 € for the complete auxiliary plant and training of operators. All commissioning and testing operations take 2 days, followed by another 2 additional days dedicated exclusively to staff calibration and training (2009 - Turbec).

Other possible use of these plants is for propulsion: small size aircrafts, helicopters or drones, or even heavy terrestrial vehicles, especially military. Recently a project involving the use of MGT units for propulsion on tugboats has been presented. Research in terms of material choice, weight and bulk reduction, increased operational reliability has led to major energy-generating projects for civil vehicles. In 2013 Capstone provided 34 C30 micro-gas turbines that can be plugged into diesel or biodiesel to be used as generators on a US electric bus fleet for US transport.

Finally, micro-gas turbine plants are spreading very rapidly on the market, and industry companies are increasing investment in research and development dedicated to these plants. Many manufacturers, given the multiplicity of intrinsic use of MGTs, offer the consumer not only the generative unit, but also a valuation study on the scope and the actual environmental conditions in which it will operate.

### 3 Thermodynamic cycle

The concept design of the micro-gas turbine starts from the analysis of a regenerative Brayton cycle (Figure 3) suitable for the specific application.

In the present PhD thesis, a micro-gas turbine for CHP application with 100 kW of electric power output has been considered. Relating to fluid-dynamic and thermodynamic parameters such as component efficiencies, total pressure losses, heat transfer and insulation coefficients, several assumptions have to be considered.

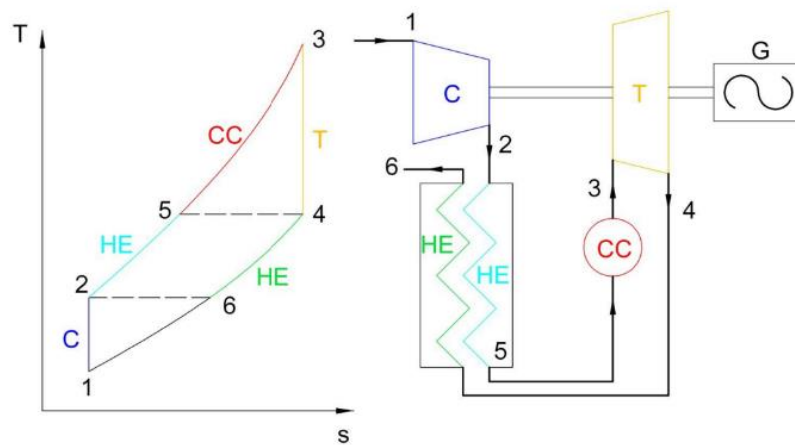


Figure 3: Regenerative Brayton cycle

These parameters were assumed from literature, components datasheets and other scientific papers and are summarized in the Table 3. These values represent the state of the art of a 100 kW micro-gas turbine technology available on the market. The calculations were performed through the open-source in-house developed code GTcycle [3].

Table 3: main cycle parameters for 100kW micro-gas turbine

Parameters	Value
<i>Compressor efficiency</i>	80%
<i>Turbine efficiency</i>	86%
<i>Recuperator effectiveness</i>	84%
<i>Pinch point temperature difference</i>	70 °C
<i>Combustor efficiency</i>	95%

<i>Generator efficiency</i>	96%
<i>Mechanical efficiency</i>	99%
<i>Compressor pressure ratio</i>	4.4
<i>TIT</i>	950°C
<i>Recuperator hot pressure losses</i>	100 mbar
<i>Recuperator cold pressure losses</i>	150 mbar
<i>Combustor pressure losses</i>	175 mbar
<i>Intake pressure losses</i>	10 mbar
<i>Exhaust pressure losses</i>	10 mbar
<i>Cycle Efficiency</i>	30%

The considered cycle has a maximum turbine inlet temperature of  $TIT = 950\text{ }^{\circ}\text{C}$ . The  $TIT$  limit is due to the maximum thermal load that can be faced by nickel-based super-alloys, since the blades are not cooled. For this  $TIT$  a total-to-total pressure ratio of the cycle  $\beta_{t-t\text{ cycle}} = 4.4$  was found to maximize the Brayton-Joule thermodynamic efficiency (see Figure 4). It results in a total-to-total pressure ratio of the turbine of  $\beta_{t-t\text{ turb}} = 3.7$ , once the pressure drop in the combustion chamber as well as in the exhaust duct are considered. Finally, in order to obtain the desired net output power of the system,  $P = 100\text{ kW}_e$ , a target mass flow rate of about  $0.75\text{ kg/s}$  was considered.

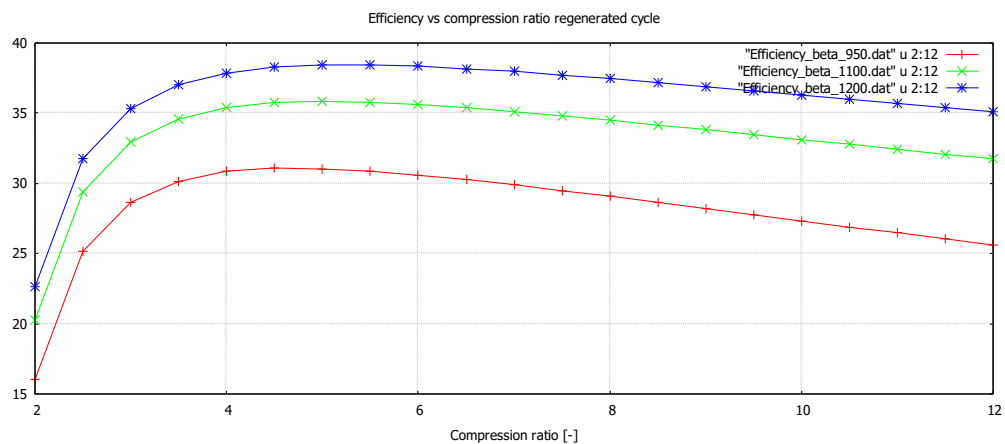
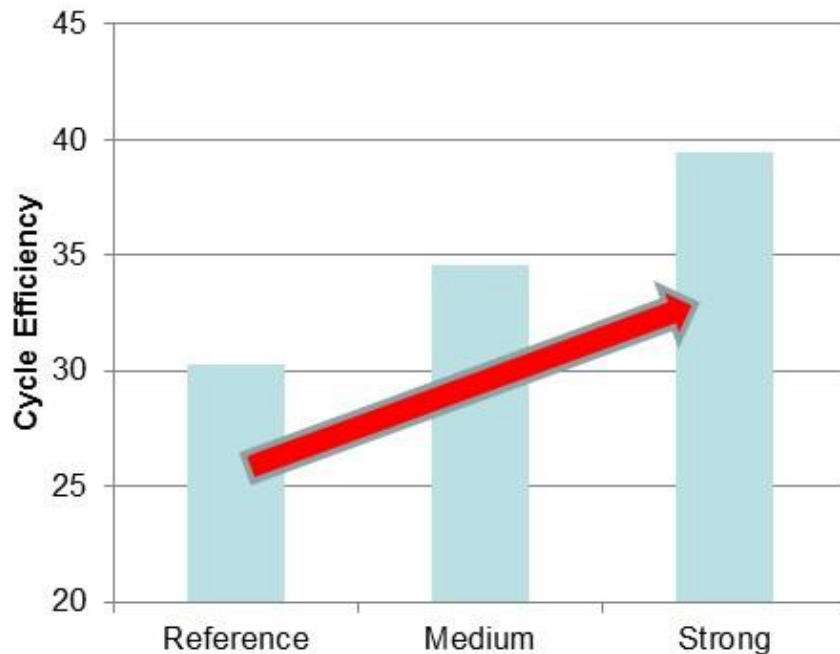


Figure 4: efficiency vs compression ratio @950°C, @1100°C, @1200°C

As reported in the previous table, the efficiency of the thermodynamic cycle is 30%. This value can be improved increasing the TIT over the current technological limit of 950°C due to the use of nickel superalloys. In recent years a great deal of effort has been devoted to research and development of innovative ceramic materials for the manufacturing of turbine impeller in order to increase turbine inlet temperature and, consequently, to enhance the global efficiency.

To overcome this technological limit, advanced heat transfer techniques are employed both in industrial heavy duty gas turbines and aeroengines. However, there are very few applications of cooled radial impellers, mainly due to manufacturing constraints.

Then, a thorough investigation was carried out in order to highlight the influence of each micro-gas turbine component efficiency variation on the overall cycle efficiency. Figure 5 shows two levels of main components optimization and values are summarized in Table 4.



**Figure 5: Effect of components optimization on cycle efficiency**

Considering compressor and turbine, the results show that the same component efficiency increase leads to different overall cycle efficiency. This is the consequence of the lower specific energy exchange of the compressor with respect to the turbine, with a greater influence of the latter.

**Table 4: Assumed efficiency and effectiveness of components for two levels of optimization**

	<b>Reference</b>	<b>Medium</b>	<b>Strong</b>
<b>Compressor</b>	80%	82%	84%
<b>Turbine</b>	86%	88%	90%
<b>Recuperator</b>	84%	89%	94%

The recuperator effectiveness strongly affects the machine efficiency. Recuperator design has to be a compromise between performance improvement, size and weight constraints.

Finally, a strong optimization of the main components, preserving the same TIT, can lead to efficiency values up to 38%, much higher than the state of the art.

## 4 Combustion chamber

---

The combustion chamber design represents a key point in order to achieve the desired overall performance of the entire micro-gas turbine cogenerative power plant. In order to be adequate to be employed in micro cogenerative power plants, the combustor has to satisfy some fundamental requirements:

- large combustion efficiency and low pollutant emissions;
- combustion stability and reliable ignition;
- low total pressure losses;
- uniform outlet temperature distribution;
- silo type combustion chamber in reverse flow configuration

To achieve the first requirement it is necessary to obtain a complete combustion and exhaust gas free as possible from unburnt fuel UHC, carbon monoxide CO, nitric oxide  $\text{NO}_x$  and smoke. Low efficiency, CO and HC are mainly the result of inadequate residence time in the primary zone of the combustor, while thermal  $\text{NO}_x$  formation is controlled by flame temperature and increases with residence time. Little  $\text{NO}_x$  is formed at temperature below around 1850 K.

Lean premixed combustion significantly decreases flame temperatures and consequently reduces  $\text{NO}_x$  formation. Moreover for lean premixed combustors  $\text{NO}_x$  formation is independent of residence time (since it is a prompt mechanism) and, as a consequence, strong reduction of pollutant emissions is achieved with LP combustors.

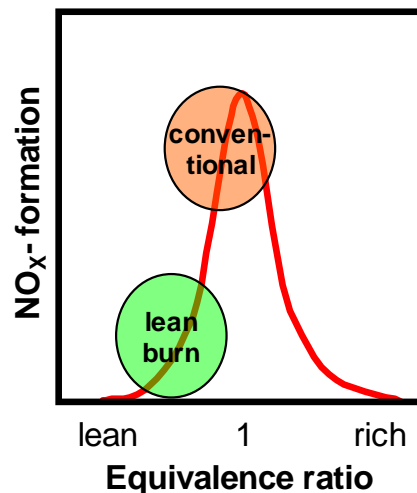


Figure 6: Conventional and lean burn combustion  $\text{NO}_x$  formation

The level of premixing plays a critical role in the performance of the combustor; some considerations have to be done:

- if the premixing duct is too long, the mixture stays in there for a time larger than characteristic ignition time (physical time, for evaporation and mixing + chemical time) with risk of auto ignition and thus combustion in the premixing duct;
- whenever the flame speed exceeds the approach flow velocity, flashback in the premixing ducts can occur;
- if pressure and heat oscillations are phased they may be auto excited and bring to combustor failure due to thermo-acoustical instabilities.

For what concerns the flame stability and reliability of ignition, the combustion must be maintained over a wide range of operating conditions. Combustion must be initiated and sustained in highly turbulent flows that generally have speed greater than the flame speed ( $S_L = 1.3$  m/s for methane stoichiometric mixture at  $T = 900$  K and  $p = 4.5$  bar). A solution can be found by creating a recirculation zone in the primary zone of the liner by means of swirler injectors, where flame speed is enhanced by a high level of turbulence and the recirculating hot products provide heating of the incoming flow at the ignition temperature.

## 4.1 Preliminary design procedure

The first step consists of a combustor preliminary design procedure able to define the fundamental overall conditions and geometrical parameters of the combustor. For the specific application, as reported above, a silo type combustion chamber has been adopted, mainly for simpler maintenance and manufacturing.

From the optimization process of the thermodynamic efficiency of the cycle it is possible to evaluate the air mass flow rate  $\dot{m}_A$ , the inlet thermodynamic pressure  $p$ , and the temperature values  $T_1$  and  $T_2$ . Starting from these values it is possible to evaluate the fuel mass flow rate  $\dot{m}_F$ . A lean premixed burn concept is implemented to obtain low pollutant emissions, with an equivalence ratio of  $f = 0.4-0.5$ . Thus it is possible to calculate the mass flow rate in primary zone,  $\dot{m}_{Ap}$ . The remaining mass flow rate ( $\dot{m}_A - \dot{m}_{Ap}$ ) has to be properly subdivided between cooling  $\dot{m}_{Ac}$  and dilution  $\dot{m}_{Ad}$  mass flow rates. This subdivision has to take into account from one side that the amount of air needed for cooling depends on the maximum temperature in the primary zone, cooling technology and liner material, and from the other side that the dilution air has to enable uniform exit temperature distribution.

## 4.2 Primary zone analysis

In order to obtain a low total pressure loss and at the same time an high flame stability, the mean velocity of the flow within the primary zone is assumed to be of about 15-20 m/s. From this assumption it is possible to evaluate the liner diameter. In addition, the primary zone length has to enable the complete combustion of fuel for each operating condition. As a consequence, by imposing that the primary zone residence time has to be higher than the burning time, it is possible to obtain the primary zone length.

Furthermore, in order to allow flame stability by means of an adequate recirculation zone, the injectors must provide a proper swirl number, defined as:

$$N_{sw} = \frac{\int \rho v_a v_t r^2 dr}{R \int \rho v_a^2 r dr} \quad (1)$$

## 4.3 Cooling and dilution zone

Rows of cooling holes generate jets through the liner to keep the temperature lower than the maximum allowable value, while dilution holes provide the desired exit mean temperature and temperature uniform distribution. Hole number, diameters and disposition must be evaluated and optimized. A first guess solution, however, can be found by applying the simplified relation suggested by [4].

## 4.4 Injector

A lean premixed flame with a small diffusion flame region in order to provide flame stability at part-load conditions can be chosen. Air and fuel for lean premixed flame are injected through the external swirler, while air for pilot diffusion flame is injected through the internal swirler. In order to obtain an higher flame stability co-rotating swirlers are employed. By imposing an overall swirl number  $N_{sw} > 0.5$  a swirler exit flow angle higher than 30 degree is obtained. In conclusion the overall requirements of the injection system are:

- turbulence intensity higher than 15% in order to enhance the mixing process;
- residence time lower than autoignition time to avoid ignition in the premixing duct;
- flow velocity in premixing duct higher than turbulent flame speed  $S_t$ ;
- avoiding recirculation zones in the premixing duct.

By following the assumptions listed before, a first guess geometry for the can combustor can be obtained. In Figure 7, an overall view of the preliminary geometry and some peculiar details are sketched.

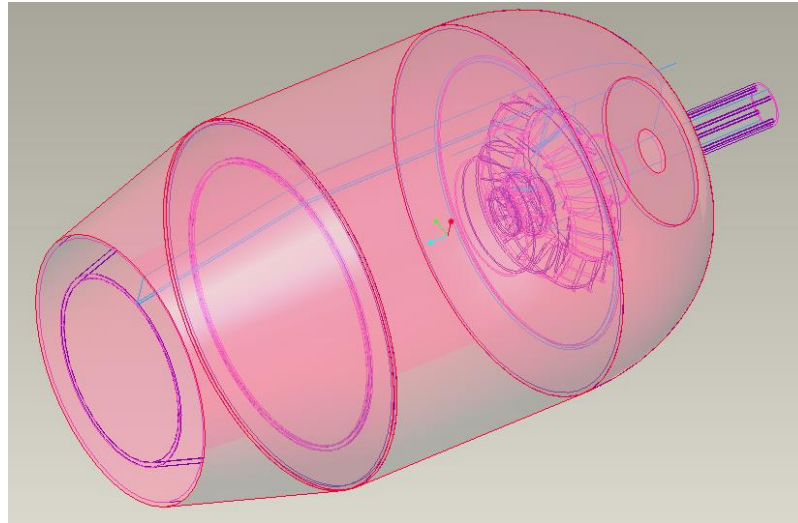


**Figure 7 - Combustion chamber preliminary design**

## 5 Recuperator

---

### 5.1 Recuperator configuration choice

The recuperator analyzed in this application is a primary surface type, due to its favorable properties of effectiveness, weight and reliability [5].

The exchange surfaces are modeled as Cross-Wavy surface (reported in Figure 8), since they are successfully employed in state of the art recuperated micro-gas turbines [6] (see Figure 9).

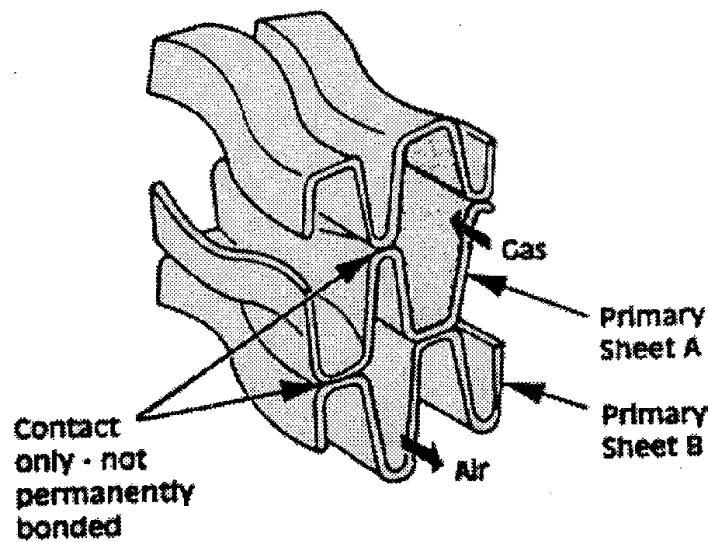


Figure 8: Cross Wavy surface scheme [7]

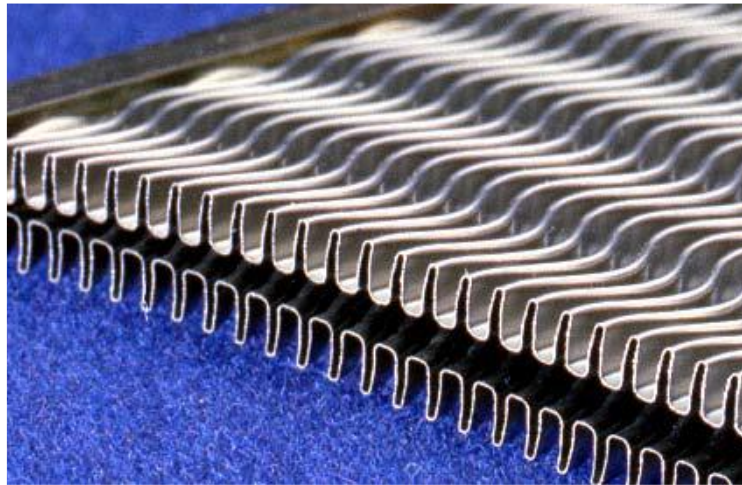
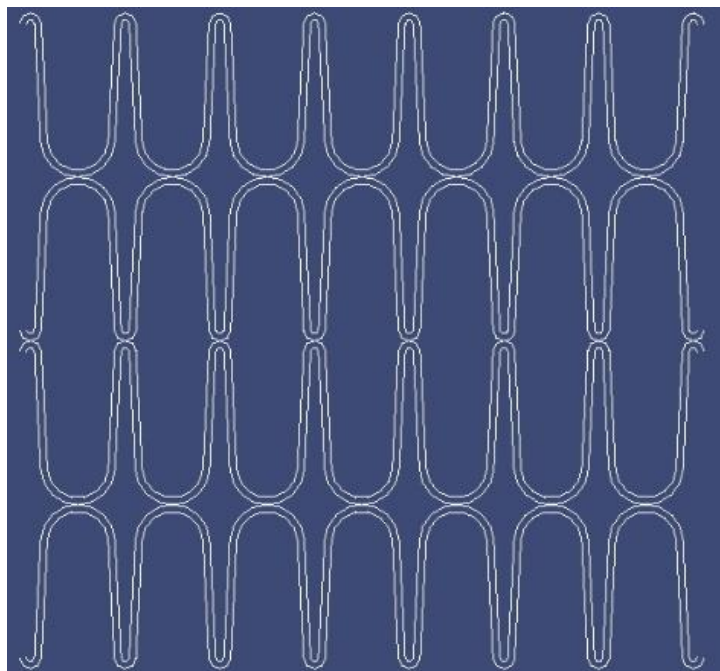


Figure 9: particular of the Cross Wavy recuperator mounted on the Capstone micro-gas turbines [8]

The Cross Wavy pattern presents two different cross sections, the larger ones allow the passage of the hot gas, while the compressed air passes through the smaller channels. Each duct is made of two corrugated metal sheets welded at the edge. The welded construction, compared to the brazed one (used in plate-fin recuperators), is cheaper and more reliable and it is one of the strength of the primary surface recuperators. The corrugated metal sheets are wavy (out of phase of  $180^\circ$  between them) in the main flow direction. This waviness create secondary flow structures: this structure disturbs the near wall boundary layer and so improves the heat transfer [7].

The specific surface geometry adopted in this work is sketched in Figure 10 and Figure 11. The ducts have trapezoidal cross section rounded at the top of the channel, while the waviness is made of straight lines connected to part of circles. This surfaces modelling follows that explained in [9] with the aim of create a geometry similar to that reported in Figure 8 and Figure 12.



**Figure 10: cross section of the exchange surfaces studied here**

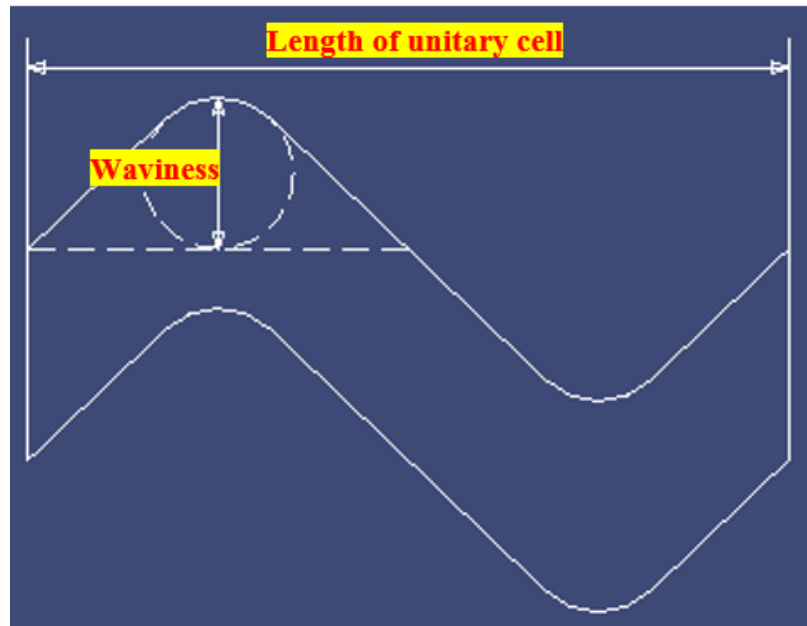


**Figure 11: waviness of the cross wavy ducts studied here**

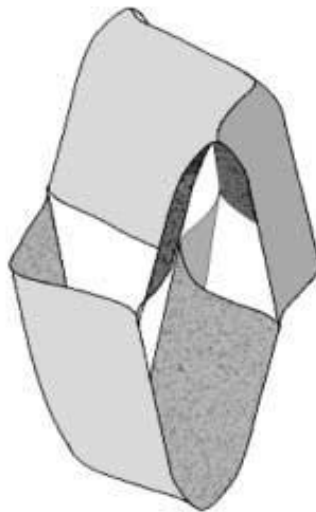


**Figure 12: model of a single Cross Wavy duct [9]**

In [5], the geometrical data of different Cross Wavy patterns are reported. Each pattern has the same cross section but different waviness and length of unitary cell (see Figure 11). The analyzed ducts are developed keeping the same proportion of the CW2-z5 pattern. The cited geometry is one of those studied in a CFD analysis conducted in [9]: the study provided data later arranged into simple correlations for the Nusselt number and the Fanning friction factor depending on the Reynolds number [7], [5]. The correlations give the results within the 10%

of the original data [7] (that of the numerical simulation) and are written in the following form:

$$\left(\frac{\text{Nu}}{f \cdot \text{Re}}\right) = C_1 + C_2 \cdot \text{Re} \quad (2)$$

where the constants are different for each pattern. For the selected geometry,  $C_1$  and  $C_2$  are reported in Table 5.

Constant	Nu	f·Re
$C_1$	1,0441	35,1707
$C_2$	0,01570	0,1168

**Table 5: coefficient of the correlations in eq. (2)**

The recuperator is made up of conventional 347 stainless steel, which is the material usually adopted when the maximum metal temperature does not exceed the value of 675°C.

Furthermore, the target pinch point temperature difference has been set equal to 30 °C, in order to improve the recuperator effectiveness.

## 5.2 Recuperator design calculations

Once the configuration, the geometry and the material are defined, it is necessary to evaluate the component dimensions. The procedure, described in [7], has been properly modified in order to calculate the channel characteristics by using a parametric model. The calculation scheme requires the knowledge of two kind of information: the properties of the flows entering the recuperator (and therefore the thermodynamic cycle of the micro-gas turbine) and the geometry of the air cell (in order to scale it, if necessary). The latter is already defined in the previous paragraph, while the former requires a specific code for the calculation of the regenerative cycle performance.

The cycle calculation is performed through GTcycle, coupled with the already cited dimensioning scheme used for the recuperator design. The code requires the knowledge of pressure losses for both the recuperator sides and, for this reason, a first guess pressure

losses value is assumed and then iteratively updated until convergence. A series of MATLAB functions enables to launch and manage the design tool.

The resulting dimensions of the ducts are different from those studied in [9], in order to match the value of the imposed Reynolds number. However, the proportions are kept, so it is possible to use the same correlations. The thickness of the metallic wall is the same for each calculation and is equal to 0,1 mm [5]. Different hydraulic diameters of the channel imply different compactness of the recuperator. The compactness is the ratio between exchange surface and volume of the heat exchanger and it is inversely proportional to the diameter of the ducts. Therefore, the compactness of the component is varied depending on the hydraulic diameter resulting from the chosen value of Reynolds number.

### 5.3 Results and discussion

The iterative and parametric calculations led to a large number of different recuperator configurations. However, a lot of them present unsuitable characteristics and are discarded. The “filter” applied on the results is on the recuperator mass, volume, length, inlet gas temperature and channel dimension values.

The inlet gas temperature is limited to 675 °C, in order to avoid the employment of a more resistant and expensive material than SS347.

Regarding the channel dimensions, they have a lower limit because of limitations on strength of materials. In fact, thin metallic foils may crack when folded with a very short length of unitary cell [7]. For this reason, all the solutions with single duct smaller than that studied in [9] have been discarded.

The limitations on the overall dimensions of the recuperator were set due to compactness reasons. Therefore the maximum recuperator mass, the matrix volume and the matrix length have been set to 250 kg, 1 m<sup>3</sup> and 1 m respectively.

By considering all the listed assumptions and constraints, the best design solution presents a Reynolds number of 500 and a gas side velocity of 19 m/s. The other parameters and the geometrical details are reported in Table 4.

The resulting heat exchanger has a very compact design, near to the value reported in [7]. This means that the channels are very small, so the pressure losses are higher than in the first- guess solution. The overall weight takes into account additional auxiliary components (e.g. manifold, casing etc.) allowing an increase in weight of about 10%. Volume and length are referred to the recuperator matrix only, so they do not include other elements.

**Table 6: Recuperator main characteristics**

<i>Recuperator mass</i>	<i>117 kg</i>
<i>Recuperator front section</i>	<i>0.136 m<sup>2</sup></i>
<i>Recuperator matrix length</i>	<i>0.31 m</i>
<i>Recuperator matrix volume</i>	<i>0.042 m<sup>3</sup></i>
<i>Exchange surface</i>	<i>50.7 m<sup>2</sup></i>
<i>Compactness</i>	<i>1214 m<sup>2</sup>/m<sup>3</sup></i>
<i>Pressure loss (air side)</i>	<i>260 mbar</i>
<i>Pressure loss (gas side)</i>	<i>121 mbar</i>
<i>Hydraulic diameter (air side)</i>	<i>0.83 mm</i>
<i>Hydraulic diameter (gas side)</i>	<i>1.77 mm</i>
<i>Length of unitary cell</i>	<i>5.81</i>
<i>Waviness</i>	<i>1.16</i>
<i>Total cross section area (air side)</i>	<i>0.036 m<sup>2</sup></i>
<i>Total cross section area (gas side)</i>	<i>0.076 m<sup>2</sup></i>
<i>Metal volume</i>	<i>0.013 m<sup>3</sup></i>

By employing the recuperator above described and keeping the pinch point temperature difference, compressor and turbine efficiency of 30 °C (which is equivalent to an effectiveness equal to 94%), 0.80 and 0.86 respectively, the resulting overall cycle efficiency raises from 30% to 32%.

## 6 Bearings

---

The rotor speed of the turbine is defined by choosing the specific speed that optimizes the plant efficiency. After the selection of the rotational speed and the evaluation of the minimum shaft diameter, the bearing speed is assessed by means of DN parameter (where D is the diameter of the shaft housing expressed in mm and N is the rotation speed expressed in rpm), as the limit comes from peripheral velocity. Since commercial micro-gas turbines work in the high speed range, the minimum DN is the most pressing constraint in bearing choice.

The other driving factors characterizing the micro gas turbines bearings are the following:

- bearing load capacity: in micro gas turbines the radial load is almost constant, even in transient operations, while the axial load due to the thrust of compressor and turbine is directed towards the compressor in base load operation whilst, during the start up phase, is directed towards the turbine;
- the dynamic behavior: the shaft layout strongly affects the eigenfrequencies of the system, which can occur at a speed lower than the operating one, therefore in the start up phase the bearings should be able to damp the vibration amplitudes of the shaft;
- dynamic behavior: in turbomachines shaft layout and compliance of the bearings, i.e. their stiffness and damping, influence critical speeds and out-of-balance response of the rotor. Bearings must provide sufficient damping to operate with vibrations of acceptable amplitude in nominal conditions and, for supercritical rotors, to overcome the critical speed without damage. In addition, for fluid film bearings, instabilities generated due to the fluid and its interaction with other parts (whirl, whip, hammering) must be avoided;
- power losses: typically, since micro-gas turbines efficiency is in the range 25-35%, bearing friction losses may influence the global energetic balance and friction factor becomes an important parameter in bearing choice. Moreover, all other losses (e. g. power required to the lubricant pump, power input for magnetic bearings...) have to be considered.

### 6.1 Bearing choice considering operating conditions

Due to the high speeds of rotation and temperatures, one of the most stressed mechanical component in micro gas turbine systems are the bearings and, therefore, lubrication system plays a key role in the operation of the machine. Therefore the most advanced tribological solutions must be considered in micro turbines systems and compared with conventional ones.

Active magnetic bearings (AMBs) and passive magnetic bearings (PMBs) use electromagnets and permanent magnets, respectively. Electrodynamic bearings (EDBs) are novel, promising supports which exploit the eddy current effects that take place in a conductor rotating in a constant magnetic field to achieve levitation. Airfoil bearings support the shaft by means of a compliant, spring-loaded foil journal lining. Ceramic hybrid bearings use ceramic balls in place of steel ones, while all ceramic bearings include also ceramic rings.

In this work only the airfoil bearings have been considered, since they represent the most promising solution and the current state of the art in the market.

## 6.2 Bearing external loads

Table 7 gathers the bearing loads computed for the reference unit. The total radial load is due to the shaft weight and it is directed downward. The positive direction of the axial forces listed in Table 7 is from compressor to turbine, as also shown by the direction of z-axis in Figure 1.

The total thrust load is computed as the algebraic sum of compressor and turbine axial forces. Both such forces are the resultant of the axial thrusts exerted on the blades and on the backside of the impellers by the working fluid.

Design variable [unit]		Value
Radial load (rotor weight) $W$ [N]		40
Total thrust load (absolute value) $T_{ref}$ [N]		500
Axial thrust on compressor blades [N]		2100
Axial thrust on turbine blades [N]		-3010
Case A	Pressure on the back side of the impellers (gauge) [Pa]	250 000
	Compressor thrust $T_c$ [N]	-600
	Turbine thrust $T_t$ [N]	1100
Case B	Pressure on the back side of the impellers (gauge) [Pa]	80 000
	Compressor thrust $T_c$ [N]	1200
	Turbine thrust $T_t$ [N]	-1700

Table 7: Loads acting on the bearings of the reference micro-GT unit

Consequently, together with the area of the impeller backside, the pressure on the clearances between casing cover and impeller back shroud (backside pressure) plays an important role in determining the nominal axial thrusts, which are plotted in Figure 13 as a

function of the backside pressure. By means of CFD simulations a backside pressure equal to 0.25 MPa (case A) has been calculated, so that both the impeller thrusts are directed toward the external side of the unit. Nevertheless, for different impeller geometries, which may yield different pressure drops between compressor delivery and clearances, compressor, turbine as well as total thrust directions can reverse, as shown by Figure 13 for backside pressures lower than 0.15 MPa. As a consequence, such case (both thrusts directed toward the inner side of the machine) must be taken into account. To this purpose, for the same reference value of the total axial load (500 N) case B is identified in Figure 13. The axial loads in both case A and B are summarized in Table 7. An axial force reversal can also occur during transient operation, e.g. the start/stop phase of the unit.

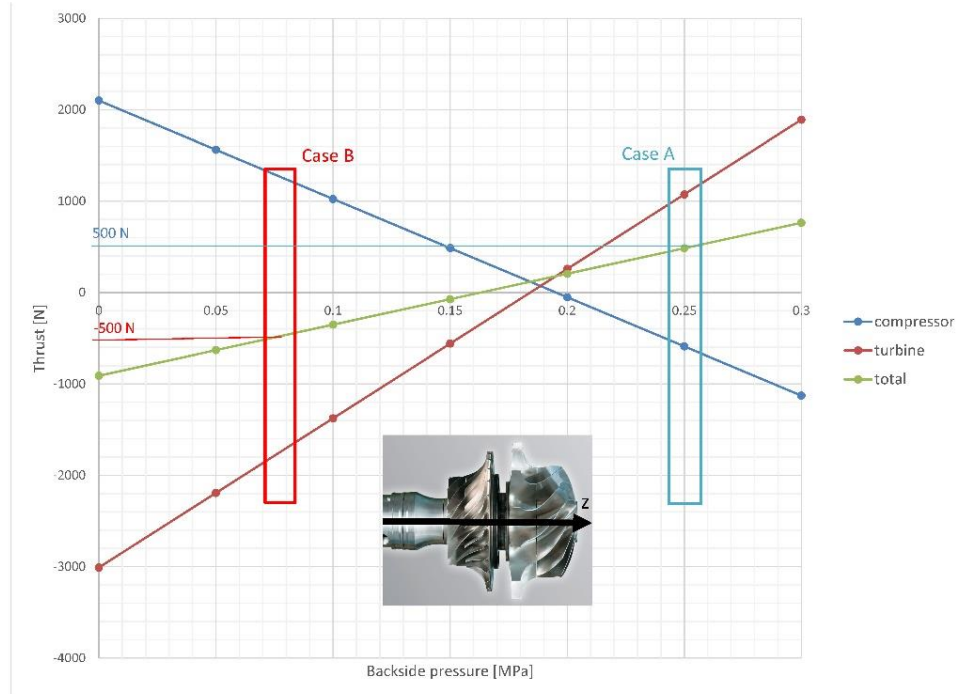


**Figure 13: Compressor, turbine and total thrust acting on the shaft in nominal conditions for the reference micro-GT as a function of the backside pressure**

### 6.3 Bearing requirements

Requirements are related to the operating conditions of the units (operative speeds and temperatures) and bearing performance (duration, load carrying capacity, power loss).

The high rotation speeds of micro-GT shafts yield different problems (e.g. ball spinning, centrifugal loading, skidding), which have greater effect on larger bearings. Therefore, an important requirement is that bearings have a high peripheral speed limit.

In the following, the effect of peripheral velocity is quantified in terms of the DN speed factor (where D is the diameter of the shaft housing expressed in mm and N is the rotation speed expressed in rpm).

Micro-GT units must usually operate in high-speed conditions, which for rotors are usually characterized by speed factors ranging between  $1 \cdot 10^6$  and  $2 \cdot 10^6$  mm rpm. In ultra-high-speed rotor applications DN overcomes  $2 \cdot 10^6$  mm rpm, as in the case of mobile power systems [10], which are beyond the scope of the present work.

Indeed, in the case of the reference micro-gas turbine the operative speed factor is roughly  $1 \cdot 10^6$  mm rpm (see Table 7), so that bearings with DN limit lower than such operative value must be discarded.

In addition, the bearings must operate throughout the domain of possible temperature conditions of the micro-gas turbine. Such temperatures range between  $100^\circ\text{C}$  and  $1000^\circ\text{C}$  in nominal operation, while during start-up they extend down to room temperature. Expected working temperature of the bearings depends on their location and relevant thermal management, e.g. type of cooling or vent.

Bearing duration should preferably overcome 70.000 hours (the average duration of the units) and should not be limited by the number of start/stop cycles, so that maintenance and bearing replacements could be minimized.

Reasonably predicted axial load is a magnitude order higher than radial load (Table 7). The former load is significant as far as metal fatigue and wear are concerned, while the latter is so light that it may cause stability problem at high speed in self-acting radial bearings.

Since the state of the art efficiency of micro-gas turbines is quite low, bearings must not reduce further this value. To this goal, they should be designed for the minimum power loss (e.g. friction) and their possible power input should not be significant.

Finally, depending on the shaft layout, resonance eigenfrequencies usually occur at a speed lower than the operating one, therefore the vibration amplitude should be limited by the bearing damping.

## 6.4 Bearing comparison

The adequacy of the most reliable types of bearings is studied. To this purpose, the behaviour of the following types of bearings is analysed:

- steel rolling element bearings, lubricated by grease or oil;
- sliding bearings, lubricated by oil;
- air (film) bearings;
- magnetic bearings;
- ceramic bearings.

The first two categories include conventional bearings, taken as a reference for performance comparison. The last item include rolling element bearings entirely manufactured in ceramic material and hybrid bearings, made up of steel rings and ceramic balls, with or without film coatings on the races.

Only supports based on well-established technology are analysed, while research solutions (still in development), like squeeze film bearings, hydroinertia gas bearings, ferrofluid bearings and metal mesh foil bearings, are not considered.

The assessment of compliance of the different bearing types with micro-GT operating conditions, including speed (DN factor), temperature and loads, requires a proper comparison of literature and technical data.

#### 6.4.1 Operating speed

Operative and absolute speed limits of the different bearing solutions are compared in Figure 14.

The speed limit of rolling element bearings is mainly due to the skidding of the elements on the rings [10]. Among such bearings, high precision angular contact ball bearings by means of suitable tolerances, osculation, rolling element size and number can reach the high speed required by micro-GT ( $DN > 1 \cdot 10^6$  mm rpm). The maximum DN reached by high precision ball bearings is about 3 million mm rpm [11][12]. Higher DN values can be reached by angular contact bearings by means of specific lubrication systems [13].

Manufacturer's catalogues (SKF, Schaeffler) show that the use of ceramic balls in place of steel ones can yield an operating speed increase of roughly 20-30%. Such result is confirmed by the data reported in [14], i.e. speed of hybrid bearings can be increased by 20-30% compared with conventional ones. Accordingly, in comparison with steel bearings, a 60% decrease of centrifugal load matched with the 30% load capacity reduction predicted by Hertz theory finally provides a maximum allowable increase in rotation speed of just 32%. It decreases to 10% for all ceramic bearings.

The DN operative limit reported for oil-lubricated slide bearings regards bearings of turbines for power generation plants [15] and for induction motors [16]. In such cases, operative speed is only restricted by strength limits and by the allowable temperature. In micro-gas

turbine applications, the operative speed of slide bearings is also limited by their stability and suitable bearing geometries are required, e.g. elliptical and pocket bearings, multi-lobe bearings, tilting pad bearings (listed from least to most stable).

Waumans et al. [17][18] report the highest achieved DN-number for a self-acting bearing operated in air is  $7.2 \cdot 10^6$  mm rpm. It is reached by an aerodynamic journal bearing stabilized by means of a grooved bush with a wave-shaped geometry as well as a flexible and damped support structure.

As far as foil bearings are concerned, maximum speed is relevant to a  $\varnothing 8$  mm bearing for micro-gas turbines operating up to 642 000 rpm (DN=5 136 000 mm rpm) from results in [19].

Among grooved bearings, the maximum operative DN of a Herringbone grooved journal bearing (HGJB) with enhanced grooved geometry [20] is  $2.7 \cdot 10^6$  mm rpm and it is lower than foil bearing one. In addition, experimental results confirm that grooved hybrid bearings (GHBs) can run satisfactory at speeds in excess of  $3.0 \cdot 10^6$  rpm mm. Nevertheless, such DN is assumed as upper speed limit for grooved bearings, as they are prone to destructive whirl instability at ultra-high speed [21].

Hybrid aerostatic bearings are suitable due to the low air consumption, such that the impact on the global efficiency is extremely small, and the aerostatic stabilizing effect at high speed [22]. For proper operation, they require air supply at high speed, when it is actually available in micro-GT systems. Data relevant to the maximum speed reached by aerostatic bearings refer to [23]. The relevant maximum operative speed is also documented in [24].

In today's industrial applications active magnetic bearing (AMB) rotational speeds are in the range of about 180.000 rpm for a grinding spindle, or about 300.000 rpm for small turbo-machinery [25]. The latter value, by assuming  $D=15$  mm as suggested by Table 7, corresponds to  $DN=4.5 \cdot 10^6$  mm rpm, which is confirmed by the data suggested by SKF. Anyway, by means of carbon fiber bandages in the rotor  $6.8 \cdot 10^6$  mm rpm can be reached [24]. Such value is a documented maximum speed for actual applications rather than a maximum theoretical limit, which is unknown as in the case of airfoil bearings [26].

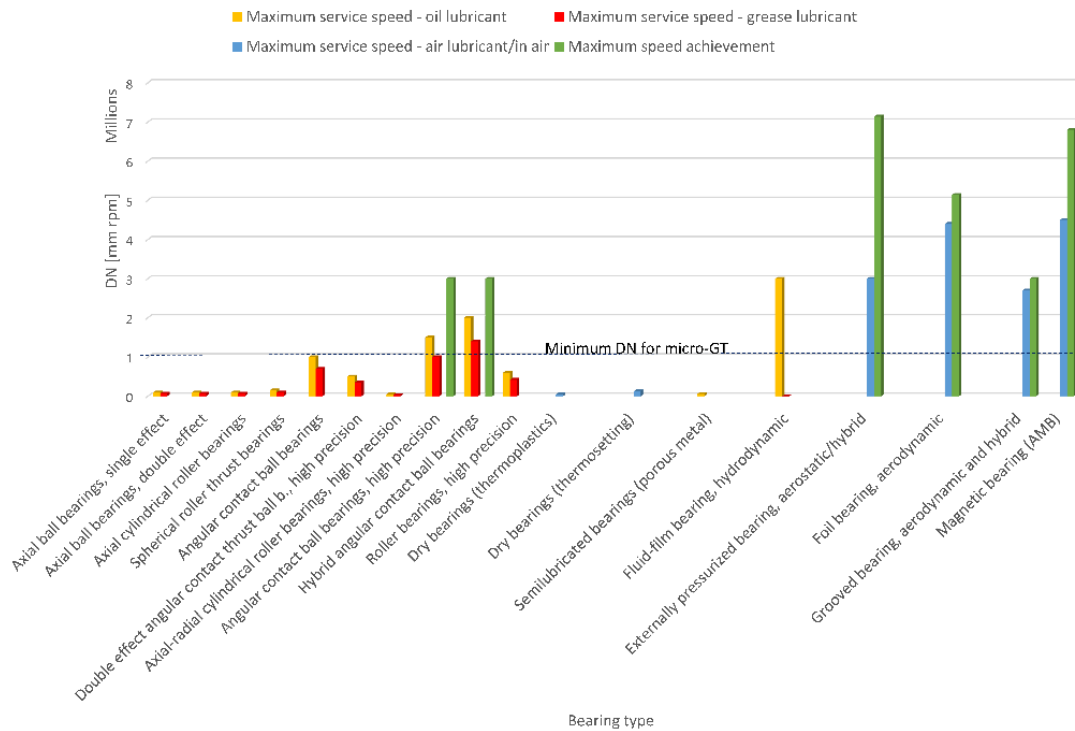


**Figure 14: Maximum speed factors for different bearings**

## 6.4.2 Operating temperature

Table 8 lists the maximum operational temperatures of the bearings.

As far as steel rolling bearings are concerned, in addition to lubrication system as well as lubricant characteristic, steel reaction to heat and dimensional stability influence their endurance at high temperature. Generally, hardness of steel starts to decrease as temperature rises over 200°C. In addition, as steel heats up, phase transformation occurs and the bearing parts expand. The maximum dimensionally stable temperature ranges between 120°C and 250°C depending on steel type (source: NSK). Accordingly, a limit temperature of 180-260°C for rolling element bearings is indicated in [26]. Similarly, a 125-150°C operative limit for AISI 52100 bearings which can be specially stabilized up to 200 °C and up to 315°C by using tool steel bearing materials is reported in [15]. The Authors of [16] confirm that operative temperature is usually kept below 150°C except for heat stabilized bearings.

Ceramic bearings behave better than steel rolling bearings at high temperature. Indeed, hardness and strength of silicon nitride do not deteriorate at high temperatures when compared to those of bearing steel. Particularly, the advantage of all ceramic bearings over hybrid bearings consists especially on the major capability of working in dry or underlubricated conditions, at high temperature (<800°C) and corrosive environment [14]. Such suitability to high temperatures is confirmed in [15], which indicates a limit of 650°C for ceramic bearings with vapour phase lubrication or solid lubricants.

Hydrodynamic bearings are the most limited in operating temperature. Indeed, such limit comes from bearing surface and oil endurance. Soft metal and Babbitt limit upper temperatures are usually in the 125-150°C range [15]. Limit operating temperature of hydrocarbon oils is 93°C [27], while high temperature oils can also reach 150-200°C, e.g. silicon oils. Therefore, oil lubricated slide bearings are ultimately limited in temperature by bearing surface resistance.

Gases can be employed as lubricants over an extremely wide range of temperatures. For gas bearings operating temperature limits comes from shortcomings of solid components (journal and bearing material), not of the lubricant. Electric motors with ceramic windings supported by gas bearings can work for long periods at temperature up to 500°C [28], which is assumed as limit temperature for aerodynamic bearings.

Foil bearings require the use of a solid lubrication to prevent wear and reduce friction during instances of contact, i.e. at low speed conditions at start-up and shutdown. Since common lubricants, e.g. graphite and moly-disulfide ( $\text{MoS}_2$ ), are limited to 150°C, solid lubrication is often obtained on the shaft and top foil layer by means of thin, soft polymeric film and sacrificial coatings. Innovative coatings, e.g. nanocomposite for journals and CuAl alloy for top foils, can reach temperatures as high as 650°C, which not by chance is also the limit operating temperature indicated for foil bearings in [26]. By using well-established tribo-solutions like polymer coatings, air bearing operation is roughly limited below 300 °C [29].

Ceramic aerostatic bearings can reach a temperature as high as 800°C [28] and, in general, temperatures up to 900°C and speeds up to 65 000 rpm are feasible for externally pressurized gas bearings [30]. Indeed, aerostatic bearings have the highest temperature limit among the bearing analysed. It is higher than temperature limit of aerodynamic bearings due to the external air supply, since air cools as it expands. In addition, the very low friction losses avoid thermal expansion due to viscous heating.

Among magnetic bearings, a great drawback of PMBs comes from high temperature operation requirements of micro-GT systems, as permanent magnet stability is affected by temperature. Maximum practical operating and Curie (demagnetization) temperatures for the major classes of permanent magnet materials are in the ranges 150-540 °C and 310-860

°C, respectively. On the contrary, AMBs can work in extreme temperature environments (500-600°C) [26].

<b>Bearing type</b>	<b>Max operating temperature [°C]</b>
Rolling element	125-315
Ceramic hybrid	350
Ceramic integral	800
Oil sleeve (journal)	125-150
Oil tilting pad	125-150
Hydrostatic	125-150
Magnetic (AMB)	500-600
Magnetic (PMB)	150-300
Aerodynamic, air foil	650
Aerodynamic, rigid/grooved	500
Aerostatic	900

**Table 8: Maximum operating temperatures for different bearing types**

## 6.5 Load carrying capacity and life

The maximum specific loads for the bearing types in analysis are summarized in Table 9.

<b>Bearing type</b>	<b>Max service specific load [MPa]</b>
Rolling element	2
Ceramic hybrid	2
Ceramic integral	2
Oil sleeve	2.1
Oil tilting pad	4.4
Hydrostatic	6
Magnetic (AMB)	0.8
Magnetic (PMB)	0.4
Aerodynamic, air foil	0.7
Aerodynamic, rigid/grooved	0.1-0.2
Aerostatic	0.2

**Table 9: Maximum service specific loads for different bearing types**

For rolling element bearings the "carrying capacity" is the ability of the bearing to carry a given load for a predetermined number of cycles or revolutions [31].

The maximum documented specific load for rolling element bearings operating in gas turbines is reported in [26]. Table 5 reports the durations of bearings in a shaft support system designed by means of catalogue high precision rolling bearings solely. They are computed according to the adjusted basic rating life [32] by using data in Table 7. It is assumed that radial load is equally distributed between two sets of high precision angular contact bearings and only one (locating) set carries the axial load in order to allow the thermal dilatation of the shaft. The solutions with both 2 and 5 matched bearings in the sets (in tandem arrangement) that carry the axial load are not satisfactory compared to the machine life (about 70.000 hours).

Set	L <sub>1</sub> [h]	L <sub>10</sub> [h]	L <sub>50</sub> [h]
1 bearing, radial load W	267960	1276000	6380200
2 bearings, radial load W and axial load T <sub>ref</sub>	65	310	1549
5 bearings, radial load W and axial load T <sub>ref</sub>	451	2150	10747

**Table 10: Expected life for sets of angular contact high precision bearings, carrying half of the rotor weight and, if specified, the axial load**

Dynamic load ratings of steel bearings can also be used for ceramic bearings of the same dimensions [33], since from test results and predicted values service life of ceramic bearings is longer than that of steel bearings, except for heavy loads.

For the remaining bearings, fatigue is not the main concern, and the external load can be treated as static.

Sleeve bearings life is theoretically infinite and extremely long when they are properly maintained. Significant wear may occur only during extended start-up or coast-down periods, as mixed lubrication occurs at low speed. If the frequency of such events is high, hydrostatic jacking is recommended to minimize bearing wear [16].

Load capacity of oil-film bearings is basically function of speed and oil viscosity, so that high temperature plays a role by reducing viscosity. Many specifications limit motor bearing specific pressures to 1.4 MPa, which is often compliant with structural strength. Nevertheless, most journal bearings safely tolerates pressures beyond 2 MPa, as reported in [15]. Tilting pad thrust bearings for turbines carry further increase of specific load and pads are subject to elastic deformation.

Generally, as hydrodynamic and hydrostatic bearings distribute the load over a larger area than rolling element bearings, their load capacity can be higher. Particularly, hydrostatic bearings can support huge loads, higher than hydrodynamic supports, as their pressure distribution is more uniform.

Air (aerostatic and foil) bearings, because of the different film layer, approximately support only a fraction of the load carried by hydraulic bearings with the same dimension. Indeed, specific load capacity of air foil bearings is 0.7 MPa [26], which is roughly one-fifth of the specific load for hydrodynamic bearings (3.5 MPa, on average). Differently, specific load for aerostatic bearings is lower due to a further constraint. Indeed, aerostatic bearings are typically limited to operate at less than 10 atm of pressure (usually 0.69 MPa) for safety reasons and due to the lubricant compressibility, which yields much higher flow rates and pumping power demand for the same pressure in comparison with liquid lubricants [34]. Such value is much lower than supply pressure of hydrostatic bearings, which typically operate at 20-40 atm but can reach 200 atm, when space is not limited and large loads must be supported. Specific load capacity (load per pad area) for aerostatic and hydrostatic bearings is the efficiency multiplied by supply pressure, where the efficiency is typically 25%-40%.

According to the basic rating life formula [32], for constant duration load-carrying capacity of rolling element bearings drops as speed rises. On the contrary, load capacity of foil bearings is proportional to rotational speed. Hence, foil bearings outperform rolling element bearings at high speeds [35] but require solid lubrication at low speed in order to reduce friction and wear. Particularly, conventional solid lubrication systems, i.e thin polymer films, enable over 100 000 h of operation before requiring a major overhaul. Beyond the temperature limits of polymer coatings (300°C), innovative coatings (PS304, Korolon) have demonstrated lives in excess of 100 000 start-stop cycles under moderate loads (0.34 MPa) and high temperatures (ranging between 178°C and 650 °C) where such solid lubricants become active. However, bearing operating life is cut by over half (roughly 33.000 cycles) at room temperature (25°C), where the coating does not perform as well [29]. For low temperature start-ups, usually under higher loads, life may further decrease [36].

In order to characterize the behaviour of foil bearings by means of a suitable map, in [37] a modified Sommerfeld number  $S'$  is correlated with the specific power loss. Foil journal bearings must be designed so that they operate in the high speed (or lightly loaded) regime ( $S' > 6$ ) of the operating map plotted in Figure 15 in agreement with the suitable regression proposed by the reference authors. Particularly, the nominal working point should be located in the high-speed (lightly loaded) regime, but significantly far from the shaft strength and thermal limit (specific power loss lower than 155.000 W/m<sup>2</sup>).

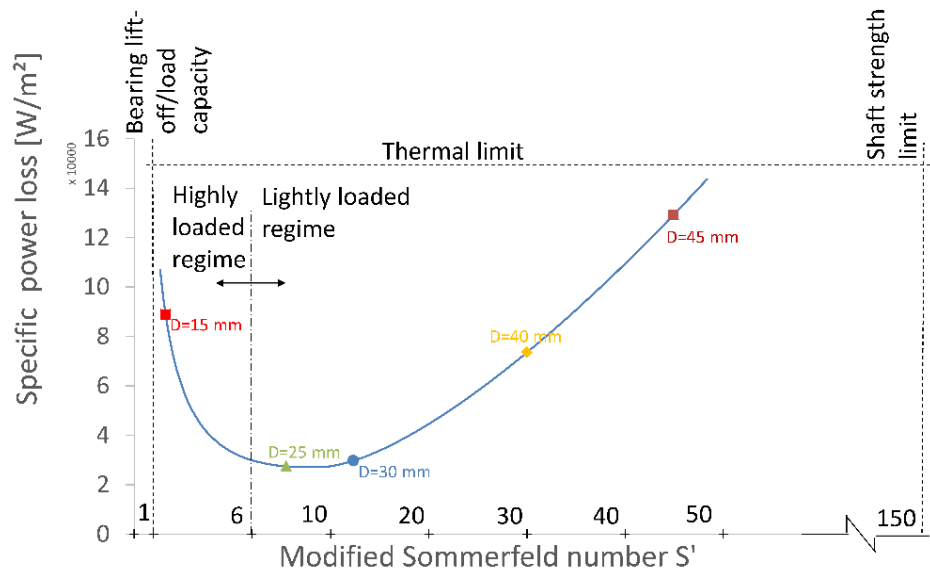


**Figure 15: Performance map of foil bearings and operating points of the reference micro-GT for different journal diameters**

In order to locate in the operating map the nominal working point of a single radial foil bearing supporting the reference micro-gas turbine shaft, the data reported in Table 7 are used together with unit (axial) length to diameter ratio ( $L/D=1$ ), load coefficient equal to  $2.7 \cdot 10^{-4} \text{ N}/(\text{mm}^3 \text{ krpm})$  (third generation bearings) and isoviscous behaviour assumption. In addition, the total load is approximated by the external one (40 N) as first estimate. By means of such assumptions, the assessment of  $S'$  according to [37] suggests that the working conditions are not suitable ( $S'=1.6 < 6$ ). Therefore, the journal diameter must be increased (optimal values range between 25 and 40 mm, as suggested by Figure 15). Indeed, transitioning over to oil-free lubrication requires suitable design solutions in that thin shafts are not required anymore to avoid rolling element bearings from operating above their DN threshold. On the contrary, large diameter hollow shafts must be used in order to increase the peripheral speed and, as a consequence, the load capacity of air bearings [36].

As far as the remaining air film bearings are concerned, the different fluid film bearing designs (multi-lobe and tilting-pad geometries) achieve better stability than plain bearings at the expense of load carrying capacity. On the contrary, gas-lubricated grooved bearings promise stability with minor reduction of lift [38].

Magnetic bearings have advantageous load carrying characteristics, whereas load does not drop as speed decreases. Nevertheless, if the electromagnets are unable to support the applied load because they are undersized or malfunctioning, the shaft cannot be levitated

and the machine shuts down [39]. Therefore, backup bearings are required to protect the rotor against overloads and power loss.

Reasonable specific loads for AMBs range between 0.3 and 1 MPa. Particularly, the maximum specific load value reported in Table 9 is suggested for AMBs in [26] on the basis of the data published in [40][41].

For a stacked structure PMB fabricated using neodymium-iron-boron magnets with a remanence of 1.3 Tesla (42 MGOe magnetic field), the maximum specific load, referred to the axial cross section (LD), is roughly 0.4 MPa and the corresponding axial specific load is 0.6 MPa [42].

Life time expectancy of passive bearings is very high, i.e. in excess of 20 years. As AMBs include more components (controllers, coils, sensors) and a laminated rotor, their life is expected to be shorter but, anyway, AMBs can still last 20 to 30 years with proper substitutions of failed components.

## 6.6 Innovative support system

The conclusion of the review study is that each bearing type has different strengths and weaknesses. Therefore, by using different types of bearings in the same support system, a proper design of their arrangement should be capable of taking the maximum advantage of the peculiarity of each bearing.

To this purpose, the conceptual design of an innovative support system, which takes advantage of both foil and rolling element bearings, is presented. A detailed literature analysis has been carried out in order to find similar design solutions, but nothing has been found. Experimental tests should be carried out in order to understand the real behavior of the proposed bearing solution.

### 6.6.1 Layout and components

A simplified scheme of the assembly of the cutting-edge support system is depicted in Figure 16. In the simplified scheme of the invention used hereafter load direction is assumed as in case B of Table 7.

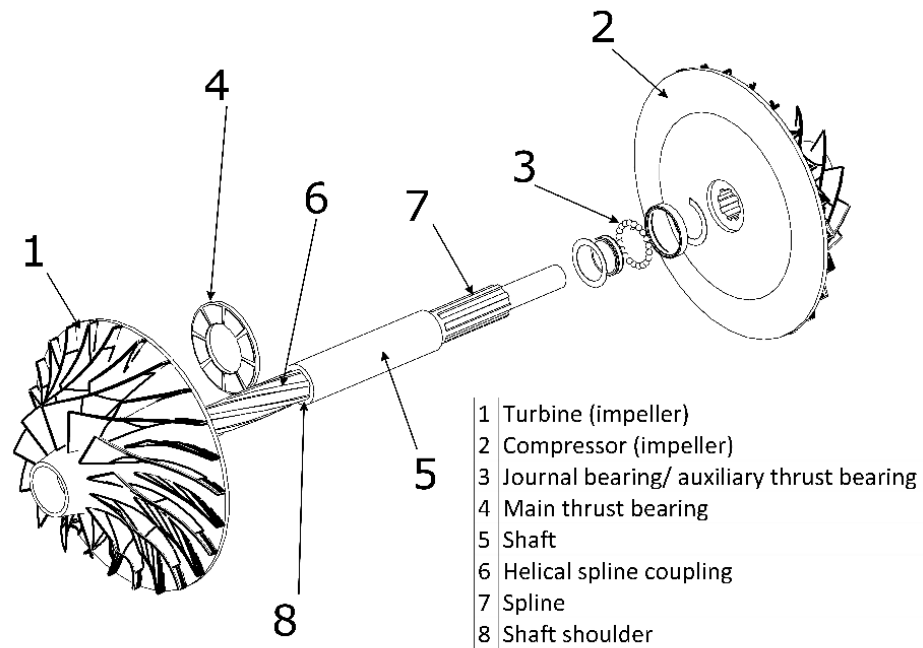


**Figure 16: Simplified assembly of the innovative support system**

The angular contact ball bearing (3), at the compressor side (Figure 16), is capable of carrying both radial and axial loads. As axial load may reverse during start-up of the unit (see [43]), the bearing must be double-effect, i.e. it is made up by two (or more) matched single row bearings in back-to-back arrangement. Although four-point contact ball bearings are normally not available for precision (high speed) applications, a single bearing is depicted in Figure 16 for the sake of conciseness of the scheme and clarity. As shown in Figure 17, such a bearing is mounted by inserting the external ring inside a suitable bore on the machine frame (9) and by placing the inner ring onto the relevant seat on the shaft with proper tolerances. Particularly, the outer ring must be axially constrained in order to carry thrust loads (locating bearing).

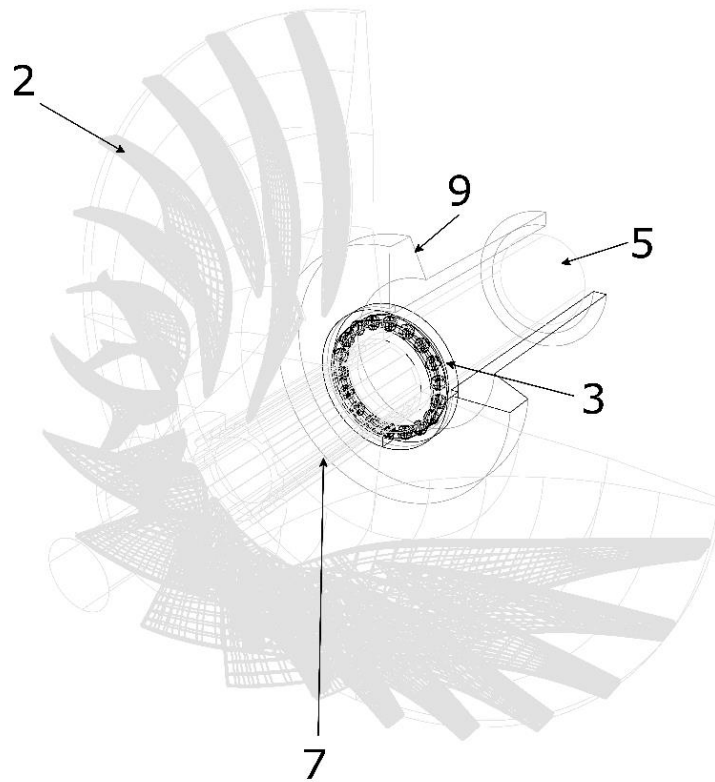


**Figure 17: Ball bearing seat and spline coupling at compressor side**

A possible second radial support (always of rolling element type, e.g. a set of angular contact ball bearings in back-to-back arrangement) is included in Figure 16 for simplicity. Nevertheless, it would be useful in order to avoid that the shaft is in a cantilever configuration and it should be able to carry radial load solely. Therefore, such additional radial bearing should not be constrained axially to the housing on the frame (non-locating bearing), so that axial the thermal dilatation of the shaft would be allowed.

The plate of the foil bearing, i.e. component (4) listed in Figure 16, is fixed to the frame as shown in Figure 6, where the runner surface is located on the back of the turbine rotor (1) and the opposite sliding pairs, runner (11) and pads (12), are separated by the clearance  $c_z$ . A suitable spacer (10) must allow a proper adjustment of the clearance (or preload in static conditions), in order to ensure optimal operation of the foil bearing.

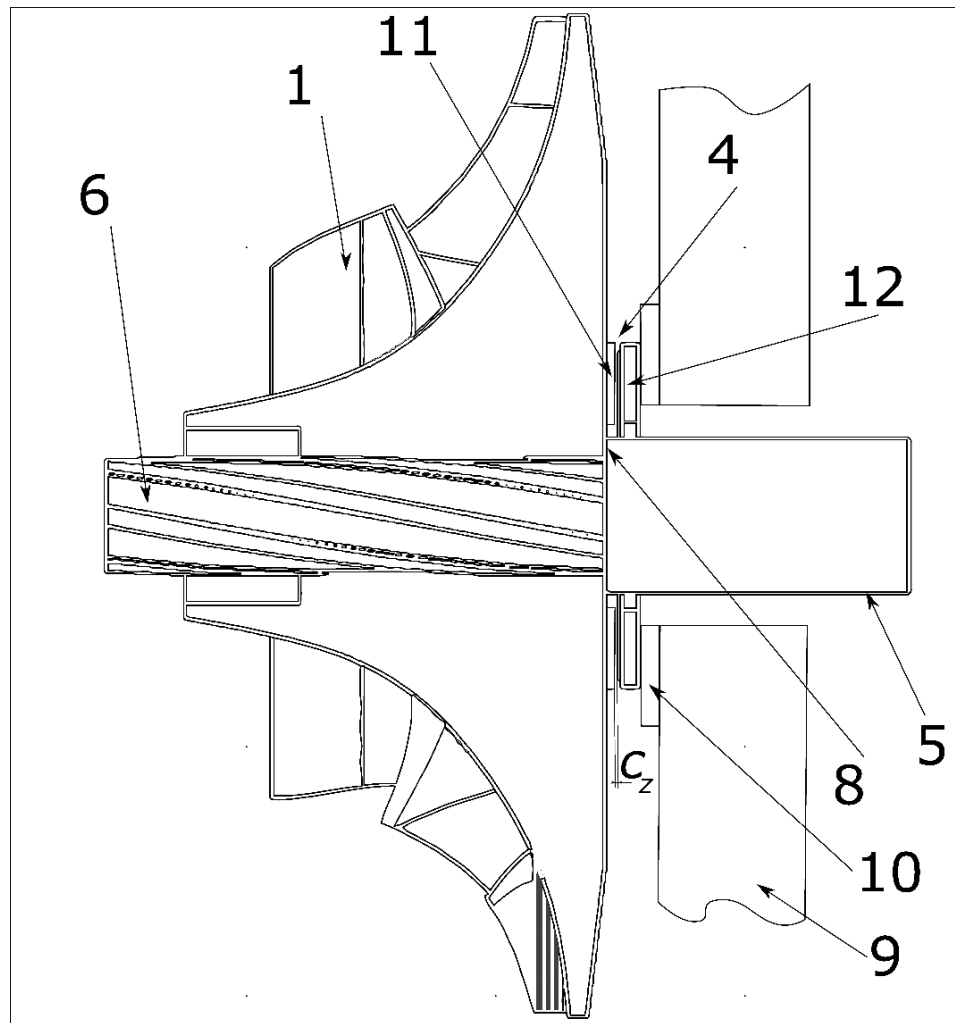


**Figure 18: Foil air bearing installation and adjustment**

When the foil bearing has no aerodynamic load-carrying capacity, the turbine thrust acts on the shaft shoulder (8). Differently, after an air film is formed and the relevant aerodynamic pressure is generated, its micrometric thickness causes the runner/impeller assembly (1) to move accordingly in the axial direction, so that the contact between the turbine impeller hub and the shaft shoulder does not occur anymore. Consequently, in nominal conditions and starting from the rotation speed at which the runner is airborne, the only axial load transfer from the turbine to the shaft may occur through the helical spline coupling, as a function of the design helical angle.

Figure 16 also illustrates the coupling between the impeller hubs and the shaft (5). The compressor impeller (2) is fixed by means of a conventional spline pair (7) (made up by equally spaced straight grooves), which profile is depicted with parallel side (or straight teeth). Differently, on the turbine side a helical spline pair (6) (in which each groove forms a

helix around the shaft) is machined. Such particular spline fit provides the additional function of axial load distributor. Of course, involute instead of parallel-side profiles may be chosen for both compressor and turbine wheel spline pairs. The purpose of the helical spline pair is to distribute the axial load between main (4) and auxiliary (3) thrust bearings, as explained in the following paragraphs.

### 6.6.2 Main thrust bearing relief

The innovative layout and, particularly, the direct matching of turbine impeller and main thrust bearing (4) allows for its relief during start/stop of the unit.

With reference to thrust loads and symbols given in Table 7 (case B), let  $F_t = -T_t$  and  $F_c = T_c$  be the turbine and compressor thrusts, respectively (Figure 19). They are caused by the pressure of the evolving fluid on the relevant impellers.

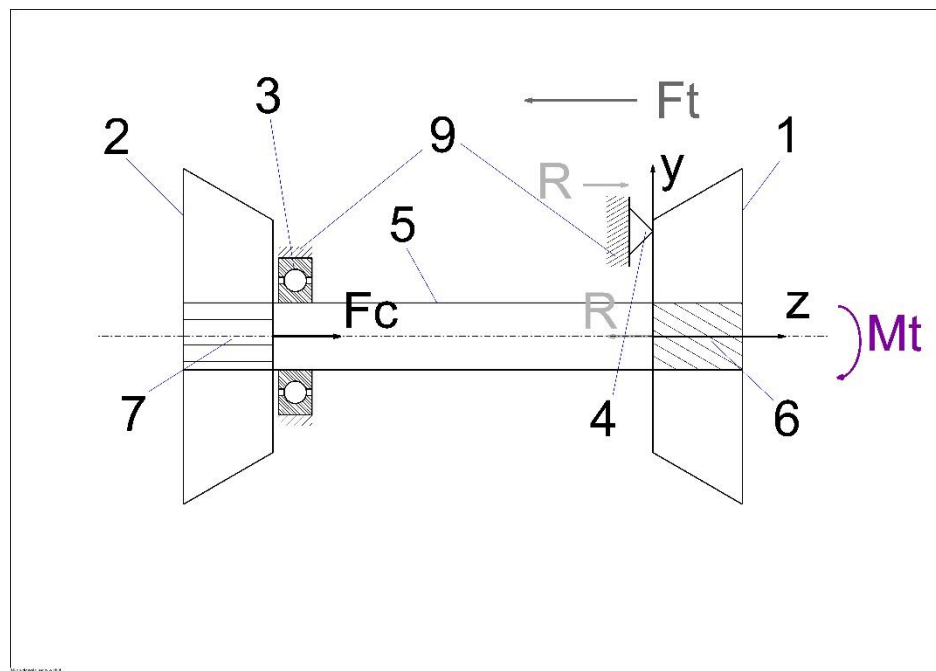


**Figure 19: Static scheme (axial forces) of the innovative rotor operating in nominal conditions**

At start-up and until the onset of the aerodynamic lift, the auxiliary bearing (3) carries the whole thrust so that the main thrust bearing (4) is unloaded and, therefore, it works with minimal or no wear (see [43]). Indeed, in such condition, the turbine impeller (1) exerts the thrust  $F_t$  on the shaft shoulder (8) (visible in Figure 16 and Figure 18) instead of on the foil bearing (4). Through the shoulder and the shaft the thrust  $F_t$  is then transferred to the shaft

support, i.e. the auxiliary bearing (3), like in a conventional bearing layout. Once the runner of the main bearing becomes airborne at sufficient speed and a consequent translation of the turbine impeller occurs, automatically it relieves the auxiliary one, as the shaft shoulder (8) does not receive thrust anymore.

### 6.6.3 Load partition

According to the explanation of the previous paragraph, in nominal working conditions with no helical spline fit (for example, by adopting a straight grooved spline on turbine-side too), the whole thrust of the turbine  $F_t$  would be carried by the main thrust bearing as well as the compressor thrust  $F_c$  would be supported by the auxiliary bearing. In a conventional shaft-bearing assembly, the reference thrust  $T_{ref}$  that loads the single axial bearing comes from the opposite thrusts exerted by turbine and compressor, i.e.  $T_{ref}=F_t-F_c$ . Therefore, during nominal operation in comparison with a conventional support system, the new assembly design would disadvantage the main thrust bearings, whereas  $F_t > T_{ref}$ . Differently, by taking advantage of the (turbine-side) helical spline pair as an actuator, a part of the turbine thrust can be transferred from the hub to the shaft. In such a way, any wanted division of the thrust load between the two (main (4) and auxiliary (3)) bearings can be obtained as a function of a single design parameter, i.e. the spline helix angle  $\beta$  shown in Figure 20.

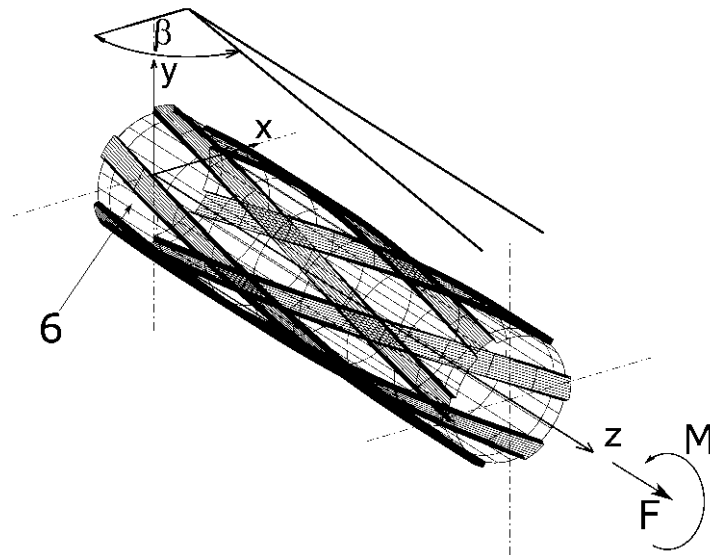


Figure 20: Helix angle and reference system of spline coupling

Particularly, by means of a suitable choice of the helix angle in the design phase, in nominal conditions it is also possible to subject the main axial bearing to a thrust  $T_{ref}$  as in a conventional support system, while the auxiliary bearing remains axially unloaded. In such a case, as this support is an angular contact ball bearing, it carries solely the radial load, which intensity is much lower than axial loads. Obviously, this is only an example of load division. The new layout allows us setting the optimal load division in the design phase as a function of the load-carrying characteristics of the bearings, as well as expected duration and reliability of rolling element supports.

#### 6.6.4 Law of load distribution

Firstly, the law of load distribution followed during nominal operation by the helical spline pair, employed as a mechanical actuator besides a simple coupling system, is determined.

Figure 19 depicts the forces acting in nominal conditions on the rotor components according to the modifications resulting from the innovation. The constraint simulates the main axial bearing (4), which carries the load  $F_t-R$ . The axial forces  $R$  are the (equal) action and reaction that the turbine impeller exerts on the shaft through the helical spline. The total thrust that acts on the shaft is  $F_t-R$  and is carried by the auxiliary axial bearing (3). The torque  $M_t$  is the resisting torque of the turbine due to the pressure exerted on the relevant blades.

A campaign of FEM structural analyses has been carried out on a model of helical spline coupling (Figure 21) with parallel-side profiles by varying the design helix angle  $\beta$  from 45 to 135 deg. Reference system and helix angle  $\beta$  of the spline coupling model are shown in Figure 20. In agreement with the helix angle definition, the middle of the range ( $\beta=90$  deg) corresponds to a spline with rectilinear generatrices (straight teeth).

As shown in Figure 21, the spline and hub submodels are merged into the coupling model by means of contact elements. Two load cases are analysed, where the hub section of one model end is submitted to either the axial load  $F_t$  or the torque  $M_t$  according to the values in Table 7. Suitable constraints are added to the other end of the model, i.e zero displacement components  $d_r, d_\theta, d_z$  in cylindrical coordinates.

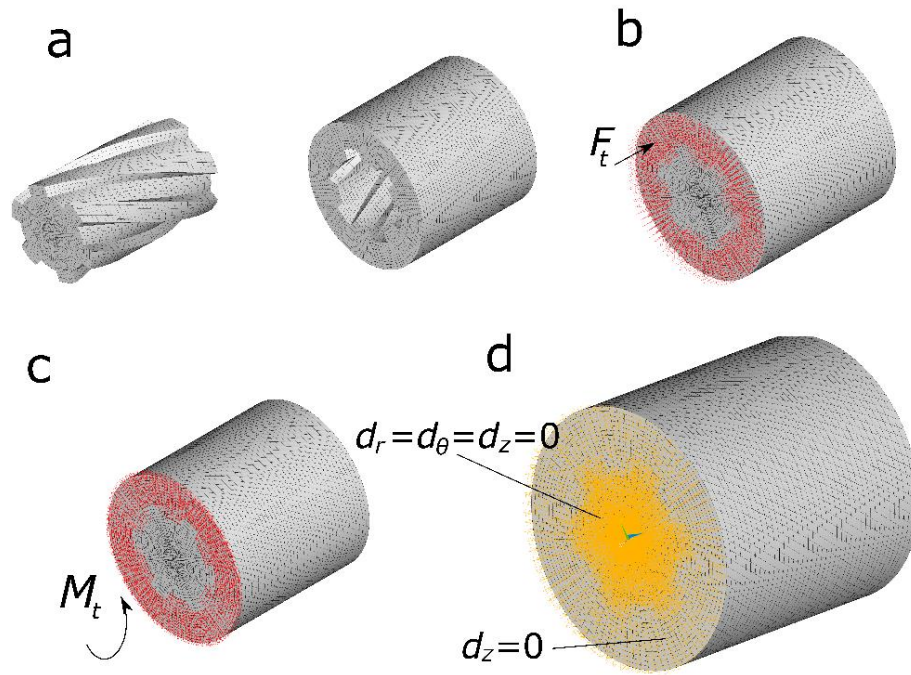


Figure 21: FEM model of helical spline coupling ( $\beta=70$  deg): a) mesh of shaft and hub, b) axial force loading, c) torque loading, d) boundary conditions

Numerical results evidence that statics of spline couplings obeys two important rules. Firstly, the load transfer through the spline due to the axial thrust  $F_t$  is small (6.7% of the thrust for  $\beta=135$  deg, i.e. the helical angle of maximum load transfer) and it is caused by deformations of the kinematic pair. In other words, if the hub and the shaft were perfectly stiff, the turbine thrust would not be transmitted at all to the shaft through the spline surfaces, but it would be carried by the constraint (4), i.e. the main axial bearing. Secondly, the load transfer  $R$  from the hub to the shaft through the spline due to the torque  $M_t$  is actually ruled by the following relationship, valid for a spline pair with perfectly stiff members:

$$R = \frac{M_t}{r_p \tan \beta} \quad (1)$$

where  $r_p$  is either the pitch radius in case of involute splines or the inner radius for parallel key splines.

Figure 22 compares the shaft and hub reactions computed by means of Eq. (1) and the FEM model with frictionless contact elements (torque load case). The shaft thrust is the reaction that the constraints exert on the grooved part of the shaft and it represents the load transfer  $R$  from the hub to the remaining part of the shaft through the spline surfaces. The hub thrust is equal and opposite according to Newton's 3rd Law. Therefore, in case of compliant

members, the rule defined by Eq. (1) is still valid with negligible error (0.6% of the transmitted load for  $\beta=135$  deg). Equivalently, the compliance of the cinematic pair members does not yield perceivable effects for the nominal value of torque  $M_t$ . Details of the FEM analyses will be published in the near future.

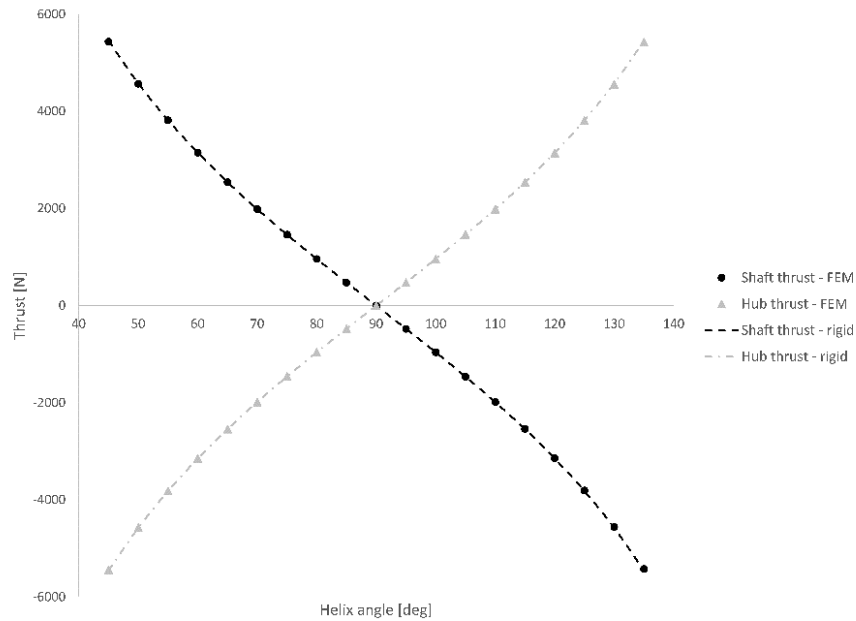


**Figure 22: Reactions of shaft and hub constraints for different helix angles under torque load**

### 6.6.5 Design of the support system

In the following, the above-explained laws of load distribution are used in order to choose the design parameters in the assumption, adopted for the sake of simplicity, that the members of the spline pair are stiff. Such assumption does not lead to significant errors, as proved above. By means of the resulting design procedure, the load distribution in nominal operating conditions between the two axial bearings can be set by means of a proper choice of the helical angle. To this purpose, Figure 23 shows for the data reported in Table 7 (case B) the load transfer through the coupling together with the corresponding axial loads of the bearings as a function of the helix angle  $\beta$  in nominal working conditions.

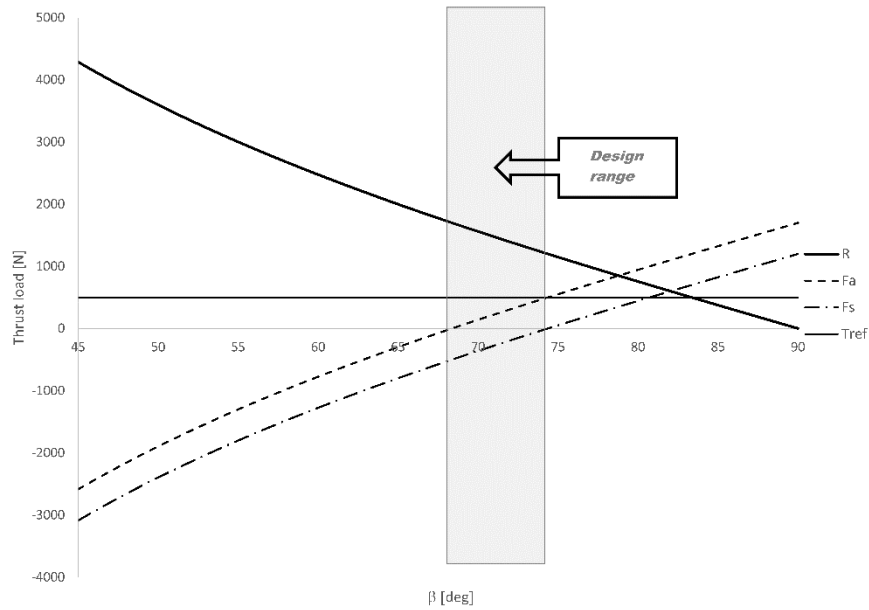


**Figure 23: Trends of axial bearing thrusts and load transfer as a function of helix angle in nominal operating conditions**

By assuming that positive torque acts on turbine impeller ( $M=M_t>0$ ), handedness of the helix must be chosen so that the load transfer  $R$  is directed as in Figure 19. In other words, the spline coupling must exert (equal) axial forces  $R$  opposite to  $F_t$  and  $F_c$  on the hub and the shaft, respectively. According to Eq. (1), such condition yields that the range of helix angle in the abscissa of the plot in Figure 23 cannot exceed 90 deg.

The load transfer  $R$  (thick solid curve) is plotted in Figure 23 according to Eq. (1). On the basis of its trend, the axial thrusts  $F_a$  and  $F_s$  that turbine and shaft respectively exert on the main bearing (4) and on the auxiliary bearing (3) are plotted as dashed and dash-dotted curves. They are respectively evaluated by means of the relations  $F_a = F_t - R$  and  $F_s = F_c - R$ , which can be deduced by the analysis of Figure 19, where turbine and compressor thrusts  $F_t$  and  $F_c$  are obviously constant in nominal operating conditions. The grey solid horizontal line represents the value of the reference load  $T_{ref} = F_t - F_c$ , which has to be carried by the single thrust bearing of a conventional machine. As reported in the paragraph dealing with layout and clearly visible in Figure 23, when a straight grooved spline ( $\beta = 90$  deg) is picked, the load acting on the main axial bearing (4) is greater than in a conventional plant. Indeed, it is equal to the total turbine thrust  $F_t$ , while the auxiliary axial bearing (3) supports the compressor thrust  $F_c$ .

By reducing the helix angle, the loads acting on both bearings begin to decrease, since the helix is oriented in such a way as to exert on the shaft and the turbine impeller a thrust  $R$  opposite to  $F_c$  and  $F_t$ , respectively (Figure 19). Particularly, by choosing  $\beta$  roughly equal to 74 deg, the main axial bearing (4) must carry the reference load ( $F_a=T_{ref}$ ), while the auxiliary one is axially unloaded and, therefore, since it is only subjected to the (light) radial load, it will have an average life exceeding 6 million hours, as specified in the first row of Table 5. Differently, for design values of  $\beta$  ranging between 68 and 74 deg, the load of the main bearing (4) becomes lower than the reference one, at the expense of the duration of the auxiliary bearing (3), on which the shaft exerts a negative thrust  $F_s$  (directed from the turbine to the compressor). For  $\beta=68$  deg the load on the main axial bearing (4) is null and, consequently, the thrust exerted by the shaft on the auxiliary bearing (3) assumes its maximum value, i.e.  $F_s=-T_{ref}$ . In such condition, the rolling element bearing (3) exhibits the same duration as in a conventional layout (e.g. see the basic rating life reported in the last two rows of Table 10). Obviously, since in the simplified layout of Figure 4 the main foil bearing is not double effect, helix angles lower than 68 deg, which moreover would lead to even more unsuitable life of the auxiliary bearing, are forbidden. A good design may require a helix angle slightly reduced in comparison with a value of 74 deg, where the amount of such reduction can be evaluated by taking into account the life and the reliability required for the bearing (3). In the design range, the highest life/reliability of auxiliary bearing (3) is obtained for  $\beta =74$  deg, while the lowest one, typical of a conventional layout, for  $\beta =68$  deg; the most severe loading case for the main axial bearing (4), equivalent to that of a conventional layout, occurs at  $\beta=74$  deg, the most favorable one (zero thrust) at  $\beta =68$  deg.

Finally, the actual assembly drawing of the new layout, suited to both case A and B of Table 7 as well as transient loading conditions is reported in Figure 24. In this case, the total hot clearance between runner (11) and pads (12) of the double-effect air bearing must be higher than that between turbine impeller (1) and the spacer (13) used to adjust the impeller axial clearance. The second set of (non-locating) angular contact bearings (14) is added.

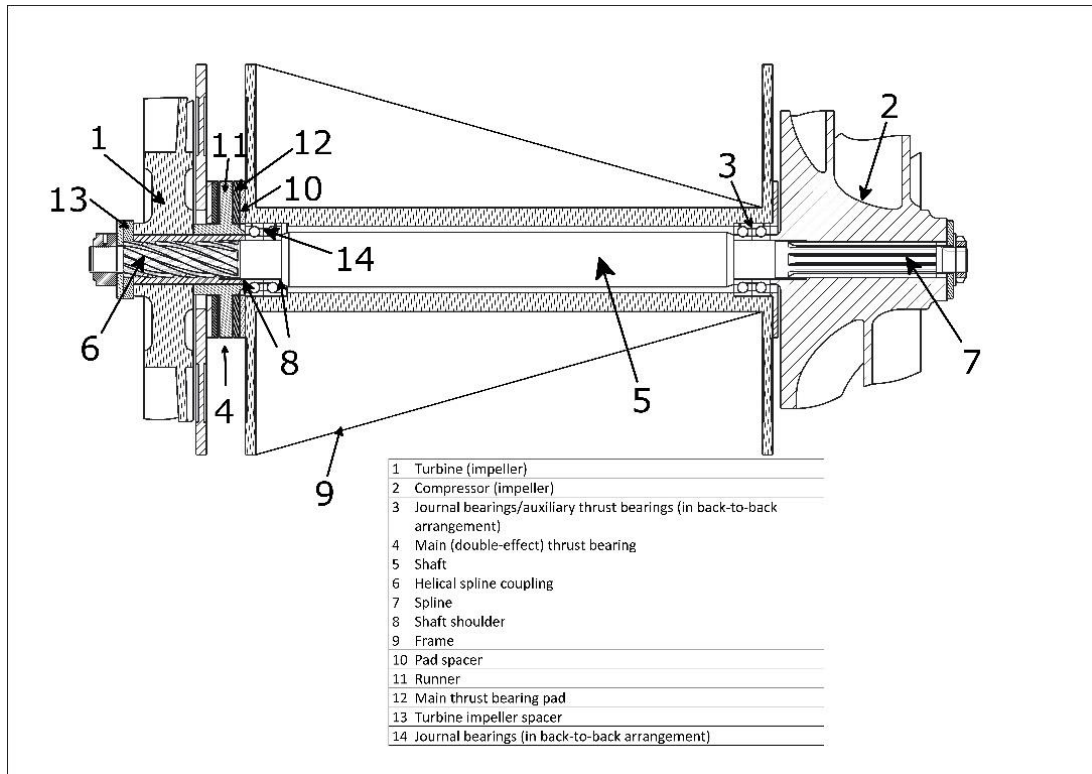


Figure 24: Section of the micro-GT support system assembly designed according to the invention

## 7 Radial inflow turbine design through multi-disciplinary optimization technique

---

### 7.1 Multidisciplinary optimization

Multidisciplinary design optimization (MDO) is nowadays widely employed to obtain advanced turbomachines design ([46], [47], [48]). The aim of this work is to provide a complete tool for the aero-mechanical design of a radial inflow gas turbine. The high rotational speed of such machines, especially if used for micro cogenerative power plants, coupled with high exhaust gas temperature, exposes blades to really high centrifugal and thermal stresses; thus the aerodynamics optimization has to be necessarily coupled with the mechanical one. Such an approach involves two different computational tools: a fully 3D Reynolds Averaged Navier-Stokes (RANS) solver is used for the aerodynamic optimization, while an open source Finite Element Analysis (FEA) solver is employed for the mechanical integrity assessment. The geometry parameterization is handled with a commercial tool that employs b-spline advanced curve for blades and vanes definition. The aerodynamic mesh generation is managed via dedicated tools provided by the CFD software and it is a fully structured hexahedral multi-block grid. The FEA mesh is built by means of a harmonic map approach, which is able to provide high quality second order unstructured grid preserving geometrical features starting from boundary surfaces of the fluid domain. The finite element calculation provides stresses, displacements and eigenmodes that are used for mechanical integrity assessments while the CFD solver provides performance parameters and local thermodynamic quantities. Due to the high computational cost of both these two solvers, a metamodel, such as an artificial neural network, is employed to speed up the process. The interaction between two codes, the mesh generation and the post processing of the results is obtained via in-house developed scripting modules. Results obtained are presented and discussed.

### 7.2 Introduction

In the last years micro-gas turbines used in cogeneration power plants have proved to be a promising technical solution for distributed combined production of electricity and heat, especially due to their low emissions and fuel flexibility. An effort should be made to improve performance of the micro-turbine in order to enhance cycle efficiency, taking it closer to internal combustion engines one. In particular, components efficiency heavily affects plant performance and aerodynamic design of novel geometries has to consider mechanical constraints in order to pursue this target without compromising machine integrity. Radial inflow turbines have compact design, good performance, and high power-to-weight ratio.

These features have made them ideal power units of micro-gas turbines, especially for microcogeneration applications [44], [45].

The preliminary design of the radial turbine impeller is usually based on empirical correlations and analytical procedures. The further aerodynamic design through CFD optimization techniques leads to the definition of a proper geometry configuration able to fulfill the requested aerodynamic performance and to monitor some peculiar aspects such as Mach number field and separation control along the meridional channel and blade incidence angle. On the other hand, geometrical parameters modification inevitably involves structural and mechanical aspects that have to be considered and taken into account. For example, a large lean angle can improve aerodynamic efficiency but, at the same time, induce high bending stress dangerous for the mechanical integrity of the impeller.

Nowadays, next steps of improvements are based on multidisciplinary optimization, because the aerodynamic design has to be strongly coupled with mechanical assessments ([49]-[51]). In fact, without considering this strong interaction, finding a satisfactory compromise solution would require many design iterations between aerodynamics and mechanical experts.

The proposed optimization procedure is focused on efficiency enhancement guaranteeing a safe turbine operation, by limiting stresses and avoiding resonances, disregarding the reduction of the moment of inertia, not crucial in the case study considered. Moreover, even though within a robust design procedure off-design performance have to be properly assessed, for the sake of clarity this work deals with design point operating condition.

A significant and relevant aspect of this work is the linking of aerodynamic design optimization (through commercial codes) and mechanical optimization through opensource software. In fact, for structural mesh generation and FEA calculations, only opensource software have been used; these tools have been coupled with CFD solver through appropriate Python and Fortran scripts. Further development will concern the introduction of opensource software also for the aerodynamic design.

### 7.3 Micro-gas turbine thermodynamic cycle

The concept design of the micro gas turbine starts from the analysis of a regenerative Brayton cycle suitable for the specific application.

The thermodynamic cycle parameters of the considered microGT are reported in Table 11. These values represent the state of the art of a 100 kW micro gas turbine technology available on the market. The calculations are carried out through the opensource in-house developed code GTcycle [76].

**Table 11: main cycle parameters for 100kW micro-gas turbine**

Parameters	Value
<i>Compressor efficiency</i>	80%
<i>Turbine efficiency</i>	86%
<i>Recuperator effectiveness</i>	84%
<i>Pinch point temperature difference</i>	70 °C
<i>Combustor efficiency</i>	95%
<i>Generator efficiency</i>	96%
<i>Mechanical efficiency</i>	99%
<i>Compressor pressure ratio</i>	4.5
<i>TIT</i>	950°C
<i>Recuperator hot pressure losses</i>	100 mbar
<i>Recuperator cold pressure losses</i>	150 mbar
<i>Combustor pressure losses</i>	175 mbar
<i>Intake pressure losses</i>	10 mbar
<i>Exhaust pressure losses</i>	10 mbar
<i>Cycle Efficiency</i>	30%
<i>Rotation speed</i>	75.000 rpm

**Table 12: Compressor reference conditions**

<b>Micro-turbine power</b>	100 kW
<b>Total pressure ratio (<math>\beta_{tt}</math>)</b>	4.5
<b>Compressor inlet total temperature</b>	288K
<b>Compressor Inlet total pressure</b>	101300 Pa
<b>Air flow rate</b>	0.74kg/s

Rotational speed	75000 rpm
------------------	-----------

## 7.4 Methodology

### 7.4.1 Radial inflow turbine overall performance evaluation

The boundary conditions for the design of the 90° radial inflow turbine, such as inlet total temperature and pressure ratio, have been defined by the optimum calculation of the thermodynamic efficiency of a regenerative Brayton-Joule cycle. In the present application the maximum turbine inlet temperature has been fixed to  $TIT = 1223$  K. It is due to the maximum thermal load that can be applied to nickel based superalloys, since the blades are not cooled. For this TIT a total-to-total pressure ratio of the cycle  $\beta_{\text{cycle}} = 4.4$  has been found to maximize the Brayton-Joule thermodynamic efficiency. It results in a total-to-total pressure ratio on the turbine of  $\beta_{\text{turbine}} = 3.7$ , once the pressure drop in the combustion chamber as well as in the exhaust diffuser are considered. Finally, a target mass flow rate of about  $\dot{m} = 0.75$  kg/s has been chosen in order to obtain the desired net output power of the system,  $P = 100$  kW.

### 7.4.2 Preliminary design approach

Once the boundary conditions are defined the following steps must be fulfilled to define the preliminary design of the machine, as classically stated by turbomachinery handbooks (see [49] and [50] for example):

1. Identification of the specific speed value maximizing the aerodynamic efficiency of the turbine from statistical data available from experiences (see [51]). This step allows the evaluation of the shaft speed. In particular a shaft speed  $n = 75000$  rpm gives a specific speed of  $n_s = 0.658$  radians, value well centred within the flat part at maximum efficiency ( $\eta \approx 0.9$ ) for the radial type turbines;
2. Literature analysis to determine relationships between dimensionless variables (such as load coefficient, blade number and geometrical parameters) as a function of specific speed. To this end recent works presented in the last 15 years at the ASME Turbo Expo conferences [52], as well as reported in works edited by the NASA Research Center and others fundamentals books [55] have been considered. All the selected works concern high efficiency design characterized by  $\eta > 0.86$ . Data reported in these works has been used to generate diagrams as the one shown in

Figure 1, where the loading coefficient ( $\psi = 2L_{1,2}/U_1^2$ ) is reported as a function of the specific speed ( $\bar{n}_s = n(\dot{m}/\rho_1)^{0.5}/L_{1,2}^{0.75}$ ). Note that in this case the specific speed is defined employing the density at the impeller inlet section, since literature data typically define the flow thermodynamic properties at the impeller inlet section. Our specific speed, based on the flow density at the machine exit  $n_s = 0.658$  (as defined at point 1) corresponds to  $\bar{n}_s = 0.484$ . The load coefficient distribution of Figure 1 allows the calculation of the impeller inlet diameter  $D_1$  (see also Equation(1) in the following). Similarly, also all the characteristic geometry ratios of the machine (made dimensionless with the impeller inlet diameter  $D_1$ ) and the impeller blade number can be obtained by linearly fitting literature data obtained from[55]. In the following a set of equations is reported for the main dimensionless geometries of the turbine (Equations (1)-(6)). Note that the narrow band of specific speed variation here considered allows a good representation of the curves like that of Figure 25 by means of linear relationships.

$$\psi = -2.99 \bar{n}_s + 3.59$$

$$\frac{b_1}{D_1} = 0.147 \bar{n}_s + 0.0069$$

$$\frac{b_2}{D_1} = 1.60 \bar{n}_s - 0.416$$

$$\frac{D_{2\_mean}}{D_1} = 0.849 \bar{n}_s + 0.0061$$

$$\frac{\Delta x}{D_1} = 1.003 \bar{n}_s - 0.15$$

$$N = -5.73 \bar{n}_s + 16.32$$

3. Once the main geometrical dimensions of the radial inflow turbine are defined by means of the previous set of equations, both the shroud and the hub lines describing the meridional channel can be obtained connecting the edge points with elliptical profiles. As described by [60] it can be considered a good starting point, and it will be later optimized in order to reduce as much as possible the velocity over-speed at shroud radius, that may eventually induce boundary layer separation;

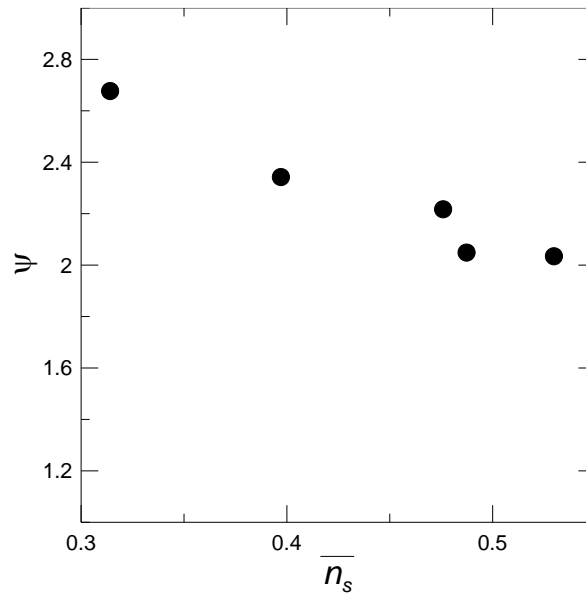


**Figure 25: Loading coefficient vs specific speed. Data have been extracted from literature [52][53][54][56][57][58][59]**

4. Impeller inlet and exit angles should now be set. Impeller inlet angle has been fixed to  $\beta = 0^\circ$  in order to minimize bending stresses and creep strains (that in turn allows to increase as much as possible the turbine inlet temperature, thus the thermodynamic efficiency of the cycle). The radial distribution of the exit flow angle was imposed in order to have an absolute flow angle aligned with the axial direction at the machine axis (thus minimizing viscous losses on the exhaust cone), while an absolute flow angle of around  $\alpha = 10^\circ$  has been imposed at the tip radius to minimize losses in the outlet diffuser. Here in fact the pressure gradient pointing toward the axis induced by the swirling flow promotes transition to turbulence of the boundary layer at the casing, thus reducing the risk of separation [60].
5. Slip effects at the rotor inlet are accounted for by means of the Stanitz's relation (Eq. (7)). In this way, once fixed the impeller relative inlet angle (thus the absolute flow angle at the impeller inlet since the peripheral velocity is known) it is possible to determine the vane exit flow angle as a function of the impeller blade number.

$$\tan\alpha_{1'} = \tan\alpha_1 (1 - 2/N) \quad (7)$$

Since inside the vane the flow is strongly accelerated by the reduction of the passage section (due to the radii reduction), here the flow can be reasonably assumed to be a potential flow (see [51]). Thus the flow angle here determined by Equation(7) can be reasonably assumed to correspond to the geometrical throat angle of the vane row;

6. Vane inlet and exit diameters are again determined by means of statistical relations coming from literature[59]:

$$D_0/D_1 = 0.344 \bar{n}_s + 1.11 \quad (8)$$

$$D_{1'}/D_1 = -0.14 \bar{n}_s + 1.096 \quad (9)$$

7. The whole geometrical dimensions and flow angles computed following the procedure described from point 1 to point 6 have been slightly adjusted in order to properly match the present boundary conditions, especially in terms of mass flow rate and work to be exchanged. Moreover, also some limitations introduced during this phase of the design contribute to slight modifications of the geometrical parameters as described from point 1 to 7, namely:

- absolute Mach number at the vane exit smaller than  $Ma_{1'} < 1$ ;
- relative Mach number at the tip of the impeller exit section  $Ma_{r2} < 1$ .

The preliminary design of the whole machine here described is used as starting point for the optimization procedure described in the next sections.

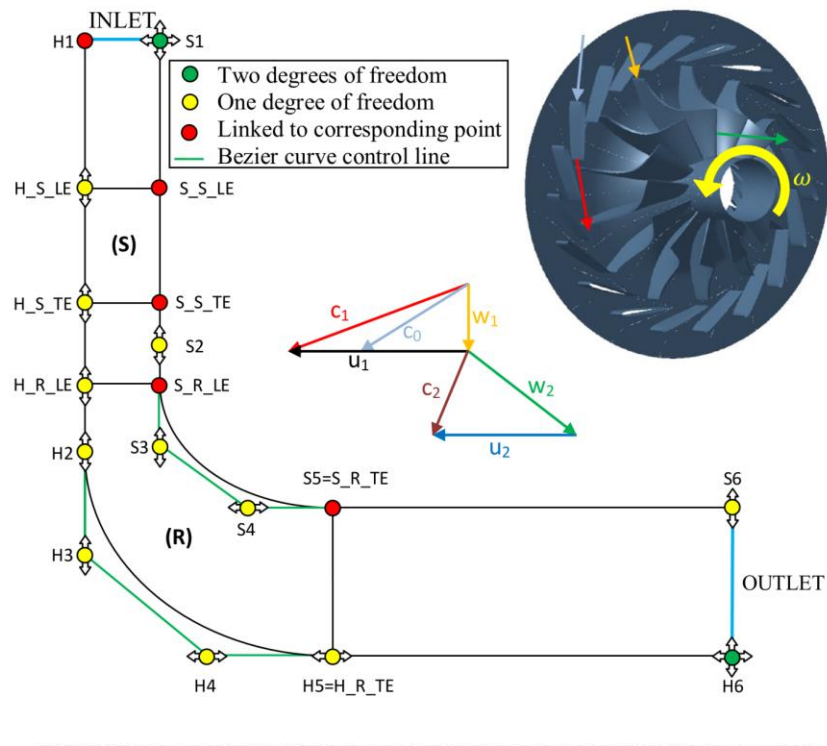


Figure 26: Meridional channel contours, control points and angles convention

### 7.4.3 3D model parameterization and meshing

The three-dimensional representation of the machine is defined by the meridional channel geometry, the stator and rotor blade camber line and thickness curves and by the definition of blade positions along the channel.

In order to obtain a useful model to be employed within the optimization module, it is necessary to parameterize the machine geometry via parametric curves. Thus, the software Autoblade [61] has been employed.

#### *7.4.3.1 Meridional channel parameterization*

Both hub and shroud contours present a fully radial line part, followed by a curvilinear part, and terminate with another line, directed in axial direction. Thus for the first and the last contours a simple line is employed to parameterize the channel, while for the central curvilinear part a Bezier curve, with 4 control points is employed. The free coordinates point, able to be modified by the optimization procedure, are indicated in Figure 26. Several control points can move only along one direction: in fact in order to guarantee slope continuity between successive curves, and in order to link some hub and shroud points each other, these points must have only one degree of freedom.

#### *7.4.3.2 Stator blade definition*

For stator geometry definition, since the blade is not twisted, only one spanwise section is employed, set in the middle of the channel. The blade sections are stacked on the leading edge. As previously mentioned, the blade geometry is defined when the camber and the thickness laws are defined. For camber law definition, a simple Bezier line is used (Figure 27).

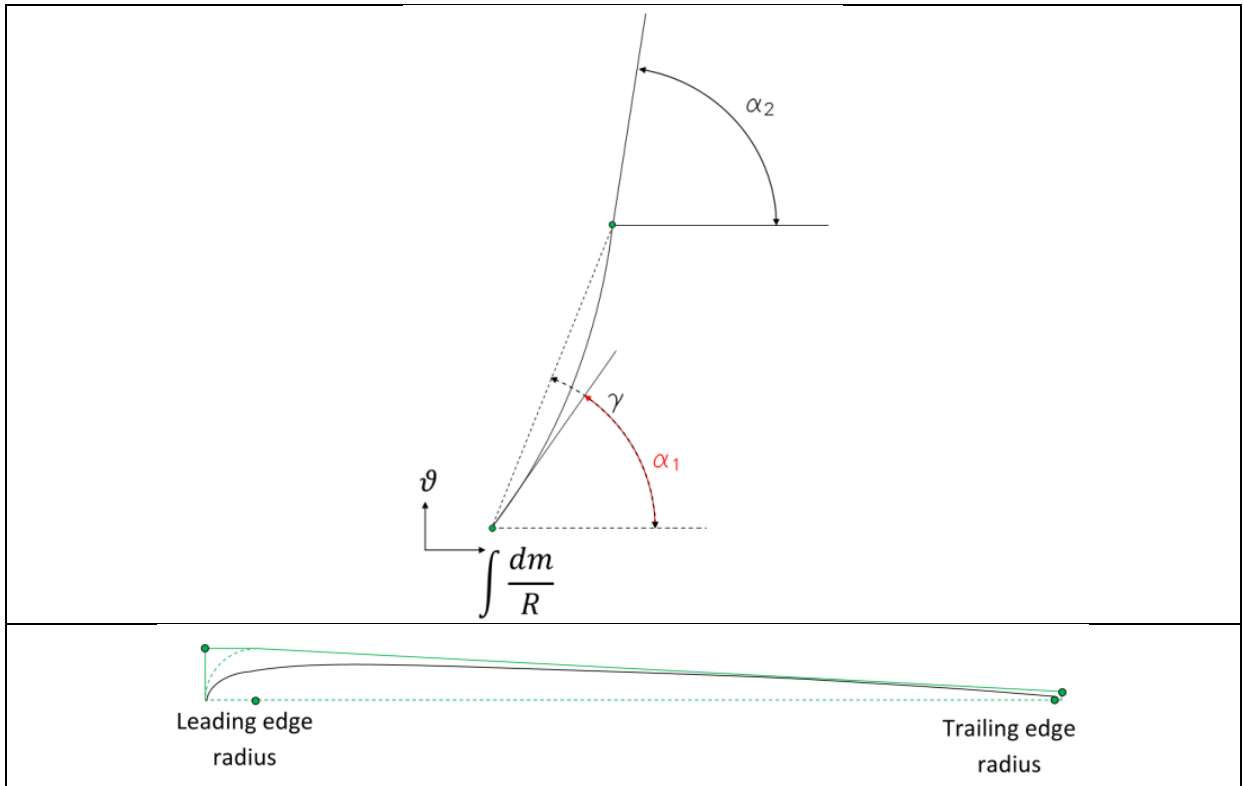


**Figure 27: Stator blade camber and half-thickness law parameterization**

The inlet metal angle is set in accordance with inlet boundary conditions, while the outlet metal angle is varied during the optimization procedure. The stagger angle is imposed as the average value between inlet and outlet metal angles previously determined.

The thickness law is defined as thickness addition on the camber curve and it is symmetric on pressure and suction side. A simple two parameter law, which employs the leading and trailing edge radii, is used, as sketched in Figure 3.

The leading and trailing edge locations are specified by imposing the values of radii on hub and shroud (indicated as  $H\_S\_LE$  and  $H\_S\_TE$  in Figure 2).

Finally, the number of blades is free to vary.

#### 7.4.3.3 Rotor blade definition

For rotor blade parameterization three spanwise sections are defined. Since the blade is first radially and gradually axially oriented, a  $\int \frac{dm}{R} - \vartheta$  plane has been employed for geometry definition. As for stator row, the three spanwise sections are stacked on the leading edge. For the camber line parameterization a Bezier curve, controlled by 4 points not equally distributed along the curve, has been employed for each spanwise section. This parameterization allows, by imposing the same value of  $\vartheta$  for the first two control points, to

obtain a quasi-rectilinear zone in the beginning part of the camber line, as sketched in Figure 28.

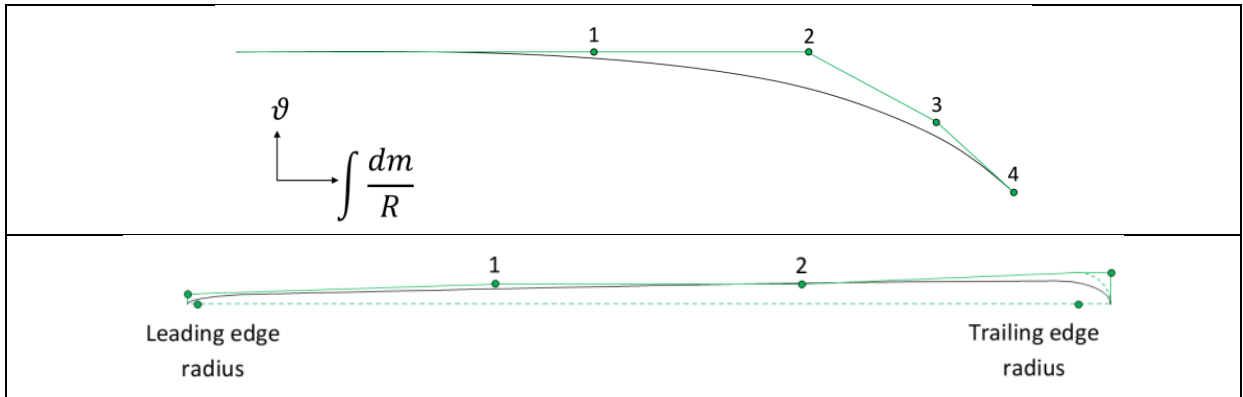


**Figure 28: Rotor blade camber and half thickness law parameterization**

The third and the fourth control points allow to modify the stagger and the outlet blade metallic angle. In addition, the blade lean angle is free to vary. The lean angle defines the inclination in the tangential direction of the leading edge line of the blade.

For thickness law definition, a Bezier curve with four control points is employed. Also for rotor row a symmetric law, defined by thickness addition to camber curve has been chosen. Two control points are defined, as made for the stator row, by leading and trailing edge radii. Two additional points are employed to control the value and the position of blade maximum thickness (indicated with 1 and 2 in Figure 28). The values of blade thickness are fixed at tip section, and a linear interpolation between hub and tip values is employed to calculate the blade thickness of the midspan section.

The leading and trailing edge positions are controlled by the values of the leading edge radius and trailing edge axial position on hub (indicated as  $H\_R\_LE$  and  $H\_R\_TE$  in Figure 26). Also for rotor row, the number of blades is free to vary in order to be optimized in the multidisciplinary optimization procedure.

In conclusion, with the previously discussed assumptions, the total number of design parameters, which will be managed by the optimization procedure, is 22.

#### 7.4.3.4 Mesh generation

Once the parametric model is set up, the entire fluid domain has to be meshed. The meridional channel is subdivided in 56 geometrical streamlines.

For both stator and rotor blade a Numeca Autogrid [61] default topology has been chosen. In order to obtain a  $y^+$  lower than unity, the first cell width has been set to  $2.5e^{-06}$  mm, using the empirical evaluation law suggested by Numeca.

The stator row is meshed with about 500.000 grid nodes, while the rotor row requires about one 1.000.000 of nodes. The mesh shroud gap is defined with a constant value of 0.2 mm along the rotor blade tip. Thus the entire mesh, which has to be introduced in the optimization algorithm, consists of 1.5 million nodes.

## 7.5 Optimization strategy

The optimization strategy, as previously discussed, is to combine the aerodynamic optimization algorithm implemented in Fine/Design3D [61] with CalculiX [62], a free open source FEA. The detailed description of the aerodynamic optimization method is reported in [63]. This procedure has been employed also for 3D axial and centrifugal turbomachinery blades optimizations ([64]-[68]), while a recent application provided by the Authors on centrifugal compressor return channel optimization is presented in [69].

From the mechanical point of view, the optimization procedure is based on the opensource finite element software CalculiX, through properly defined in-house developed macros for stress and frequency assessment. These results are used to define the multidisciplinary objective function employed by the optimization algorithm. Every sample analysed through CFD for evaluating its aerodynamic performance is also verified for its structural behaviour.

### 7.5.1 Aerodynamic optimization process

The method is based on the minimization of a properly defined objective function, modelled through an artificial neural network (ANN). The ANN is defined by setting the number of layers and a solutions database provided by CFD calculation obtained via DoE technique. After the training, the genetic algorithm (GA) employs the ANN as a meta-model in order to find the partial optimum solution, which is verified through a CFD calculation. The result is inserted in the database to update the ANN training. This procedure is repeated for the desired number of optimization iterations.

The domain considers both the stator row and the radial impeller, with a mixing plane interface between the rotating and the stationary domain. Boundary conditions are in accordance with those used for 1D design previously described. Total conditions and flow angle have been set at the inlet section and averaged static pressure is imposed at the outlet section. The effects of turbulence is considered by means of  $k\omega$ -SST turbulence model.

### 7.5.2 Geometrical constraints

In order to reduce the number of geometrical parameters inside the optimization procedure, some constraints have been introduced. For the meridional channel contour, the first three points for both hub and shroud curves (indicated with H1, H2, H3 for the hub and with S1, S2, and S3 for the shroud in Figure 26) have the same axial coordinate. Similarly, the last three points (indicated with H4, H5, H6 for the hub and with S4, S5, and S6 for the shroud) have the same radial coordinate. These assumptions allow to obtain a radial inlet duct and an axial outlet duct, with slope continuity in curve connections. Furthermore the inlet section is set at constant radius, while the outlet is set at constant axial coordinate.

For the blade construction, to reduce the number of parameters to be optimized, the leading and trailing edges of stator row are set at constant radius. Similarly, for rotor blade, the leading edge has been set at constant radius, while the trailing edge is set at constant axial coordinate. Furthermore, the leading edge is imposed at the same axial coordinate of the hub and shroud points which controls the final position of meridional channel Bezier curves.

In order to allow the initial hub definition line to be extended beyond the rotor leading edge, the corresponding control point (indicated with H2 in Figure 26) is free to move independently from the corresponding shroud points (indicated with S2). To define the H3, H4, S3 and S4 point range of free movement, the following kind of law has been introduced:

$$v = v_{\min} + \delta_v(v_{\max} - v_{\min}) \quad (10)$$

Where  $v$  is the free geometric coordinate value,  $v_{\max}$  and  $v_{\min}$  its maximum and minimum allowable values and  $\delta_v$  a real variable ranging from 0 to 1. Thus the position of these points is function of the parameter  $\delta_v$ , which will be modified by the optimization procedure.

### 7.5.3 Database generation

For the turbine geometry optimization, as the number of variables is quite high, a 15X random sample is chosen. In fact, other schemes would lead to too expensive database generation. Each parameter is split in five different values, and about 350 sample CFD calculations, chosen with a pseudo-random technique called “random among discrete levels”, are employed. Each computation is run in serial (2.5 hours on modern CPU), but the overall database generation is split over several CPUs.

### 7.5.4 Aerodynamics objective function

The objective function for turbine geometry optimization process, to be minimized, is made up of several penalty terms:

$$P_{aero} = P_{\dot{m}} + \sum_{i=1}^4 P_{MAX\alpha_{OUT,i}} + \sum_{i=1}^4 P_{MIN\alpha_{OUT,i}} + P_{MAX\eta_{t-s}} \quad (11)$$

where

$$P_{\dot{m}} = W_{\dot{m}} \left( \frac{\dot{m}_{nom} - \dot{m}}{\dot{m}_{nom}} \right)^2 \quad (12)$$

$$P_{MAX\alpha_{OUT,i}} = \begin{cases} 0 & \text{if } \alpha_{OUT,i} < \alpha_{OUTMAX,i} \\ W_{\alpha_{OUT,i}} \left( \frac{\alpha_{OUTMAX,i} - \alpha_{OUT,i}}{\alpha_{OUTMAX,i}} \right)^2 & \text{if } \alpha_{OUT,i} \geq \alpha_{OUTMAX,i} \end{cases} \quad (13)$$

$$P_{MIN\alpha_{OUT,i}} = \begin{cases} W_{\alpha_{OUT,i}} \left( \frac{\alpha_{OUTMIN,i} - \alpha_{OUT,i}}{\alpha_{OUTMIN,i}} \right)^2 & \text{if } \alpha_{OUT,i} < \alpha_{OUTMIN,i} \\ 0 & \text{if } \alpha_{OUT,i} \geq \alpha_{OUTMIN,i} \end{cases} \quad (14)$$

$$P_{\eta_{t-t}} = W_{\eta_{t-t}} (1 - \eta_{t-t})^2 \quad (15)$$

The aim of this function is to drive the optimization process to ensure a mass flow rate equal to design condition (Equation (12)), to keep the outlet tangential velocity in a desired range along spanwise direction (sampling the values on four spanwise sections, (Equations (13)-(14)) and to maximize the overall total to total efficiency (Equation (15)). Each term is made non dimensional by using suited reference values.

**Table 13: Aerodynamic weighting functions**

Weight	Value
$W_{\dot{m}}$	20
$W_{\alpha_{OUT,i}}$	1
$W_{\eta_{t-t}}$	40

The values of the weighting functions used within aerodynamic objective function, as stated in Eq. (12) – (15), are summarized in Table 13. These values have been imposed by considering that the main goal was total to total efficiency maximization, by preserving as much as possible the mass flow rate and keeping, if possible, the outlet flow angle spanwise distribution in a desired range.

## 7.6 Structural analysis

### 7.6.1 Procedure description

Aerodynamic geometry of blade and channel is provided by NUMECA CFD calculations in STL (STereoLithography) format. Then, in order to create, always in STL format, the two periodic surfaces, the back and the front hub faces of the impeller, a Python script has been implemented.

Normally during this procedure some errors can occur (e.g. facet orientation, degenerate facets), so, in order to obtain a robust optimization procedure, a further step has been defined: all STL triangles are checked and, in case, fixed by ADmesh, an opensource program for processing triangulated solid meshes.

After that, mesh is exported to GMSH, an open source three-dimensional finite element mesh generator, developed by Christophe Geuzaine and Jean-François Remacle ([70],[71]).

GMSH creates the 3D mesh of quadratic tetrahedral elements, by using the Delaunay algorithm; for stress analysis each mesh has approximately 160.000 nodes and 100.000 elements. For modal analysis, that has to be carried out for a large number of nodal diameters (see [72][73][74]) in order to decrease computing time, the number of nodes and elements has been reduced to 60.000 and 45.000 respectively. This reduction has been possible because modal analysis is less sensitive to mesh refinement and, consequently, also poor mesh gives very satisfactory results. In fact, a sensitivity analysis has been carried out, providing the average frequency discrepancy between the finer and the coarser model which is lower than 0.5%. FEM analyses, i.e. thermal, stress and modal, have been carried out by using CalculiX, a free and opensource finite element tool [62].

### 7.6.2 Thermal analysis

For thermal analysis a simplified approach has been adopted, by imposing adiabatic temperatures coming from CFD solver NUMECA (interpolating from CFD to FEA mesh through a FORTRAN script) and by setting appropriate heat transfer coefficients and bulk temperatures in the zones not in contact with the main flow.

This assumption has been set basing on two reasons:

- main goal of the implemented optimization procedure is to enhance turbine aerodynamic efficiency, limiting global stresses and controlling blade eigenfrequencies, but without optimizing impeller fatigue and creep behaviour, for which a very accurate thermal field is crucial;
- conjugate heat transfer (CHT) approach would have largely increased computational time.

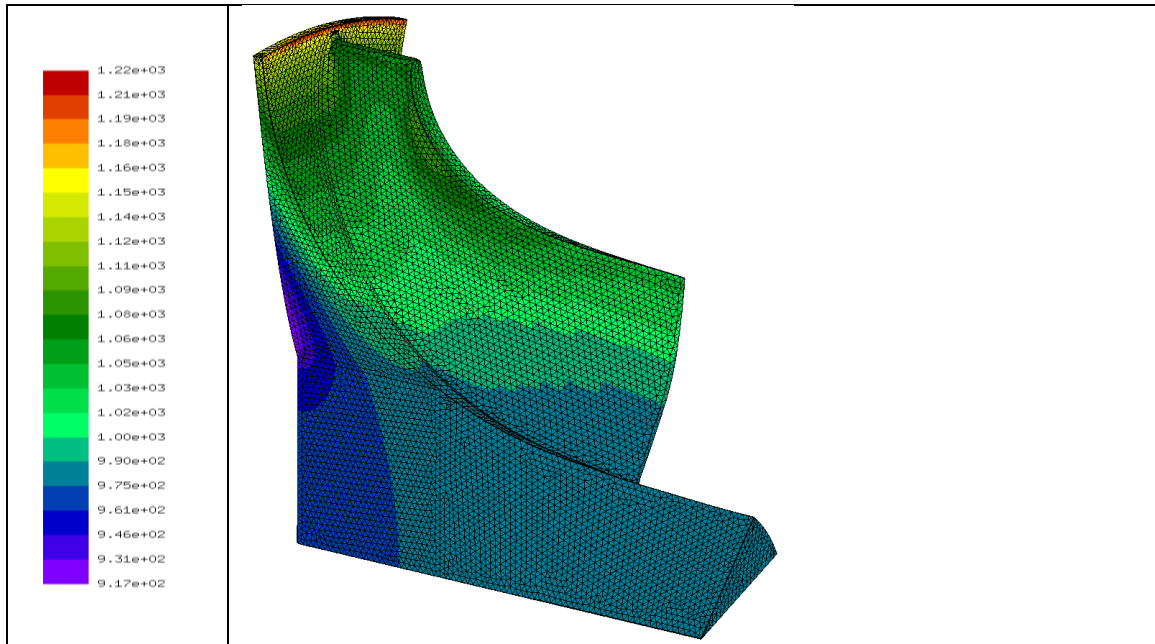


Figure 29: Example of field temperature on preliminary sample [K]

Moreover, periodic boundary conditions are applied, such that only a  $1/N_{rotor}$  part of the geometry needs to be analyzed. In Figure 29 it is reported the thermal distribution on the preliminary sample.

### 7.6.3 Thermomechanical analysis

The thermomechanical analysis is performed applying three types of loadings:

- nodal temperatures coming from previous thermal analysis;
- static pressure distribution calculated by NUMECA, interpolating from CFD to FEA mesh through a FORTRAN script;
- centrifugal force, by setting a rotational speed of 75.000 RPM.
-

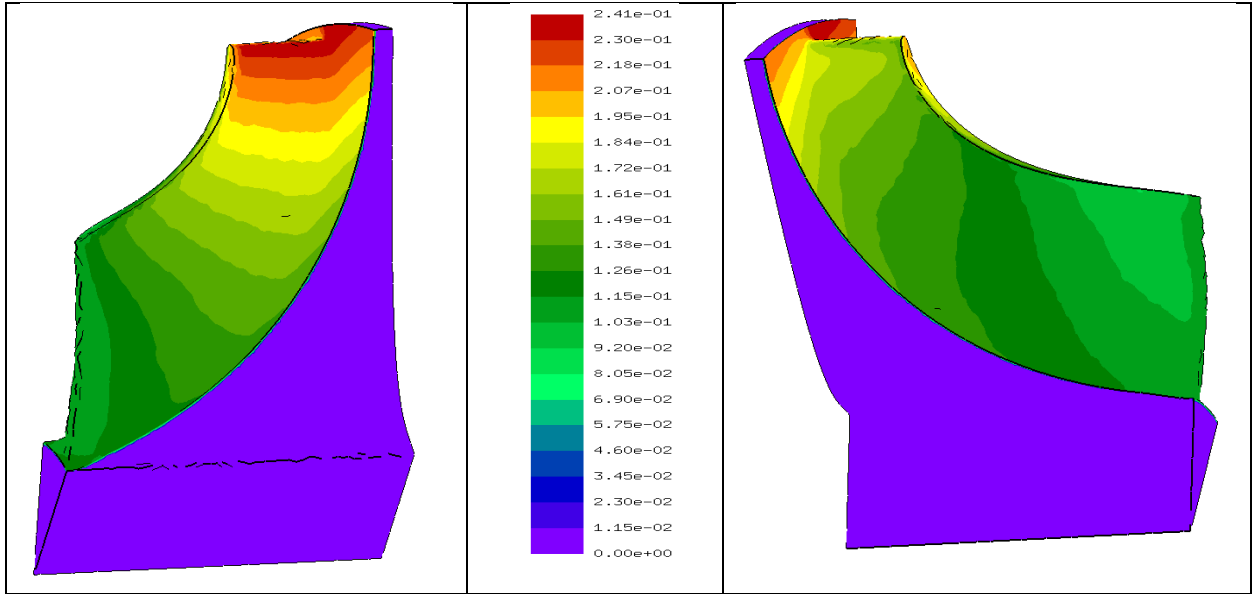


Figure 30: Pressure distribution [MPa] – pressure and suction side

Appropriate constraints on displacements are applied in the FEA model. The materials model is linear-elastic, and geometrically nonlinear effects are taken into account. In the periodic surfaces of the impeller, adequate boundary conditions are applied, such that only a  $1/N_{rotor}$  part of the geometry can be simulated. Once the calculation is performed, temperature and Von Mises stress fields of the blade are then extracted. For a preliminary assessment an allowable stress has been defined, based on yield strength, expressed as a function of temperature, according to the following expression:

$$\sigma_{all} = \frac{a_1 T^6 + a_2 T^5 + a_3 T^4 + a_4 T^3 + a_5 T^2 + a_6 T + a_7}{SF} \quad (16)$$

where SF is a safety factor and  $a_1$  properly defined constants. Then, Von Mises stresses of each blade node have been compared to the allowable ones, consequently defining the penalty factor:

$$P_{stress} = \begin{cases} W_{stress} \left( \frac{\sigma_{max}}{\sigma_{all}} \right)^2 & \text{if } \sigma_{max} \geq \sigma_{all} \\ 0 & \text{if } \sigma_{max} \leq \sigma_{all} \end{cases} \quad (17)$$

#### 7.6.4 Modal analysis

As mentioned before, modal analysis is carried out using a model with a reduced number of nodes and tetrahedral quadratic elements, in order to speed up the computation.

Even in this case adequate boundary conditions have been applied, such that only a  $1/N_{rotor}$  part of the geometry can be simulated.

Since the disk is rotating and subjected to pressure and thermal loadings, there is a preload. Therefore, the first step is a nonlinear geometric static analysis in order to calculate the deformation and stresses due to this loading; this preload is taken into account in the calculation of the stiffness matrix in the frequency calculation.

Depending on number of blades, there are different numbers of nodal diameters. In particular, the maximum number of nodal diameters in the impeller is half the number of blades (for an even number of blades). For an impeller having an odd number of blades, the maximum nodal diameter is  $(N_{rotor} - 1)/2$ .

Through a script which modifies CalculiX input deck, the correct number of nodal diameters is specified; then eigenfrequencies are extracted and an assessment is performed.

The major source of excitation considered are the vanes and the first four Engine Orders (EO); the frequency of vane excitation force is a function of the number of nozzles and the speed of the turbine. The shape of this force is determined by the number of nozzles.

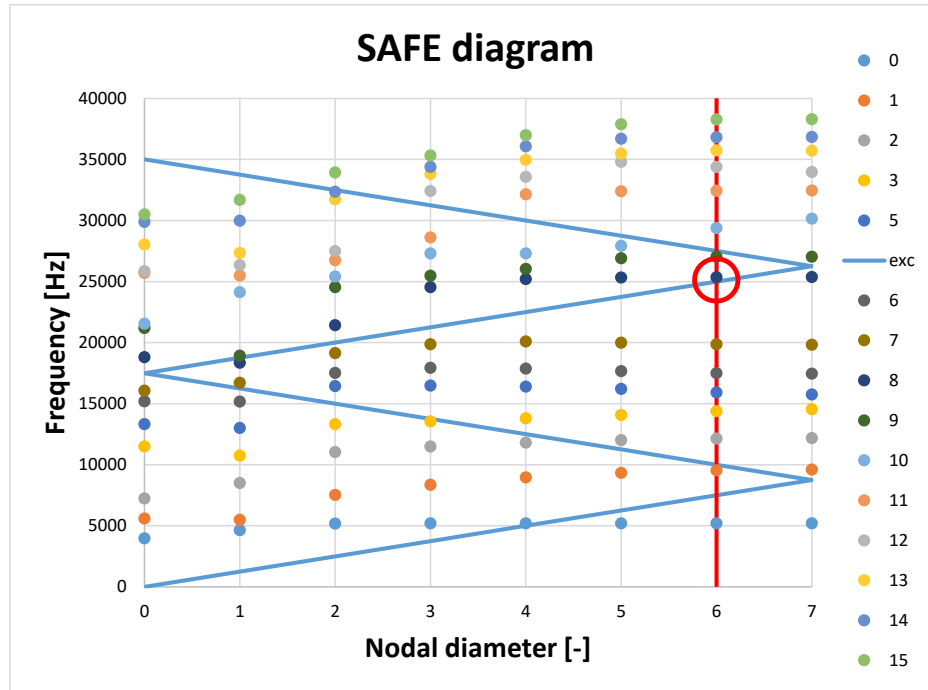


Figure 31: SAFE diagram of preliminary sample

Vane excitation is of higher harmonics than  $N_{rotor}/2$ ; it can be shown that the engine orders that can excite a tuned disk mode satisfy the following equation:

$$L = |nN_{rotor} \pm M| \quad (18)$$

where n is an integer.

In order to clarify the concepts expressed before, a discussion on Figure 7 is reported; this figure represents the SAFE diagram, a tool that compares not only exciting harmonics frequencies with blade eigenfrequencies, but also the shape of these harmonics with the normal mode shapes of a completely bladed wheel ([73][74][75]). In the legend, the families of mode shape are represented by coloured points, while the exciting force is represented through a blue line. Preliminary sample has 20 vane blades and 14 rotor blades.

With  $L = 20$ ,  $n = 1$  and  $N_{rotor} = 14$  the nodal diameter  $M$  that satisfies Eq. (18) is 6; the exciting frequency is:

$$f_{NPF} = f_{ROT} N_{vane} = 25.000 \text{ Hz} \quad (19)$$

So, resonance could occur at nodal diameter 6, at 25.000 Hz, in the red circle depicted in Figure 31.

According to that, a FORTRAN script has been developed, in order to extract eigenfrequencies and check possible resonances at the correct nodal diameter, taking into account that both  $N_{rotor}$  and  $N_{vane}$  are variable parameters.

Main target is to avoid that eigenfrequencies are in the range 0.95-1.05 of the exciting frequencies, so a penalty factor has been defined accordingly:

$$P_{freq\_low} = \begin{cases} W_{freq\_low} \left( \left| \frac{f_{eigfr}}{f_{exc\_low}} - 1 \right| - 0.05 \right)^2 & \text{if } \left| \frac{f_{eigfr}}{f_{exc\_low}} - 1 \right| \leq 0.05 \\ 0 & \text{if } \left| \frac{f_{eigfr}}{f_{exc\_low}} - 1 \right| \geq 0.05 \end{cases} \quad (20)$$

$$P_{freq\_high} = \begin{cases} W_{freq\_high} \left( \left| \frac{f_{eigfr}}{f_{exc\_high}} - 1 \right| - 0.05 \right)^2 & \text{if } \left| \frac{f_{eigfr}}{f_{exc\_high}} - 1 \right| \leq 0.05 \\ 0 & \text{if } \left| \frac{f_{eigfr}}{f_{exc\_high}} - 1 \right| \geq 0.05 \end{cases} \quad (21)$$

Thus, the structural analysis objective function can be obtained as the sum of the previously described terms:

$$P_{Struc} = P_{Stress} + P_{Freq\_low} + P_{Freq\_high} \quad (22)$$

**Table 14: Mechanical weighting functions**

	Value
$W_{stress}$	16
$W_{freq\_high}$	10
$W_{freq\_low}$	10

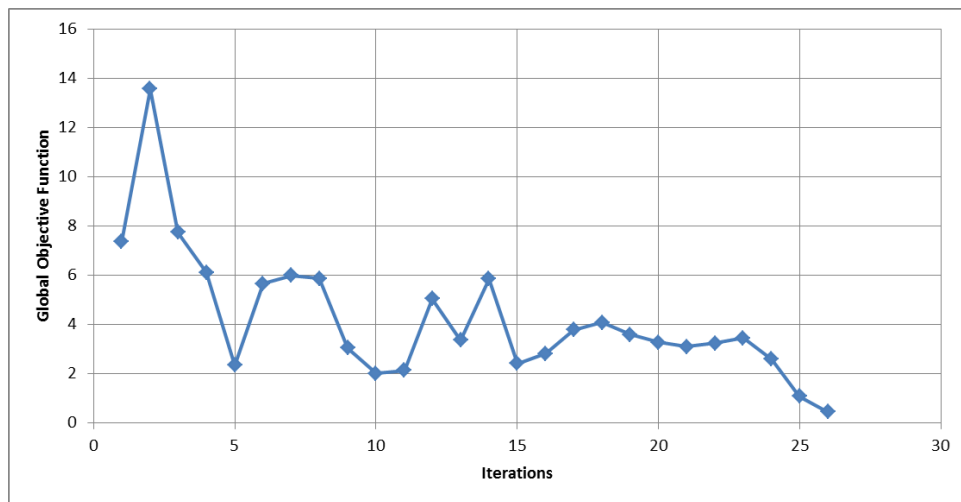
The values of the weighting functions used within mechanical objective functions, as stated in Equations (17), (20) and (21), are summarized in Table 14.

## 7.7 Results

Once the aerodynamics and structural objective functions have been chosen, the optimization procedure will find the optimum solution for the overall objective function defined as:

$$P = P_{Aero} + P_{Struct} \quad (23)$$

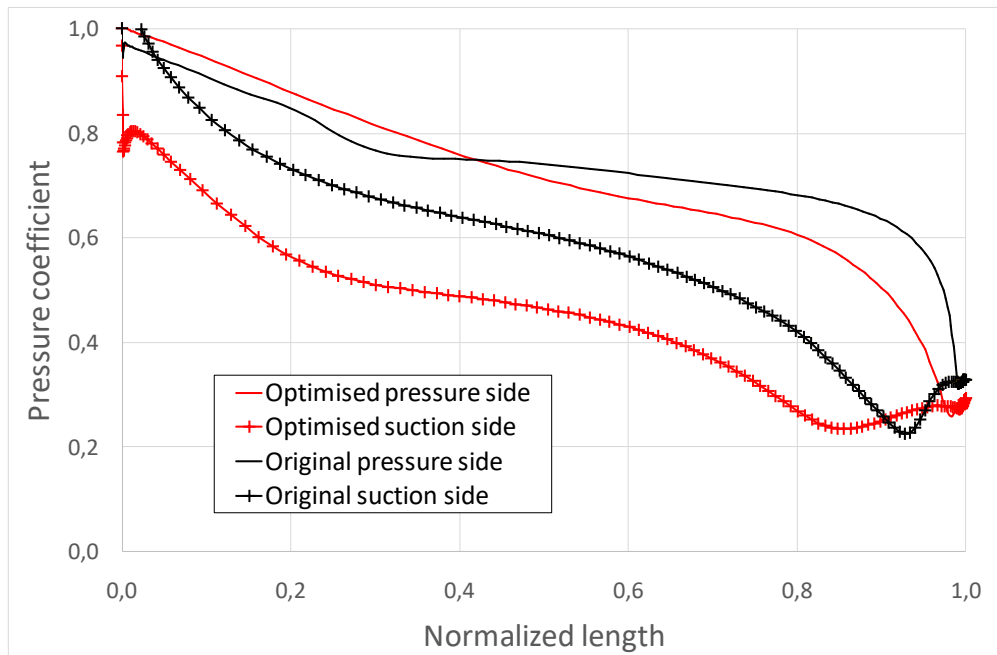
The optimization process has been set to 30 iterations. In Figure 8 the convergence history during the optimization process of  $P$  is plotted. In order to understand the phenomena driving the optimization procedure previously discussed, the blade loading distributions in the form of static pressure coefficient  $c_p$  at midspan are reported in Figure 9 for both the baseline and the optimized geometries.



**Figure 32: Overall objective function convergence history**

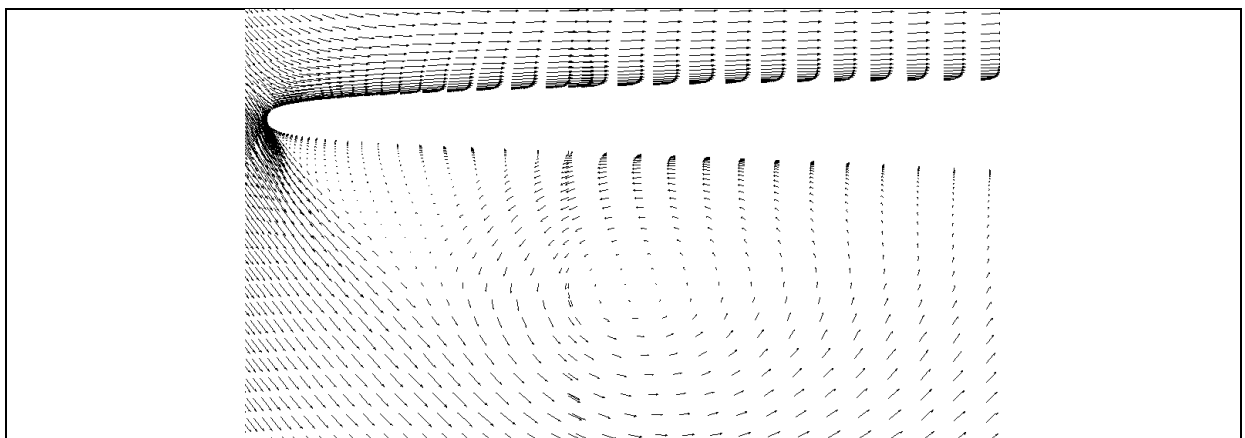
It has to be noted that, as reported in Table 15, since the mass flow difference between baseline and optimized configuration is not negligible, comparisons reported are affected both by the optimized design and by different operating point.

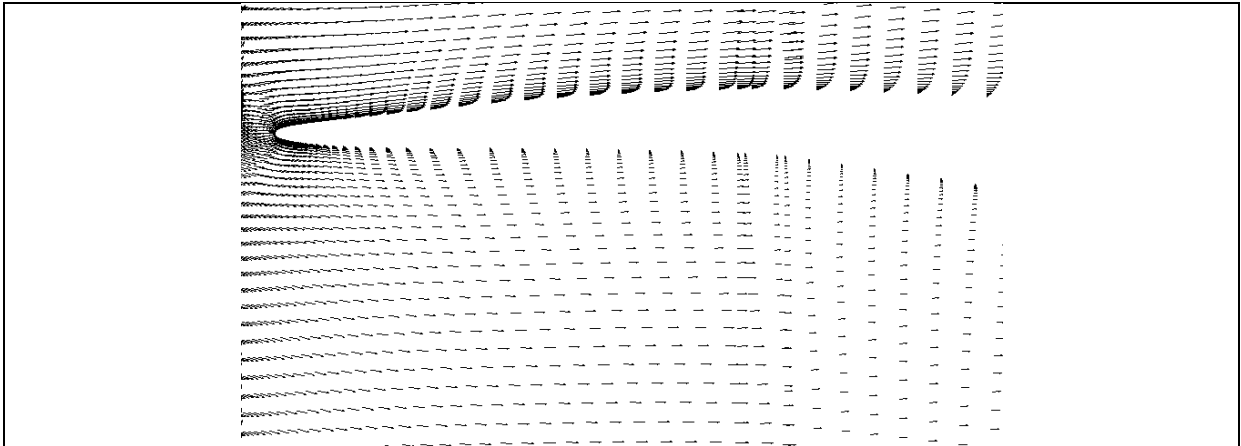
For the baseline configuration (black curves) the pressure and the suction side lines intersect just behind the impeller leading edge, suggesting the occurrence of a pressure side boundary layer separation due to excessive negative incidence angle condition. The wrong relative inlet flow angle induces the formation of a recirculating flow region, as it is clearly highlighted by the vector map reported on the top of Figure 34.



**Figure 33: Pressure coefficient diagram for original and optimized configuration at midspan**

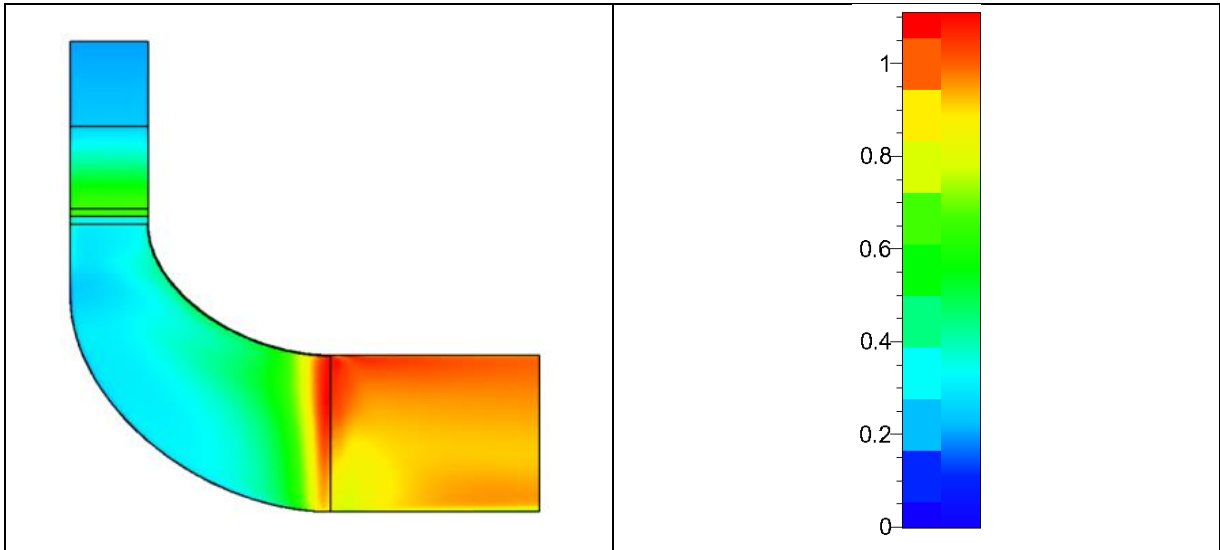
In the optimized case the optimization tool increases the tangential component of the absolute velocity at the rotor inlet (reducing the channel height and raising the absolute exit flow angle from the stator blade), thus minimizing the incidence angle at the impeller leading edge. This re-establishes a right incidence condition to the impeller, as shown by the load distribution in the optimized case (see the red lines in Figure 33), as well as by the absence of recirculating flow region in the vector map reported on the bottom of Figure 34.





**Figure 34: Velocity vector for original (top) and optimized configuration (bottom) at midspan**

As a consequence, a higher Mach number at the stator blade trailing edge is obtained for the optimized configuration, as shown in the colour plot of Figure 35, where both the absolute and relative Mach number distributions in the meridional plane (characterizing the stator and the rotor blades, respectively) are reported.



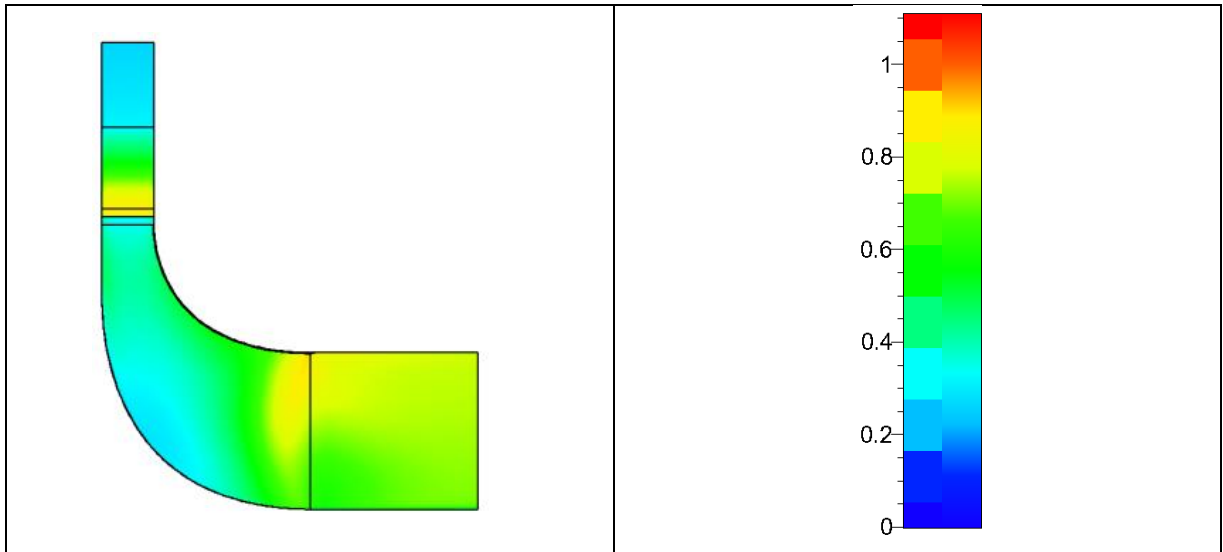


**Figure 35: Absolute (on the stator region) and relative (on the rotor region) Mach number distributions in the meridional plane: original (top) and optimized (bottom) configurations**

In the original configuration the pressure coefficient distribution in the rear part of the blade also shows a sudden increase of static pressure just prior to the blade trailing edge. It is due to the occurrence of a shock wave close to the blade trailing edge, since the relative Mach number becomes transonic in this flow region.

Indeed the colour plot of Figure 35 (on the top) clearly highlights flow regions characterized by  $Ma_r > 1$ . The steep pressure increase induced by the shock wave also causes large viscous losses due to penalties in the suction side boundary layer evolution.

This high relative Mach number characterizing the original case also sets excessive mass flow rate elaborated by the turbine as compared with the target value. Thus, the optimization procedure acts reducing the mass flow rate sensibly modifying the impeller width at the entrance, but keeping the same blade height at the outlet section (see Figure 35). This implies a reduction of the exit relative Mach number, which becomes subsonic in the optimized case.

Both sonic and viscous effects observed in the original case contribute to enlarge the entropy production in the rear part of the impeller, as it is made evident by the entropy fields shown in Figure 36.

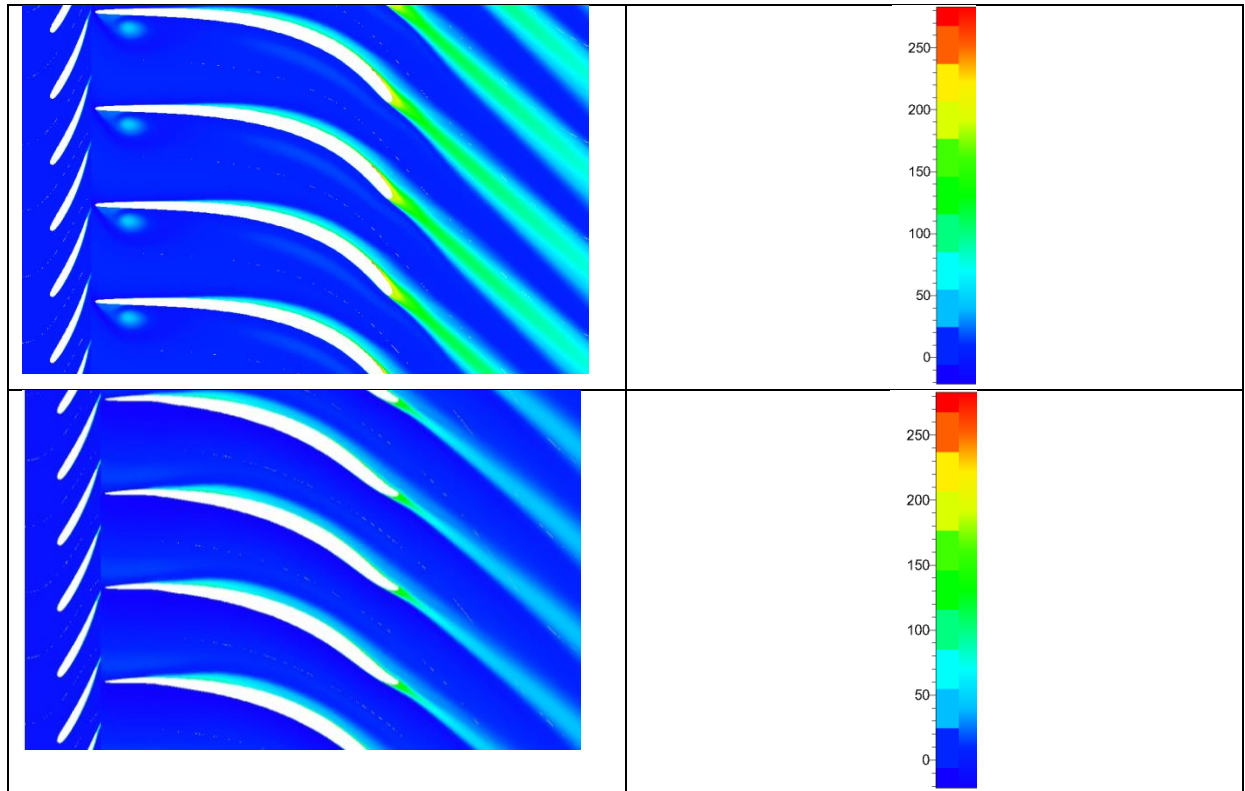


Figure 36: Entropy field (expressed in J/kgK) for original (top) and optimized configuration (bottom) at midspan.

Indeed, excepted for the pressure side region close to the blade leading edge (where the flow recirculation in the original case induces further additional losses), the main differences between the original and the optimized cases can be observed only in the last part of the rotor blade suction side. Here the aforementioned viscous and sonic phenomena tend to significantly increase the loss production rate. The wake flow region of the optimized case is indeed evidently thinner and characterized by smaller entropy, thus explaining the increased aerodynamic efficiency obtained after the optimization procedure. To this end the original and optimized overall performance are summarized in Table 15.

Table 15: original and optimized overall performance

	Original	Optimized
$\dot{m}$ [kg/s]	0.907	0.769
$\eta_{t-t}$ [-]	0.872	0.927
Power [kW]	250.24	246.17

$U/C_0$	0.655	0.651
<i>Stress usage factor</i> [–]	2.54	0.98
<b>Resonance 4EO</b>	Yes	No
<b>Resonance NPF</b>	Yes	No

For what concerns the structural optimization, Figure 37 shows the Von Mises stress field for original and optimized configurations: in the original configuration there is a high stress mainly due to the lean angle of the blade. The optimized configuration shows a lower level of stress; the stress peak is concentrated in the fillet radius, where local plastic strains are allowed. Aerodynamic and structural optimizations act simultaneously in the proposed optimization procedure, thus extracting the better solution in accordance with the definition of the overall objective function defined in Equation. (23).

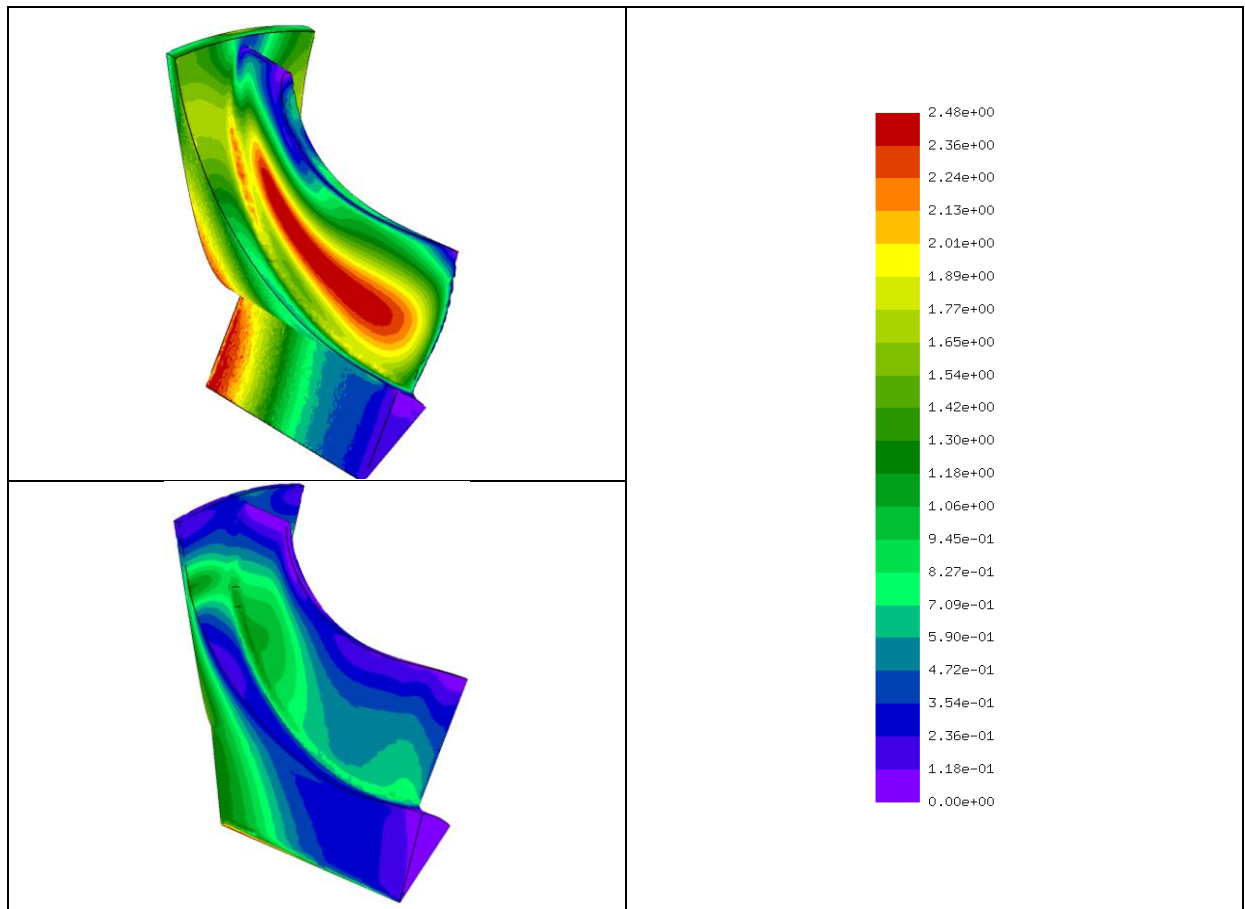


Figure 37: Non dimensional Von Mises stress field for original (top) and optimized configuration (bottom)

In Table 16 the original and the final optimized values for penalty functions are reported.

**Table 16: original and optimized penalty functions**

	<b>Original</b>	<b>Optimized</b>
<b><i>P</i></b>	7.364	0.443
<b><i>P<sub>Aero</sub></i></b>	6.9086	0.4024
<b><i>P<sub>Struc</sub></i></b>	0.4554	0.0406

## 8 Multi-disciplinary optimization of a centrifugal compressor for micro-turbine applications

---

### 8.1 Introduction

The present chapter presents the multi-disciplinary optimization of the centrifugal compressor for a 100kW micro-gas turbine. The high rotational speed fixed by the cycle optimization (75.000rpm) requests a simultaneous analysis of flow aerodynamics and mechanical stress to account for the high centrifugal stresses the blades are subjected to, while maximizing the aerodynamic performance. A commercial 3D computational fluid dynamics (CFD) solver adopted for the aerodynamic computations and an open source finite element FEM code for the mechanical integrity calculations are coupled with metamodels to speed up the optimization process. In-house scripting modules, which manage multidisciplinary optimization, mesh generation, geometry parameterization and result post-processing have been written and utilized. Once generated the sample data-base on the basis of the parameters selected to describe aerodynamic and mechanical constraints, an optimization procedure based on a genetic algorithm has been performed. A RANS steady approach with a two-equation SST (Shear Stress Transport) model have been adopted for the aerodynamic computations during the optimization procedure. The optimized compressor so achieved showed an important boost in aerodynamic performance, without any penalty in the mechanical stresses, as compared with the baseline design. The optimized configuration has been tested also by means of URANS phase-lag investigations, which highlighted even a larger increase of the aerodynamic performance as compared with the one predicted by RANS calculations.

In recent years the application of micro-gas turbines in cogeneration power plants has been found to be a promising solution for the distributed combined production of electricity and heat. To enhance the cycle efficiency, the improvement of the performance of micro-gas turbine components plays a fundamental role. Due to the small size of micro-gas turbines, radial machines are generally preferred thanks to their compactness and high power-to-weight ratio.

These qualities make the centrifugal compressors widely employed in small-scale energy conversion systems, and explain the increasing interest in the improvement of their performance through numerical and experimental analyses aimed at studying the flow development in existing machines ([77][78][79]) and through the adoption of advanced optimization procedures for the design phase ([80][81][82][83][84][85][86][87]).

For what concerns the design of the centrifugal compressor, the high rotational speed exposes blades to high centrifugal stresses, which lead to severe structural constraints. For this reason, a multidisciplinary optimization, which increases the aerodynamic performance of the machines simultaneously fulfilling the structural constraints, is essential to speed up the design process ([88][89][90]).

The preliminary design configuration is generally optimized from the aerodynamic point of view through CFD calculations, in order to reduce the relative Mach numbers at the impeller inlet lip and the risk of shock waves, which have detrimental effects on the impeller performance, as well as to improve the rotor/stator interaction and the diffuser performance, hence reducing the overall losses. The aerodynamic optimization gives rise to new geometrical and kinematic parameters which may not respect the mechanical constraints, with the consequent requirement of several iterations to reach a satisfactory solution, when a traditional approach, which performs the mechanical analysis only at the end of the optimization procedure, is adopted. If a novel approach, such as the one applied to a centrifugal compressor by Verstraete et al., which simultaneously accounts for both aerodynamic and structural constraints, is followed, the optimization procedure becomes considerably less time-consuming.

The present work is focused on the design and optimization of a centrifugal compressor for micro-turbine application. Starting from a preliminary design based on 1-D equations, empirical data and statistical analysis, which allow the selection of the ranges of variation for the main parameters, a multi-objective optimization is then performed to reach an optimized configuration with higher aerodynamic performance obtained still respecting the mechanical constraints. Home-made scripting modules, which manage multidisciplinary optimization, mesh generation, geometry parameterization and results post-processing are adopted. The compressor design process is based upon two steps: the first one consists in the database generation that investigates machine performances, by generating samples in a multidimensional geometrical space; in the second step an optimization loop, which is based on a genetic algorithm and involves both multilayer perceptron (MLP), CFD (RANS calculations) and FEM code, is carried out. The blades and meridional channel geometries are parameterized by means of high-order Bezier curves. Starting from the fluid-dynamic mesh, a FEM grid with second order elements is built and linear elastic simulation as well as modal analysis are performed. These computations provide stresses, displacements and eigenmodes, that are used for mechanical integrity assessments.

The main parameters of the baseline and optimized compressors, as well as the most significant aerodynamic results are compared to give a physical justification of the aerodynamic performance improvement. Moreover, the results obtained by means of

URANS analyses on the optimized compressor are also shown to confirm, in a more realistic environment, the performance improvement predicted by the RANS investigations.

## 8.2 1d design approach

The centrifugal compressor, which the optimization procedure has been applied to, has been designed starting from a one-dimensional preliminary approach aimed at fulfilling the design duty with the best machine efficiency, taking also account of mechanical limitations of the materials.

In this first design step the principal dimensions and blade angles have been found applying 1D equations, starting from empirical data and statistical analyses to fix the ranges for the main unknown design parameters.

Successively, the flow within the compressor has been analyzed by CFD 3D simulations to verify the 1D design approach.

The compressor working conditions have been fixed by the micro turbine cycle analysis, which identified the pressure ratio and the machine rotational speed able to optimize the cycle efficiency, and the mass flow rate necessary to achieve the nominal power, once fixed the pressure ratio.

The small mass flow rate favored the choice of a 3D radial compressor, which is able to guarantee the desired pressure ratio with a single stage machine.

For the preliminary design, a computer program written starting from the procedure suggested by Vavra [91], extending the equations applicability to the cases of not purely radial blades at the impeller discharge and of absolute inlet velocities not in the axial direction, has been adopted.

The one-dimensional design should fix the following parameters:

- peripheral velocity at the impeller outlet ( $u_2$ );
- impeller radius ( $R_2$ ) and width at the exit ( $b_2$ );
- inner ( $R_{1i}$ ) and outer ( $R_{1o}$ ) radius at rotor inlet;
- relative blade angle at  $R_{1o}$  ( $\beta_{1o}$ ) and at  $R_2$  ( $\beta_{b2}$ );
- absolute flow angle at  $R_2$  ( $\alpha_2$ );
- radius at the inlet lip of the diffuser inlet ( $R_3$ ) and at the diffuser outlet ( $R_4$ );
- number of impeller blades ( $Z_R$ ) and diffuser vanes ( $Z_v$ ).

Some design limits should be imposed to take into account fluid dynamic and mechanical constraints.

The relative Mach number at the impeller inlet ( $Ma_{r1}$ ) and the absolute Mach number at the diffuser inlet ( $Ma_2$ ) should be contained to reduce as much as possible the supersonic flow regions and the associated shock losses.

The peripheral velocity  $u_2$  is limited by the permissible rotor stresses to about 400m/s for steel unshrouded wheel impellers, and to about 650 m/s for Ti impellers ([92] [93]).

The radius ratio  $R_{1o}/R_2$  should not exceed 0.7-0.75 [91] to obtain acceptable shroud curvatures in the meridional plane, whereas the ratio  $R_{1i}/R_{1o}$  should be enough large in order to permit the arrangement of a sufficiently large number of rotor blades with reasonable thickness (not less than 0.3-0.4) and not compromise wheel efficiency.

A backsweep angle should be adopted at the impeller exit to increase the degree of reaction and consequently the stage efficiency.

The ratio between the blade width and the impeller exit radius ( $b_2/R_2$ ) should be larger than 0.08 [91] to reduce disk friction losses and improve the efficiency. The maximum deceleration ratio  $w_2/w_{1o}$  and the maximum flow deflection ( $\beta_{1o} + \beta_2$ ) should be contained to avoid boundary layer separation.

Once fixed the compressor efficiency, the wheel efficiency as well as the slip factor (on the basis of a statistical analysis), and chosen the impeller exit angles, the peripheral velocity at the impeller outlet necessary to guarantee the desired pressure ratio can be calculated. Since for the present case the rotational speed has been already fixed from the preliminary cycle analysis to optimize the compressor-turbine matching, the impeller outlet radius is directly determined. Fixing the  $R_{1o}/R_2$  rate on the basis of the previous considerations, and  $\beta_{1o}$  to a value which gives an acceptable  $Ma_{r1}$ , the values of  $R_{1i}$  and  $b_2$  can be deduced from the mass flow rate. For these calculations the actual flow area is considered by the introduction of blockage factors which take into account the displacement thickness of the boundary layers at the two sections. The radius at the diffuser inlet and outlet sections have been selected on the basis of a statistical analysis carried out on the existing high-efficiency centrifugal compressors with the same specific speed.

The main geometrical parameters found with this procedure have been compared with the limits imposed by the flow physics and with the ranges found by the statistical analysis. The procedure described above has been iterated, changing the initial design parameters, until the aforementioned main fluid dynamic and mechanical constraints have been fulfilled.

The main geometrical parameters and angles fixed by the preliminary design are reported in Table 17.

**Table 17: Compressor preliminary design geometrical parameters**

$R_{1i}/R_{1o}$	<b>0.41</b>	$\beta_{1i}$	<b>45°</b>
$R_{1o}/R_2$	<b>0.68</b>	$\alpha_2$	<b>71°</b>
$b_2/R_2$	<b>0.092</b>	$\beta_{b2}$	<b>30°</b>
$\Delta x/R_2$	<b>0.56</b>	$\alpha_{b4}$	<b>38°</b>
$\delta_b/b_2$	<b>0.05</b>	$Z_R$	<b>12+12</b>
$\alpha_{1o}$	<b>0°</b>	$Z_v$	<b>20</b>
$\beta_{1o}$	<b>68°</b>	$R_3/R_4$	<b>0.65</b>

### 8.3 Parameterization of the 3d geometrical model

The three-dimensional representation of the whole centrifugal compressor is defined by the meridional contours of hub and shroud, the impeller main blade, impeller splitter blade and diffuser camber line, thickness distribution, meridional and tangential stacking law so as, obviously, by the number of blades of each row. It's necessary to choose a proper set of parametric curves in order to identify the most appropriate geometrical topology that allows designer both to manage different geometrical shapes via a limited number of key parameters automatically inside an optimization environment and to explore all the feasible configurations for the involved row. The commercial software Numeca/Autoblade [93] has been employed for this purpose.

#### 8.3.1 Meridional channel parameterization

Since the requested centrifugal compressor has a low specific rotational speed number it is a fully radial outflow turbomachine, it turns flow from axial direction to radial one. Moreover the hub and shroud walls are axi-symmetric, that means they can be geometrically parameterized using only the hub and shroud meridional projection curves. For achieving axial-to-radial configuration both hub and shroud contours present the same geometrical topology: an axial line part, followed by a curvilinear part, to end it up with another line, radially directed. Thus for the first and the last stretch a straight segment, limited between two control points, has been employed to parameterize the channel, while a Bezier curve, with 4 control points, has been selected to represent the central curvilinear part.

If each control point coordinates have to be defined, 32 variables would be needed for the six geometrical entities: 4 and 8 variables for each straight segment and third order Bezier curves respectively. For the curve continuity it is necessary to force, for each path, the end point to be equal to the starting point of the next path. Thus 12 independent points (24 variables) remain.

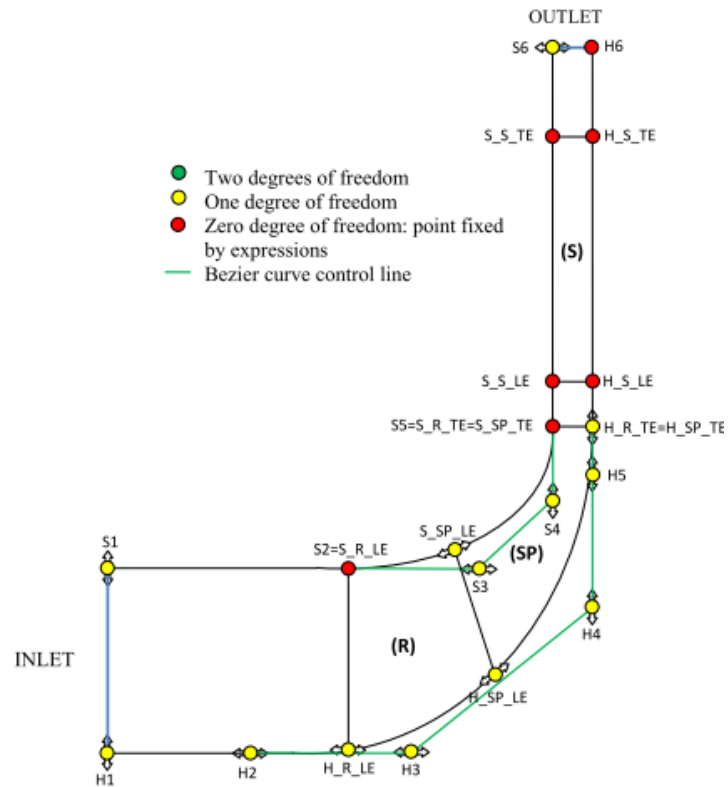


Figure 38: Channel and blades meridional track with their control points

In order to guarantee regular contours up to first derivative, the slope must be the same in each junction point for adjoining paths. Both hub and shroud walls have two junction points, one adjoining straight line to Bezier curve, the other linking Bezier curve to straight line. Hence, with the additional  $C^1$  continuity assumption, 4 degrees of freedom are removed with a total of 20 independent variables remaining in the meridional channel model, corresponding to the  $z$  and  $R$  coordinates of the free control points. Among these ones only a few are effectively allowed to move (they are reported in Figure 38), due to imposed geometrical constraints that are stated in the dedicated paragraph.

### 8.3.2 Impeller row definition

The impeller row is made up of a main blade and a splitter blade. Both of them are twisted and tapered, hence they have been defined on three spanwise sections: on hub, shroud and the axial-symmetric surface at midspan in order to be able to represent just mentioned spanwise variations. The  $\int dm/R - \vartheta$  profiles construction plane has been selected since the most intuitive  $m - R\vartheta$  plane does not preserve angles except when cylindrical sections are employed. Impeller main blade is stacked on leading edge (LE); LE meridional projection is a line controlled by extreme points  $H\_R\_LE$  and  $S\_R\_LE$  respectively on hub and shroud wall, as reported in Figure 38. LE shape in the  $\vartheta - span$  frontal plane is linear too, controlled by its slope and its starting tangential position at hub (null by default). The meridional location of main blade is fully set by adding trailing edge (TE) definition, linear between  $H\_R\_TE$ , on hub, and  $S\_R\_TE$ , on shroud.

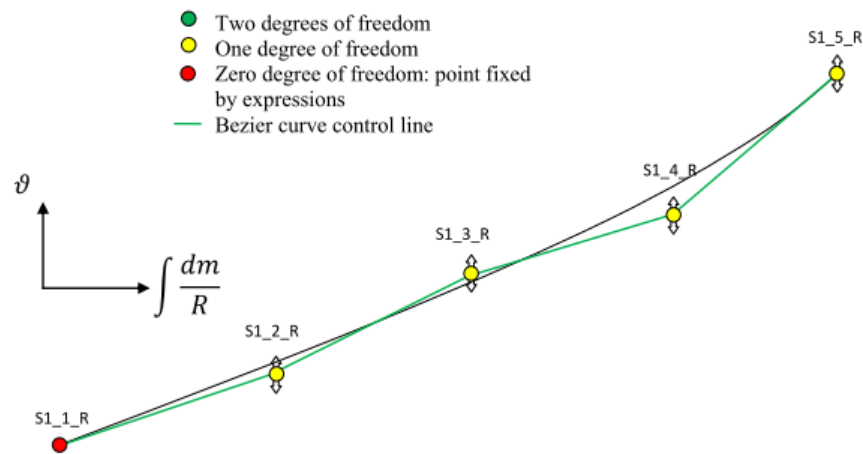
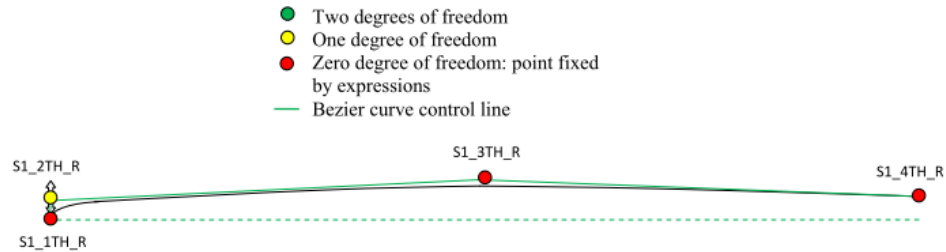


Figure 39: Impeller main blade camber parameterization on section at hub

For main blade camber parameterization a Bezier curve, controlled by 5 points equally distributed along the  $\int dm/R$  abscissa, has been employed for each spanwise section; among these control points the first one is automatically positioned by LE stacking law (Figure 39). Inlet and outlet camber metallic angle are not explicitly present within camber parameterization; due to the important role they assume  $\beta_{b1}$  and  $\beta_{b2}$  have been introduced as user defined variables in place of the second and fourth control point. The suction and pressure sides have been defined adding a symmetric half-thickness profile perpendicular to camber curve. For half-thickness law definition, a Bezier curve with 4 control points has been employed on each spanwise section. The first control point is rigidly joined to main blade LE while the second one can vary in order to control the LE radius amplitude. The third one is

located in the middle of camber abscissa and tunes the maximum thickness of profile; the last trims the profile so as to obtain a blunt TE (Figure 40).



**Figure 40: Impeller main blade half-thickness law parameterization on section at hub**

The camber shape and half-thickness law of splitter are inherited from the corresponding ones of main blade. On each spanwise section splitter profile is tangentially placed in the middle of main blade channel while along meridional direction it starts at an arbitrary position and ends at main blade TE. The number of splitter is equal to main blade one. Therefore the impeller row model presents 30 independent variables potentially able to move; restrictions will be put by geometrical constraints.

### 8.3.3 Diffuser row definition

The diffuser row is made up of rectilinear wedge-shaped blades. They are cylindrical, unleaned and not tapered blades, therefore they have been defined only by means of an hub surface profile axially extruded up to intersect shroud surface. The  $m^* - \beta$  profiles construction plane has been selected since it's the most convenient plane to achieve a rectilinear camber curve inside Autoblade. Profiles stacking and meridional extension of blade are defined in the same way of impeller main blade ones.

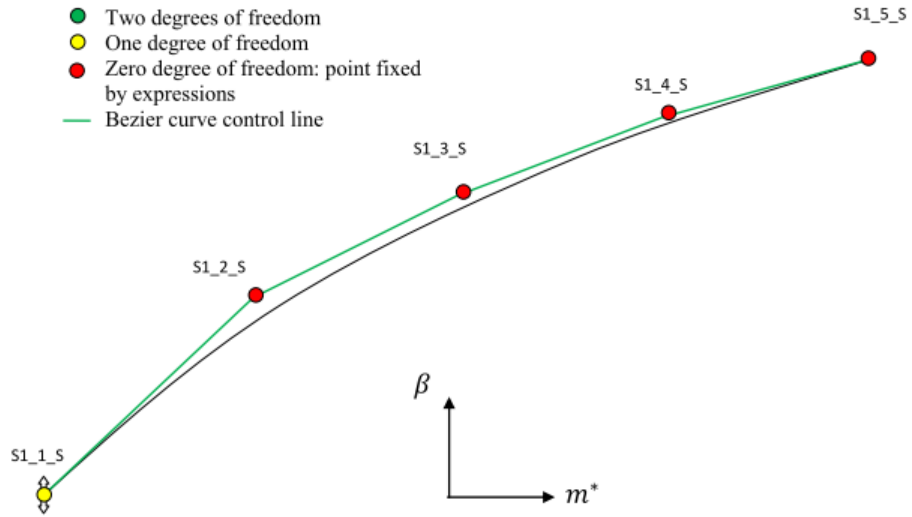


**Figure 41: Diffuser camber parameterization**

For diffuser camber parameterization a Bezier curve, controlled by 5 points equally distributed along the normalized abscissa  $m^*$  has been employed since such atopylogy is sufficient to obtain a rectilinear camber curve in physical plane. Writing the line formula in cylindrical coordinates:

$$\begin{aligned} \vartheta = & a \sin\{[-R_{S1_1_S} \cos(\vartheta_{S1_1_S}) \tan(\vartheta_{S1_1_S} + \beta_{S1_1_S}) + \\ & R_{S1_1_S} \sin(\vartheta_{S1_1_S})] \cdot \cos(\vartheta_{S1_1_S} + \beta_{S1_1_S}) / R\} + \\ & + \vartheta_{S1_1_S} + \beta_{S1_1_S} \end{aligned} \quad (1)$$

and the corresponding  $\beta$  angle expression:

$$\beta = \beta_{S1_1_S} - (\vartheta - \vartheta_{S1_1_S}) \quad (2)$$

it's straightforward to assign the desired value of  $\beta$  to  $S1_2_S, S1_3_S, S1_4_S$  and  $S1_5_S$  (Figure 41).

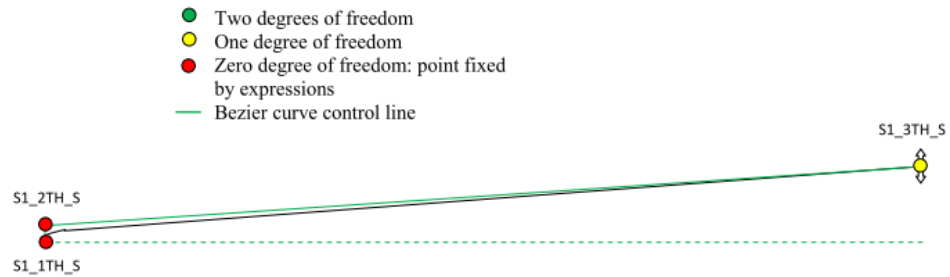


**Figure 42: Diffuser half-thickness parameterization**

The diffuser suction and pressure sides have been defined in the same way of impeller main blade ones. For half-thickness law definition, a Bezier curve with 3 control points has been employed. The first control point is rigidly joined to diffuser LE while the second one can vary in order to adjust the LE radius amplitude. The third one is placed at diffuser TE and controls the maximum thickness of blunt profile (Figure 42). The ratio between fluid passage area at diffuser outlet and the corresponding one at diffuser inlet has been introduced as user defined variable in place of *S1\_3TH\_S* in order to manage more directly the diffusion of stator row.

Also for diffuser row, the number of blades is free to vary. Therefore the diffuser row model presents 6 independent variables, hereafter reduced in number because of geometrical constraints.

## 8.4 Fluid mesh generation and CFD analysis

The whole fluid domain has been meshed by means of Numeca/IGG Autogrid5 [93]. For each row involved the multi-block hexahedral structured mesh is built in four main steps: firstly defining the number of meridional flow paths, then selecting the B2B mesh topology, afterwards optimizing the B2B mesh on a prescribed number of spanwise layers and interpolating them on the axi-symmetric surfaces obtained by meridional flow paths azimuthal revolution, finally generating the 3D mesh. Both for the impeller and diffuser row 57 meridional flow paths and 101 B2B mesh optimization layers have been chosen, moreover in order to obtain a  $y^+$  lower than unity, the cell width at wall has been set equal to  $1.0e^{-06}$  mm, using the empirical formula suggested by Numeca/FineTurbo manual [93]. As regards impeller row the H&I B2B mesh topology, for blade channel, and the butterfly topology, for blade gap (of width 0.2 mm, constant along the rotor blade tip), have been adopted while as concerns diffuser row the O4H B2B mesh topology has been selected. An additional H block has been created upstream the impeller row. The entire mesh is made up

of about 2.0 million of cells, 1.35 million in the impeller row, 0.05 million in the inlet duct and 0.6 million in the diffuser row.

A Python script that automatically manages the multirow configuration has been implemented in order to simplify the interfacing with the optimization environment.

The CFD calculation is arranged throughout Numeca/FineTurbo [93] and is carried out by means of Numeca/Euranus Navier Stokes equations solver ([93][94][95]). A RANS steady approach is followed and the two equations SST (Shear Stress Transport) ([96][97][98]) model has been chosen for representing turbulence phenomenology. Absolute total flow conditions, absolute flow angles, turbulent kinetic energy and turbulent dissipation rate values determined by empirical relations [93] are set at inlet while mass flow rate is imposed at outlet. No slip boundary condition is assumed at solid walls and rotation periodicity condition is adopted to match periodic surfaces. Moreover the interface between impeller and diffuser row is managed by conservative coupling through pitchwise rows mixing plane approach.

## 8.5 Solid mesh generation and structural analysis

### 8.5.1 Automated solid mesh generation procedure

Solid wall boundaries, both for blade and channel are provided by aerodynamic NUMECA CFD calculations in STL (STereoLithography) format while the other surfaces needed for the 3D model creation have been generated through a Python script.

Hence, a procedure that has involved three opensource software has been implemented:

- checking and fixing all STL triangles coming from Python script through ADmesh, a code for processing triangulated solid meshes. Through this opensource software it is possible to correct face orientation or shape error that could occur during the process, obtaining a reliable and robust procedure;
- exporting STL triangles to GMSH, a three-dimensional finite element mesh generator, developed by Christophe Geuzaine and Jean-François Remacle ([99], [100]). Mesh elements are quadratic tetrahedral created through Delaunay algorithm. For stress analysis each mesh has approximately 200.000 nodes and 120.000 elements, while for modal analysis, carried out over a large number of nodal diameters (see [101], [102] and [103]), the number of nodes and elements has been reduced to 40.000 and 25.000 respectively, to speed up calculations. Modal analysis is less sensitive to mesh

sizing than stress analysis, therefore a quite poor mesh sizing can provide very satisfactory results anyway. In fact, the sensitivity analysis carried out provided the average frequency discrepancy between the finer and the coarser model, which is lower than 0.5%;

- exporting 3D mesh to CalculiX, a finite element analysis application, developed by Guido Dhondt and Klaus Wittig [104] , in order to perform thermo-mechanical and modal analyses.

### 8.5.2 Material selection

Titanium TI-6AL-4V has been selected for its high yield stress over mass density ratio; this choice has been made in order to have less structural constraints and enhance aerodynamic performance.

The characteristics used in the calculation are as follows: elasticity modulus= 113 GPa, mass density= 4.43 kg/dm<sup>3</sup> and yield stress = 950 MPa.

The allowable stress used in the optimization procedure has been set equal to 600 MPa.

### 8.5.3 Thermomechanical analysis

Thermomechanical analysis has been performed applying three types of loadings:

- constant temperature of 210 °C. This assumption has been made since thermal distribution in compressor impeller is not as important as, for example, in radial turbine;
- static pressure distribution calculated by the flow solver, interpolating from CFD to FEA mesh through a Fortran script;
- centrifugal force, by setting a rotational speed of 75.000 RPM.

Appropriate constraints on displacements have been applied in the FEA model.

Material model is linear elastic and geometrically nonlinear effects have been taken into account. In the periodic surfaces of the impeller, adequate boundary conditions have been applied, such that only a  $1/N_{rotor}$  part of the geometry can be simulated.

After being run the calculation, Von Mises stress field of the blade is evaluated. For the stress assessment Von Mises stresses in the blade are compared to an allowable stress of 600 MPa and a penalty factor has been defined as follows:

$$P_{stress} = \begin{cases} W_{stress} \left(1 - \frac{\sigma_{max}}{\sigma_{all}}\right)^2 & \text{if } \sigma_{max} > \sigma_{all} \\ 0 & \text{if } \sigma_{max} \leq \sigma_{all} \end{cases} \quad (3)$$

#### 8.5.4 Modal analysis

Next step has been to analyze blade eigenfrequencies, in order to guarantee a safe behavior in the operating regime. Also for modal analysis periodic boundary conditions have been applied, such that only a  $1/N_{rotor}$  part of the geometry can be simulated.

Resonances have been avoided in a range between 105% and 95% of the nominal speed. Resonances occur when the two following conditions are met:

1. the frequency of the exciting force equals the eigenfrequency;
2. the exciting force profile has the same shape as the associated mode shape of vibration.

Normally, to identify resonance condition two types of diagram can be used, the Campbell and the SAFE diagrams. Campbell diagram can predict if blades eigenfrequencies coincide with the exciting frequencies, identifying a condition of possible resonance. In the Campbell diagram only the first condition above described can be represented.

SAFE (Singh's Advanced Frequency Evaluation) diagram, also called interference diagram, that has been used in this work, differs from the Campbell diagram because it plots frequency as a function of nodal diameters (mode shape) rather than frequency as a function of speed. Through the SAFE diagram the probable resonances can be identified, because it can represent both the conditions above described.

Depending on number of blades, there are different numbers of nodal diameters. Through a script which modifies CalculiX input deck, the correct number of nodal diameters, necessary for calculation and assessment, is specified; then eigenfrequencies are extracted and an assessment is performed.

Fluctuating forces considered are due to two primary sources:

- nozzle passing frequency excitation, caused by nozzle vanetrailing edge wakes as the flow leaves the vanes;
- running speed harmonic excitation. In this work the first four engine orders EO have been considered.

Through a Fortran script, probable resonances, depending also on number of blades and vanes (which are not constant values but variable parameters), are checked.

In this particular case, vane excitation is of higher harmonics than  $N_{rotor}/2$ ; it can be shown that the engine orders, that can excite a tuned disk mode, satisfy the following equation:

$$L = |nN_{rotor} \pm M| \quad (4)$$

where n is an integer.

The penalty factors have been defined as follows:

$$P_{freq\_low} = \begin{cases} W_{freq\_low} \left( \left| \frac{f_{eigfr}}{f_{exc\_low}} - 1 \right| - 0.05 \right)^2 & \text{if } \left| \frac{f_{eigfr}}{f_{exc\_low}} - 1 \right| < 0.05 \\ 0 & \text{if } \left| \frac{f_{eigfr}}{f_{exc\_low}} - 1 \right| \geq 0.05 \end{cases} \quad (5)$$

$$P_{freq\_high} = \begin{cases} W_{freq\_high} \left( \left| \frac{f_{eigfr}}{f_{exc\_high}} - 1 \right| - 0.05 \right)^2 & \text{if } \left| \frac{f_{eigfr}}{f_{exc\_high}} - 1 \right| < 0.05 \\ 0 & \text{if } \left| \frac{f_{eigfr}}{f_{exc\_high}} - 1 \right| \geq 0.05 \end{cases} \quad (6)$$

Thus, the structural analysis objective function can be obtained as the sum of the previously described terms:

$$P_{mech} = P_{stress} + P_{freq\_low} + P_{freq\_high} \quad (7)$$

## 8.6 Optimization algorithm

The optimization algorithm is the one implemented in Numeca/FineDesign3D. The detailed description of the method and the early applications of the algorithm on two-dimensional airfoils are reported in [105]. Afterward the procedure has been employed also for 3D axial and centrifugal turbomachinery blades aerodynamic optimizations [64][65][66][67][68][69].

In the present work a multidisciplinary optimization is carried out, interfacing CalculiX mechanical computation with Numeca/FineDesign3D optimization process through in-house developed Python scripts.

### 8.6.1 Optimization strategy

The optimization strategy is based on meta-models: the objective function modeled through an artificial neural network (ANN) is minimized using a genetic algorithm. At the first step the ANN is trained using a database of 3D CFD solutions created with a DoE technique. The set up

of the ANN is automatically performed by providing the code with the DoE samples and the number of layers in the ANN. The ANN is then internally designed and trained by the Design3D module. The successive step is to run the optimization with the genetic algorithm and using the ANN as meta-model; the intermediate optimum obtained is then validated with a 3D CFD solution and used to update the ANN model. The overall process is repeated for a given number of iterations. The idea is to start with a rough meta-model from a coarse database and refine it during the process. The optimization technique is a single objective approach and employs an objective function assembled through the sum of several penalty terms as defined in the following.

#### 8.6.1.1 Database generation

For the centrifugal compressor database generation, due to the high number of variables involved in the optimization process, a fractional factorial sampling has been chosen. In fact, other more refined DoE techniques would lead to too expensive computational effort. Giving to each parameter the possibility to assume nine different values between its lower and upper bound 700 CFD calculations, chosen randomly among the available ones, have been performed as database samples.

#### 8.6.1.2 Objective functions

The optimization procedure is applied in order to minimize a single objective function that is composed by the sum of several dimensionless penalty terms (equation (8)), each of which contains a structural or aerodynamic quantity.

$$P = P_{\eta_{is\,tt}} + P_{\beta_{tt}} + P_{stress} + P_{freq\_low} + P_{freq\_high} \quad (8)$$

Due to the parabolic form of each penalty term the objective function is a convex function, therefore a minimum always exists. Each parabolic penalty term has a weighting coefficient. In the centrifugal compressor optimization five penalty terms are employed, two aerodynamic (Equation(9), (10)) and three structural (Equation (3), (5) and (6)).

$$P_{\eta_{is\,tt}} = \begin{cases} W_{\eta_{is\,tt}}(1 - \eta_{is\,tt})^2 & \text{if } \eta_{is\,tt} < 1 \\ 0 & \text{if } \eta_{is\,tt} \geq 1 \end{cases} \quad (9)$$

$$P_{\beta_{tt}} = \begin{cases} W_{\beta_{tt}} \left(1 - \frac{\beta_{tt}}{4.5}\right)^2 & \text{if } \beta_{tt} < 4.5 \\ 0 & \text{if } \beta_{tt} \geq 4.5 \end{cases} \quad (10)$$

The structural penalty terms have been previously discussed. The aerodynamic ones are composed in order to maximize the total-to-total isentropic efficiency and guarantee the

design absolute total pressure ratio. The values of the weighting coefficients used are summarized in Tab. 18.

**Tab. 18: Mechanical weighting coefficients.**

	<b>Value</b>
$W_{stress}$	20
$W_{freq\_high}$	20
$W_{freq\_low}$	20
$W_{\eta_{isst}}$	50
$W_{\beta_{tt}}$	25

Aerodynamic and structural optimizations act simultaneously in the proposed optimization procedure, thus extracting the better solution in accordance with the definition of the overall objective function defined in Equation(8).

## 8.7 Results

The DOE procedure previously described led to a database that covers well the input variable domain. Penalty functions for aerodynamic and mechanical features are evaluated for each sample and the surrogate model, trained on this dataset, drove the optimization algorithm through different geometries reducing the global penalty function.

A representation of these data sets, in terms of aerodynamic and mechanical penalty functions, is depicted in Fig. 43. This diagram shows that preliminary geometry performs better than many database samples. Nevertheless it is worth noting that a lot of database samples have lower penalty values than preliminary geometry concerning mechanical behavior.

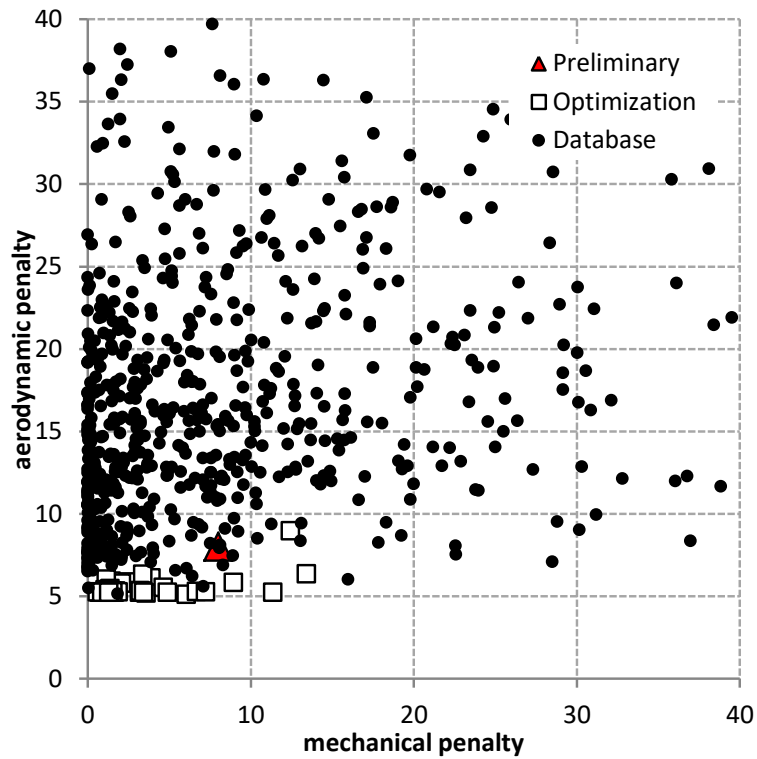


Fig. 43: Aerodynamic and mechanical penalty for the preliminary configuration, database samples and optimization.

The optimization process, starting from the most performing database sample, finds several geometries with improved aerodynamic performance even though there is a great deviation in terms of local stress and vibrations (mechanical penalty). The characteristics of the most performing sample, named in the following as the optimized geometry, are reported in Tab. 19. The global performance parameters are compared with those of the preliminary design in Tab. 20.

Tab. 19: Compressor optimized design geometrical parameters.

$R_{1i}/R_{1o}$	0.27	$\beta_{1i}$	$35^\circ$
$R_{1o}/R_2$	0.62	$\alpha_2$	$68^\circ$
$b_2/R_2$	0.08	$\beta_{b2}$	$34^\circ$
$\Delta x/R_2$	0.50	$\alpha_{b4}$	$37^\circ$
$\delta_b/b_2$	0.05	$Z_R$	10 + 10
$\alpha_{1o}$	$0^\circ$	$Z_V$	19

$\beta_{1o}$	$63^\circ$	$R_3/R_4$	0.65
--------------	------------	-----------	------

Isoentropic efficiency gains nearly 4 points during the optimization process and, considering also the slight increase of pressure ratio, improvement obtained in terms of polytropic efficiency is even better. The peripheral velocity at the impeller outlet  $u_2$  increases due to the larger impeller outlet diameter, leading to a stronger component of centrifugal forces acting on the impeller. This is related to the increased backsweep angle  $\beta_{b2}$  that reduces the tangential velocity component of the flow at the impeller outlet section and consequently the work exchange.

**Tab. 20: Comparison of compressor optimized and preliminary design global performance parameters.**

	Preliminary	Optimized
$\eta_{is\ tt}$	0.80	0.84
$\beta_{tt}$	4.4	4.6
Maximum $Ma_{r1}$	1.4	1.25
Maximum $Ma_2$	1.3	1.15

The geometric parameters, which the optimization procedure has modified, have a direct impact on the flow field within the impeller and the diffuser. In particular, a comparison of Tab. 19 with Table 17 highlights a reduction of the ratio  $R_{i1}/R_{10}$ . This has a direct consequence on the absolute Mach number at the impeller inlet section, which is reduced in the optimized configuration, as depicted in Fig. 44. The strong shock wave structure that is present in the preliminary geometry analysis, due to the transonic flow, is completely absent in the optimized design with a positive impact on impeller efficiency. The reduction of the blockage related to the smaller blade number is another component of this effect. This feature moreover, combined with a reduced axial length of the impeller  $\Delta x/R_2$ , contributes to the reduction of the wet surfaces and of the tip gap area. These features have a positive impact on the aerodynamic efficiency even though the blade loading increases, due to the reduced number of blades, as depicted in Fig. 45, with a greater pressure difference between pressure and suction side.

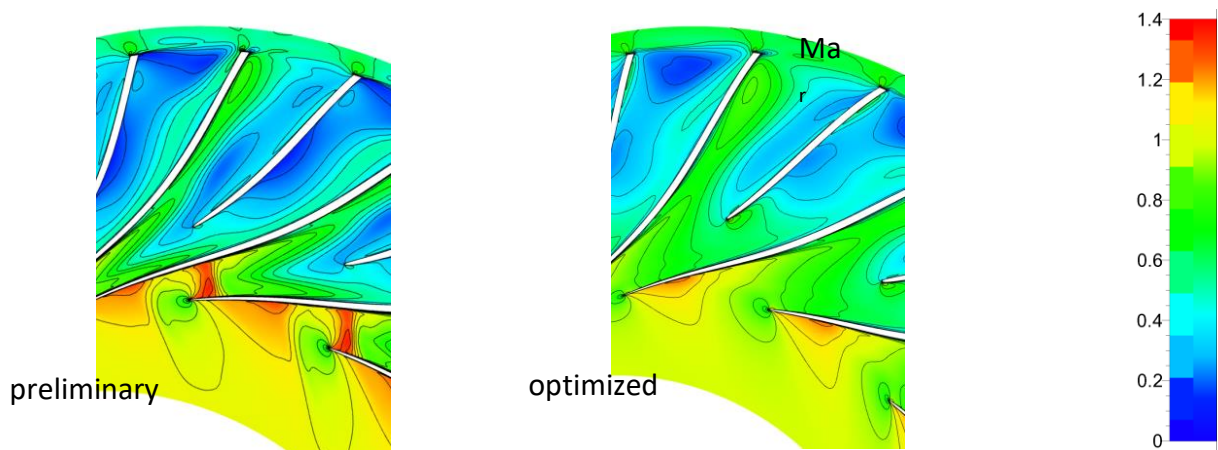


Fig. 44: Comparison of relative Mach number at 0.9 span section, impeller inlet section.

Fig. 45 shows also the improvement of flow incidence at LE of both main blade and splitter. The blade loading has a smoother distribution over the entire blade length.

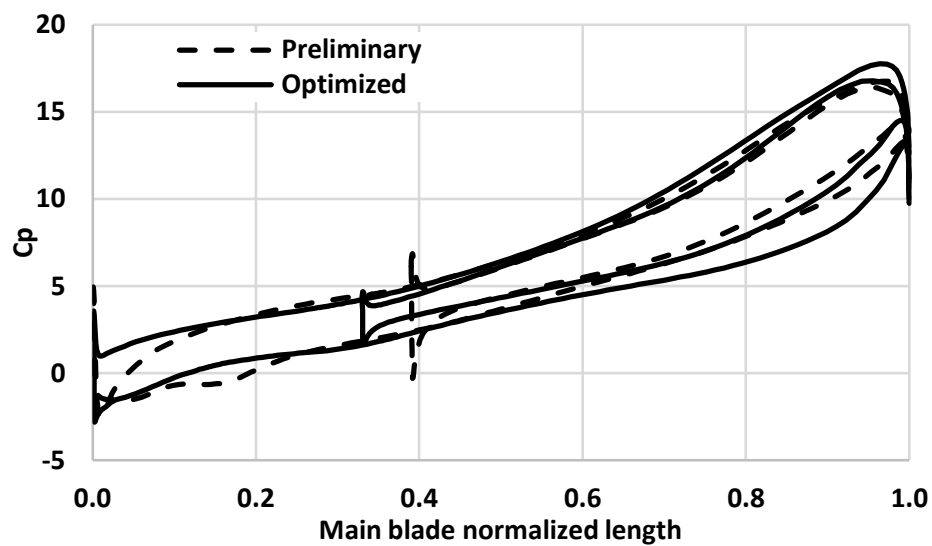


Fig. 45: Comparison of blade loading at midspan.

Fig. 46 collects relative Mach number distributions over three control sections A, B, and C respectively: at the impeller inlet, at splitter blade inlet and at the impeller outlet, respectively (as shown in Fig. 46a).

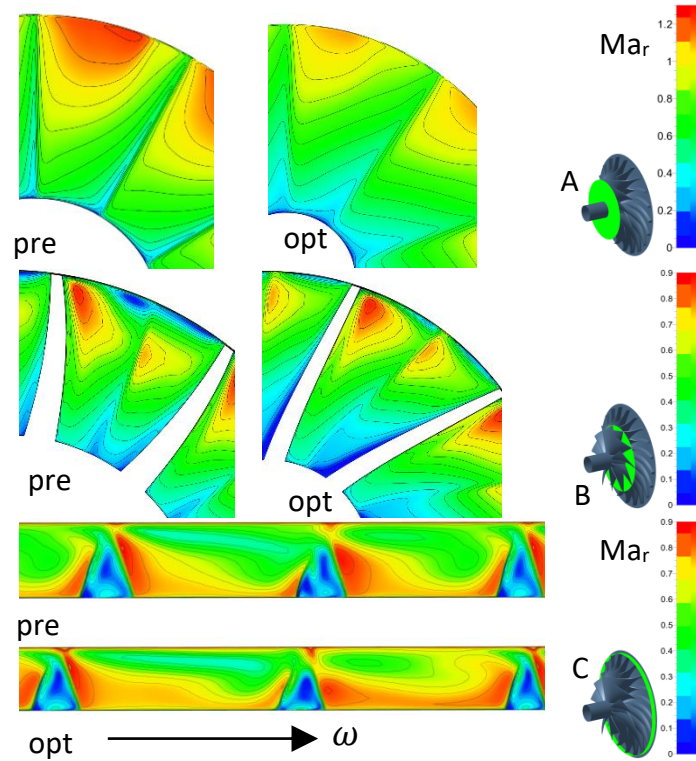


Fig. 46: Comparison of relative Mach number in three control sections (A, B, C).

The relative flow at the impeller inlet section A, as previously stated, is characterized by a lower value of  $Ma_r$  especially at blade tip section with beneficial effects on both global efficiency reducing local energy losses due to the shock waves, and off design operating range as reported in Fig. 47.

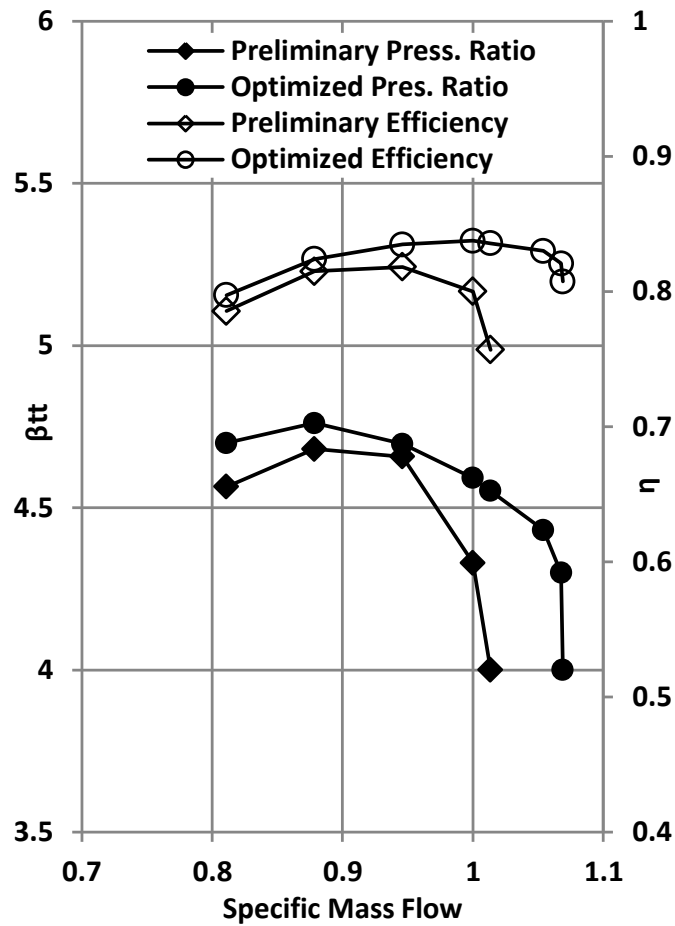


Fig. 47: Performance maps of both Preliminary and optimized geometry.

Indeed, even though the optimization procedure is focused only on the nominal operating condition, it shows that the optimized compressor is characterized by larger efficiency and pressure ratio over the entire operating range, as well as by a smaller sensitivity to the specific mass flow variation.

Fig. 46b depicts the same Mach field for both the configurations even though it highlights a different lean angle distribution for the splitter blades leading edge [106].

In Fig. 46c,  $Ma_r$  distribution for optimized geometry is comparable with the preliminary one both in terms of distribution and maximum value.

It is worth noting that even though the outlet section diameter increased, the outlet area decreased due to the reduction of the blade height  $b_2$ . This has a beneficial effect on the flow in the vaneless diffuser zone reducing the possibility of reverse flow [106].

Absolute Mach distribution within the diffuser is reported in Fig. 48. Its average value at diffuser inlet has not been strongly affected by the optimization process even though the different blade shape enables a smoother velocity reduction and consequently a more efficient pressure recovery.

In order to assess the validity of the results obtained with the assumption of steady flow used during the database generation and optimization process, an unsteady calculation has been also carried out on the optimized configuration. A phase lagged boundary condition has been used to handle the diffuser periodicity in order to avoid the computation of a full annulus grid.

Unsteady global results, such as pressure ratio and efficiency, are in good agreement with the steady performance resulting in a difference value of 0.5%, thus proving the reliability of the mixing plane approach.

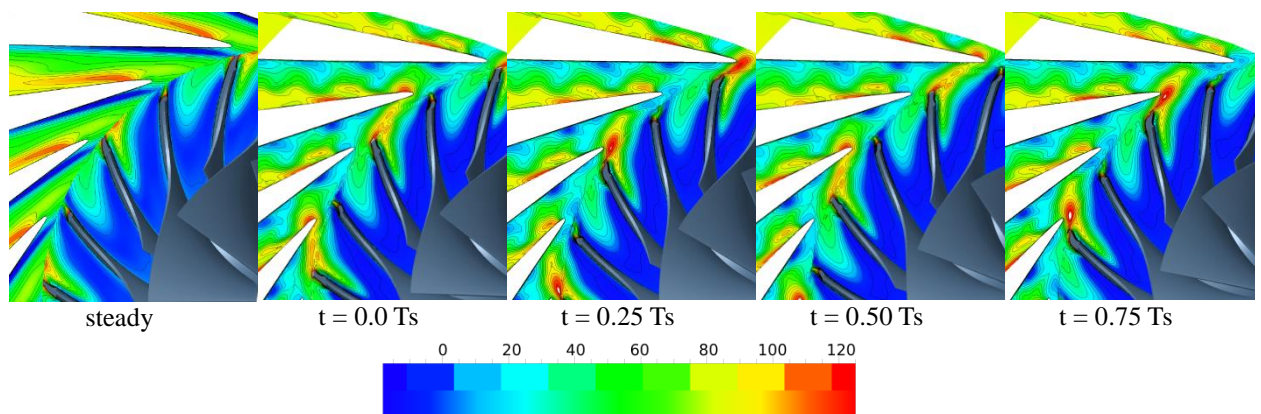


Fig. 49 shows a comparison of entropy generation for steady and unsteady simulations at the rotor/stator interface. The high level of entropy within rotating blades wakes affects also the diffuser vanes with a persistent unsteadiness as clearly visible throughout the instantaneous entropy contours at midspan reported in Fig. 49.

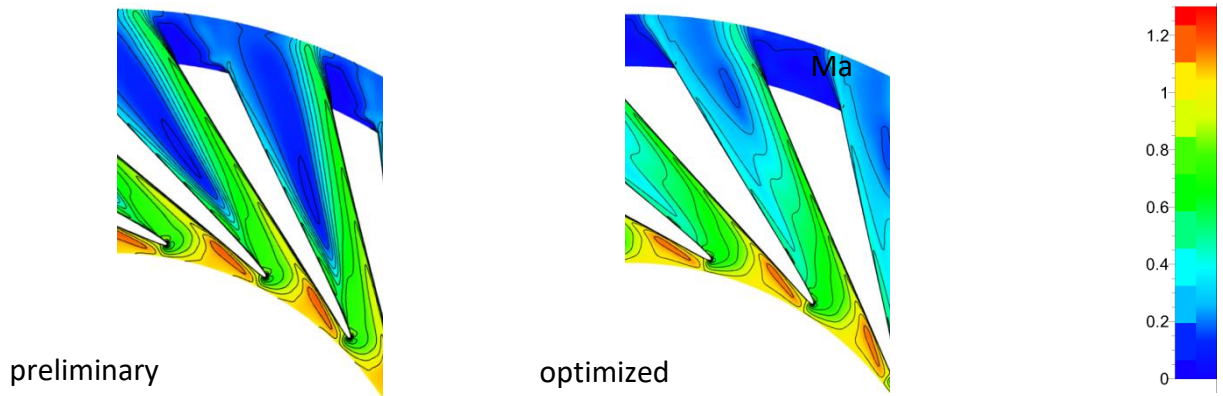


Fig. 48: Comparison of Mach number at 0.5 span section, vaned diffuser.

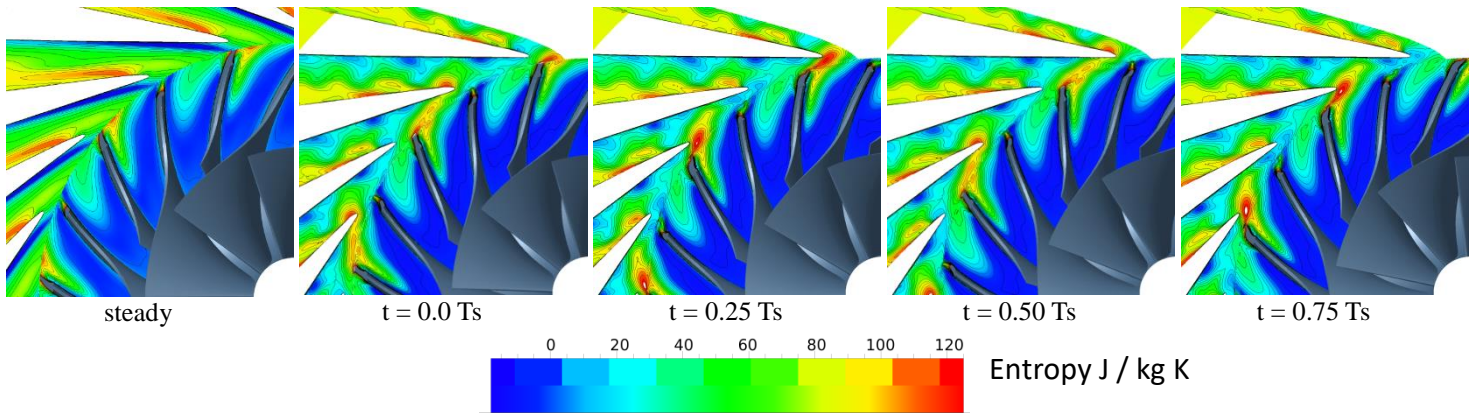


Fig. 49: Entropy contours at 0.5 span section for unsteady simulation, four contiguous time steps, optimized geometry.

Concerning the structural optimization, Fig. 50 shows the Von Mises stress field for preliminary and optimized configurations: the two configurations show similar maximum Von Mises stress, but in the optimized configuration the Von Mises stress map is smoother and the stress at the hub has been reduced. In figure the stress scale has been limited to 600 MPa for both the samples.

The maximum Von Mises stress does not represent a limiting factor in the optimization procedure, since the use of titanium and a reasoned parameters choice, which led to not excessive lean angles and blade heights, enabled to limit the overall stress distribution in the impeller.

Moreover, the peak stress is concentrated in the fillet zone, as it is clearly visible in Fig. 50, in both the configurations, where some geometry simplifications have been introduced. A

complete and detailed modeling of the fillet zone will definitely reduce these stress values, which, furthermore, are concentrated in a zone where local plastic strain can be potentially accepted after a dedicated analysis for low cycle fatigue assessment.

In the optimized impeller the stress level in the airfoil is quite low and well balanced.

Local high stresses near the rotation axis are mainly due to the constraints of the model, therefore they can be neglected. A more detailed analysis of this part could be done via axisymmetric 2D analysis but it is not object of the present work.

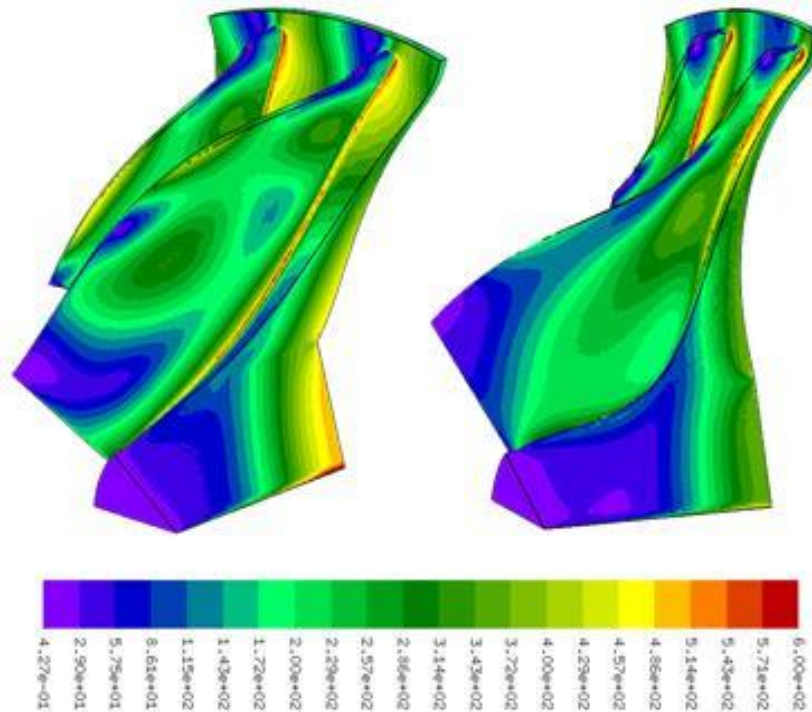


**Fig. 50: Von Mises stress distribution in the preliminary (left) and optimized (right) configuration [MPa].**

For the dynamic behavior assessment, unlike the stress one, it is difficult to make some considerations on the eigenfrequencies a priori. It is clear that, since the number of blades and vanes are free parameters, the dynamic behavior of the system is subject to many variables, thus complicating the optimization process.

Therefore, an automated procedure is needed to check the blade behavior and meet all the dynamic requirements defined in the set up phase.

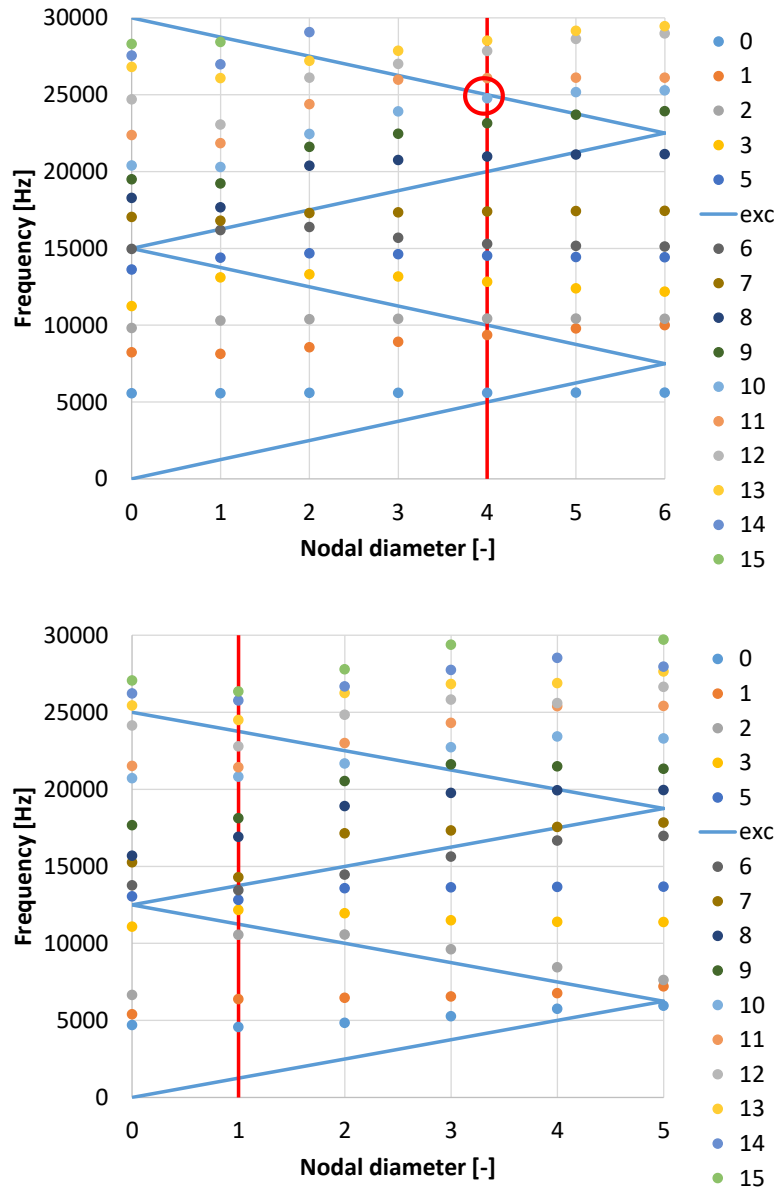


**Fig. 51: SAFE diagram in the preliminary (top) and optimized (bottom) configuration.**

Fig. 51 shows the SAFE diagram for the preliminary and the optimized impeller.

In the preliminary configuration there are no resonances with the first four EO, while there is a resonance due to number of downstream vanes. The resonance occurs at 4 nodal diameter according to the equation (2), where  $L = 20$  (number of vanes),  $n = 2$  and  $M = 4$  and it is represented with the red circle depicted in the top figure.

In the optimized configuration there are no resonances; the modifications of the impeller are mainly related to the upper part of the leading edge of the main blade, in correspondence to the inlet. The optimization procedure, slightly modifying the thickness distribution, changed the eigenfrequencies, obtaining a blade free from resonance in the range 95%-105% of the operating speed. In particular resonance could occur at 1 nodal diameter according to the

equation (2), where  $L = 19$  (number of vanes),  $n = 2$  and  $M = 1$ , but the resultant safety margin is 6%, in accordance with the limits set in the assessment phase.

## 9 Global optimization results

---

The overall results for the centrifugal compressor and the radial turbine obtained have been reported in this chapter. As reported above, also recuperator has a great influence on overall efficiency but, in this work, only considerations on the preliminary design have been reported.

Through the integrated design approach proposed, starting from a preliminary 1D design, for radial turbine the goals reported in Table 21 have been achieved.

**Table 21: turbine optimization summary results**

	Preliminary	Optimized
Mass flow [kg/s]	0.85	0.76
Total to total efficiency [-]	0.87	0.927
Power [kW]	250	246
U/C0	0.655	0.651
Stress usage factor [-]	2.34	0.98
Resonance 4EO	Yes	No
Resonance NPF	Yes	No

Multidisciplinary optimization enabled to achieve the following goals:

- high efficiency (92.7%); no separated flow regions;
- Von Mises stress field below the allowable limits, defined as a function of temperature;
- free from resonance behaviour of the impeller, in the speed operating regime, for the sources of excitation considered.

For the centrifugal compressor the goals reported in Table 22 have been achieved.

**Table 22: compressor optimization summary results**

	Preliminary	Optimized
Mass flow [kg/s]	0.74	0.74
Total to total efficiency [-]	0.80	0.84
Compression ratio [-]	4.4	4.6
Inlet relative Mach at impeller tip [-]	1.4	1.25
Absolute Mach at diffuser inlet [-]	1.3	1.15
Stress usage factor [-]	1.54	0.95
Resonance 4EO	Yes	No
Resonance NPF	Yes	No

Multidisciplinary optimization enabled to achieve the following characteristics:

- higher efficiency (84%);
- high  $\beta_{(t-t)}$  in centrifugal single stage;
- transonic rotor and subsonic stator;
- reduction of the separated flow zone;
- Von Mises stress field below the allowable limits;
- free from resonance behaviour of the impeller, in the speed operating regime, for the sources of excitation considered.

## 10 Conclusions

---

In the first part of the work an overall analysis of the thermodynamic cycle and the main influencing parameters have been reported. It is clearly shown that a strong efficiency optimization of the different components can lead to an overall efficiency up to 36%, keeping the turbine inlet temperature at 950 °C and thus avoiding the use of ceramic materials for the turbine impeller. The preliminary design procedure has been reported for the combustor, the recuperator and the bearings, giving an insight of the integrated multidisciplinary design of the micro-gas turbine.

Three main considerations can be remarked:

- turbine cooling techniques, for the current application, doesn't provide significant advantages for efficiency enhancement;
- the same efficiency increase for compressor and turbine leads to really different effects on overall efficiency, therefore it is convenient to address the design efforts on the turbine;
- the recuperator effectiveness plays a key role for the cycle efficiency, but its design has to fulfil geometrical (overall dimensions) and thermodynamic (pressure losses) constraints.

Then, three main components of the micro-gas turbines, i.e. combustion chamber, recuperator and bearings, have been described and some preliminary design considerations have been reported. Moreover for the bearings a new innovative layout has been presented, useful for extending and optimizing the bearings life.

In the last part of the work the multidisciplinary optimization procedure, partially based on opensource software, has been described and discussed, both for centrifugal compressor and radial turbine.

For this latter, the aim of the work was to illustrate a multidisciplinary procedure capable of increasing aerodynamic efficiency and improving mechanical safety for high speed radial gas turbines. The work illustrates the coupling between a widely used CFD commercial software and open source tools for mesh generation and mechanical analysis. The coupling has been obtained via in-house developed Python and Fortran scripts suited for the current application.

Regarding the centrifugal compressor, the multidisciplinary optimization has started from a preliminary design based on 1-D equations, empirical data and statistical analysis, which allow the selection of the ranges of variation for the main parameters, a multi-disciplinary optimization based on surrogated models has been performed to reach an optimized configuration with higher performance. A commercial CFD tool and an open source FEA software have been coupled through in house developed scripting modules, which manage multidisciplinary optimization, mesh generation, geometry parameterization and results post-processing.

The optimization procedure has been able to identify the most influencing geometrical parameters related to losses mechanisms and to drive the design process towards global thermodynamic performance enhancement while guaranteeing a safe component operation. Furthermore, an unsteady simulation has been carried out in order to check the overall results of the optimized geometry, deepening the effects of rotor-stator interaction on the compressor global performance.

The off-design behavior has been also investigated resulting in a wider operating range, increasing choking mass flow, and in a larger efficiency over the whole characteristic curve.

## 11 Appendix: modal analysis of bladed wheels

Compressor and turbine bladed wheels interact with the fluid distributed by the stator vanes. The blades are excited by fluctuating forces, and their vibration is the reason of fatigue failures. The Campbell diagram approach is just to avoid the matching between the natural mode frequency and the excitation frequency. However, bladed wheels show many natural frequencies that are very near each other, so it is difficult to avoid any resonance matching. The SAFE diagram approach introduces also the shape matching instead of just the frequency matching. Many frequency matching can be identified as non-critical and then tolerated.

### 11.1 Theory

Turbine wheels and compressors vibrate due to the interaction of the fluid between the impeller and the stator. Blade excitation can produce an intense fatigue stress that can lead to fractures typically at the blade attachment to the disk or blade itself. Determining the own frequencies of the wheel is therefore the first step in verifying the improper operation of the impeller. The most immediate approach is that of the Campbell diagram, in which it is possible to identify the eigenfrequencies and compare themselves with the harmonic components of the forcing. Fluid interaction with the impeller blades is of a harmonic nature since the fluid is distributed by a stator, whose compartments are angularly equidistant, and thus interaction cyclically repeats the passage of each sector. The main frequency of this stress is related to the speed of rotation of the impeller and the number of stator blades which coincides with the number of compartments. The additional harmonics of the forcing are multiple of the main frequency and therefore also linear with the rotation speed of the impeller. The frequencies of the rotated wheel are, basically, not influenced by the rotation speed (neglecting the possible effects of stress stiffening and/or centrifugal actions). The Campbell diagram of the palletized wheels is typically as shown in Figure 52.

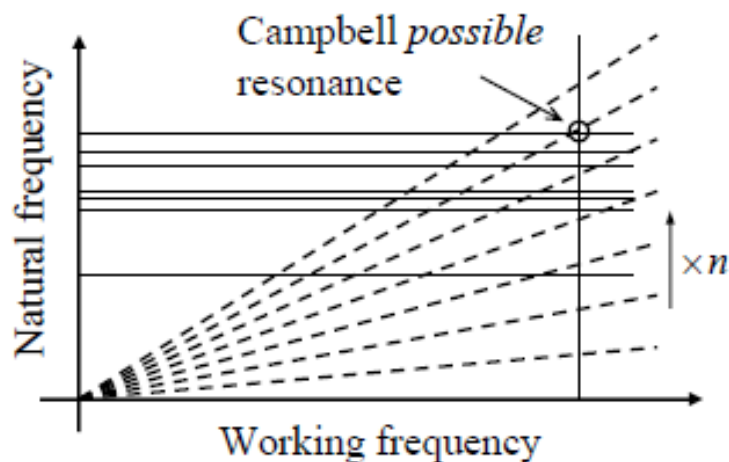


Figure 52: Campbell diagram

The complex shape of bladed wheels has the effect that their frequencies are very close, as shown schematically in Fig.1. Consequently, at each rotation regime there is probably a coincidence (or near values) between a frequency of a multiple multiplex of the main and a natural frequency. Applying the Campbell approach would thus make design impossible, always identifying possible resonances. However, in many situations, both for bladed wheels and for structural dynamics in general, the coincidence between the frequency and frequency of the forcing does not necessarily imply a resonant condition. The structures, having a geometric extension, may have forces in counter-phase (even partial) with the forcing, see Figure 53.

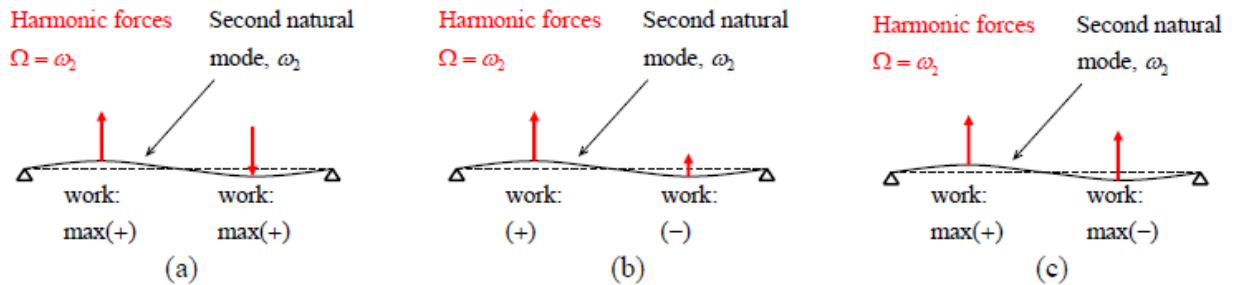


Figure 53: Possible combinations of forcible and proper way, example of beam restraint: (a) constructive composition, (b) partially constructive composition, (c) destructive composition.

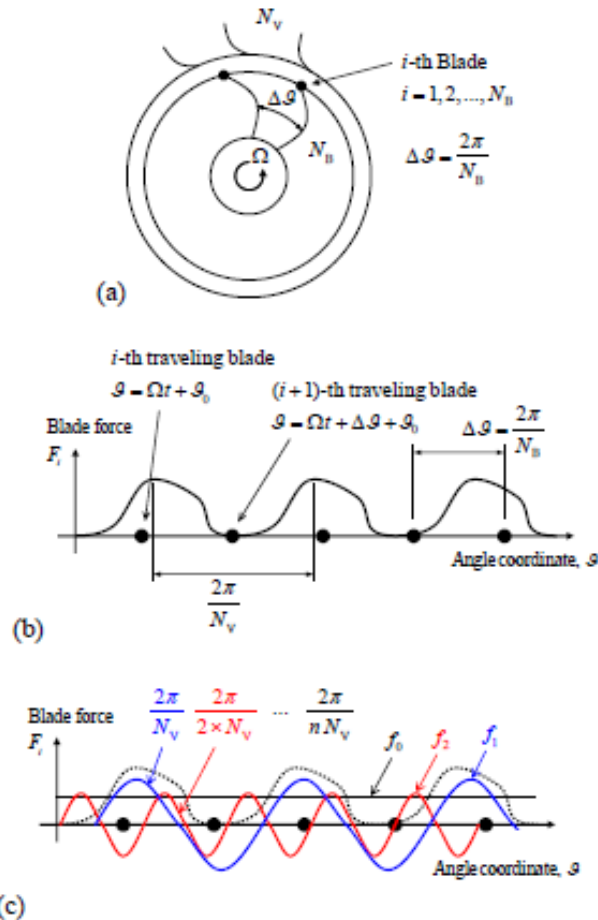


Figure 54: (a) Bladed wheel and stator. (b) Interaction between the time variable and the angular position of each blade. (c) Force breakdown on single blade in multiple harmonics of the fundamental harmonic.

The Singh's Advanced Frequency Evaluation (SAFE) diagram, which was introduced by M.P. Singh was later considered to be the point of reference for the check of bladed wheels, can precisely identify those combinations between the eigenfrequencies and the harmonic of excitation, considering the coincidence of the frequencies as well as the combination of the shape.

This diagram applies to a family of bladed wheels with modular geometry, thus providing an optimal configuration that avoids dangerous resonances.

Figure 54 (a) shows the main dimensions needed to describe the vibratory dynamics of bladed wheels.  $\Omega$  is the angular velocity of the impeller,  $\Delta\theta$  is the angular distance between a blade and the next, while  $N_B$  and  $N_V$  are the number of blades of the impeller and the number of vanes, respectively.

Each blade receives an interaction action with the stator by means of fluid flow. This force is of a harmonic type for the cyclic symmetric stator with which the single blade interacts. In addition, the forces on the various blades are equal to each other, but with an angular displacement. Since each blade interacts with the stator compartments, the frequency of the fundamental harmonic is:

$$\Omega_1 = N_V \Omega$$

The next harmonics are simply multiple of the first:

$$\Omega_n = n\Omega_1 = nN_V\Omega$$

The overall force acting on each of the two shovels can therefore be decomposed according to the Fourier series, Eq3, to note the interaction between time and angular position as shown in Figure 54 (b).

$$f_i = F_0 + \sum_{n=1}^{\infty} F_n \cos(nN_V(\Omega t + i\Delta\vartheta) + \varphi_n)$$

$F_1, F_2 \dots F_n$  are the different harmonics. Their overlapping create the total force  $f_i$  for each blade  $i$ , Figure 54 (c).

The generic blade responds to vibrational stress with a oscillating deformation motion that can be expressed by modal overlap:

$$x_i = X_0 + \sum_{m=1}^{\infty} X_m \cos(\omega_m t + \varphi_{tm}) \cos(d_m \Delta\vartheta i + \varphi_{\vartheta m})$$

where  $X_m$  is the amplitude of the single  $m$ -mode,  $\omega_m$  is the (angular) frequency of the generic mode itself, and finally  $d_m$  is the number of nodal diameters of the single mode itself. The number of nodal diameters is, of course, a specific concept in this discussion regarding bladed wheels. The nodal diameters are points along the circumference of the wheel that do not undergo displacement, relative to a single particular mode.

$d_m$  can be any natural up to a maximum value of  $d_{m,\max} = N_B/2$  if  $N_B$  is even, equal to  $d_{m,\max} = (N_B-1)/2$  if it is odd.

## 12 References

---

- [1] Mueller, L., Alsalihi, Z., Verstraete, T., 2013, "Multidisciplinary Optimization of a Turbocharger Radial Turbine", *Journal of Turbomachinery*, Volume 135
- [2] Verstraete, T., Alsalihi, Z., Van den Braembussche R., 2010, "Multidisciplinary Optimization of a Radial Compressor for Microgas Turbine Applications", *Journal of Turbomachinery*, Volume 132  
World Energy Outlook 2015; ODEC/IEA 2015; Agenzia Internazionale per L'energia
- [3] GTcycle, <https://github.com/ampsolutions/gtcycle>
- [4] Lefebvre, A.H., and Ballal, D.R. – "Gas Turbine Combustion – Alternative Fuels and Emissions", 3th edition, CRC Press, 2010.
- [5] Shah R. K., 2005, Compact heat exchangers for microturbines, 5th International Conference on Enhanced, Compact and Ultra-Compact Heat Exchangers, Science Engineering and Technology.
- [6] McDonald C. F., 2003, Recuperator considerations for future higher efficiency microturbines, *Applied Thermal Engineering*, 23(12), 1463-1487.
- [7] Utriainen E. and Sundén, B., 2002, Evaluation of the cross corrugated and some other candidate heat transfer surfaces for microturbine recuperators, *Journal of Engineering for Gas Turbines and Power*, 124(3), 550-560.
- [8] Maziasz P. J., Pint B. A., Swindeman R. W., More K. L. and Lara-Curzio E. 2002, Advanced alloys for high temperature recuperators, *DER Peer Review*, 2.
- [9] Utriainen, E. and Sundén, B., 2002, A numerical investigation of primary surface rounded cross wavy ducts, *Heat and Mass transfer*, 38(7-8), 537-542.
- [10] Isomura K., Togo, S.-I., Tanaka S. Study of Micro-High Speed Bearings and Rotor Dynamics for Micromachine Gas Turbines, Paper 7. In: *Micro Gas Turbines. Educational Notes RTO-EN-AVT-131*, Neuilly-sur-Seine, France 2005.
- [11] Signer H., Bamberger E.N., Zaretsky E.V., Parametric Study of the Lubrication of Thrust Loaded 120-mm Bore Ball Bearings to 3 Million DN. *J. of Lubrication Tech.* 1974; 96 pagg. 515–526.
- [12] Zwysig C., Member S., Kolar J.W., Member S., Round S.D. Megaspeed Drive Systems: Pushing Beyond 1 Million r/min. *Ieee/Asme Trans Mechatronics 2009 Volume 145* pagg. 64–574.
- [13] Akamatsu Y., Mori M.. Development of Eco - friendly Oil Jet Lubricated. *NTN Technical Review.* 2004;72:6-10.
- [14] Popp M., Sternagel R.. Hybrid ceramic and all ceramic anti friction bearings. *Eur Sp Agency-Publications-ESA SP.* 1999;438:105-110.
- [15] Khonsari M.M., Booser E.R.. An Engineering Guide for Bearing Selection. *Tribol. Lubr. Technol.* 2004;February 2004:26-32.
- [16] Finley W.R., Hodowanec M.M.. Sleeve versus antifricition bearings: Selection of the optimal bearing for induction motors. *IEEE Trans Ind Appl.* 2002;38:909-920.
- [17] Waumans T., Peirs J., Al-Bender F., Reynaerts D.. Design, Optimization and Testing of a High-Speed Aerodynamic Journal Bearing With a Flexible , Damped Support. In: *Tech Dig PowerMEMS 2009; December 1-4, 2009; Washington, DC, USA.* 2009. p. 83-86.

- [18] Waumans T., Peirs J., Al-Bender F., Reynaerts D.. Aerodynamic journal bearing with a flexible, damped support operating at 7.2 million DN. *Micromechanics Microengineering*. 2011;21(104014)
- [19] Hikichi K., Isomura K., Saji N., Esashi M., Tanaka S.. Ultra-High-Speed Tape-Type Radial Foil Bearing for Micro Turbomachinery. In: *Proc. PowerMEMS 2009* ; December 1-4, 2009; Washington DC, USA. 2009.
- [20] Schiffmann J.. Enhanced Groove Geometry for Herringbone Grooved Journal Bearings. *J. Eng. Gas Turbines Power*. 2013;135(102501)
- [21] Stanev P.T., Wardle F., Corbett J.. Investigation of grooved hybrid air bearing performance. *Proc. Inst. Mech. Eng. Part K J. Multi-body Dyn.*. 2004;218:95-106.
- [22] Peirs J., Waumans T., Vleugels P., Al-Bender F., Stevens T., Verstraete T., Micropower generation with microgas turbines: A challenge.. *Proc. Inst. Mech. Eng. Part C. J. Mech. Eng. Sci.*. 2007;221:489-500.
- [23] Waumans T., Peirs J., Reynaerts D., Al-Bender F.. On the dynamic stability of high-speed gas bearings: stability study and experimental validation. *Sustainable Constr. Des.*. 2011;2:1-10.
- [24] Görne J.. Using Active Magnetic Bearings for High Speed Machining – Conditions and Benefits. In: *TEHNOMUS XVII*; May 2013; Suceava, Romania. 2013. p. 13–20.
- [25] Schweitzer G.. Active magnetic bearings-chances and limitations. In: *6th Int. Conf. Rotor Dyn.*; Elsevier Ltd., Australia; 2002.
- [26] Clark D.J., Jansen M.J., Montague G.T.. An Overview of Magnetic Bearing Technology for Gas Turbine Engines . *NASA Technical Report*. 2004;NASA/TM-2004-213177
- [27] Cappellino C.A., Osborne J.C.. The Prediction of Bearing Lubricant Temperatures and Cooling Requirements for a Centrifugal Pump. In: *Proc. Second Int. Pump Symp.*; April 1985; Houston, Texas. 1985. p. 77-84.
- [28] Ghosh M., Majumdar B., Sarangi M. . *Theory of Lubrication* New Delhi: Tata McGraw-Hill; 2013.
- [29] DellaCorte C., Lukaszewicz V., Valco M.J., Radil K.C., Heshmat H.. Performance and Durability of High Temperature Foil Air Bearings for Oil-Free Turbomachinery. *Tribol. Trans.*. 2000;43:774–780.
- [30] Venkatesh V. *Precision Engineering* Tata McGraw-Hill Education; 2007.
- [31] Hamrock B.J., Anderson W.J.. *Rolling-Element Bearings*. NASA Reference Publication. 1983;NASA RP-1105(February 2011):1-58.
- [32] Pope J.E.. *Rules of thumb for mechanical engineers*. Houston, Texas: Gulf Publishing Company; 1997.
- [33] Tanimoto K., Ikeda T.. Evaluation of extra-small ceramic ball bearings. *KOYO Engineering Journal English Edition*. 2000;156(E):23-29.
- [34] Powell J.. *Design of aerostatic bearings* Brighton, U.K.: The Machinery Publishing Co.; 1970.
- [35] DellaCorte C., Valco M.J.. Load Capacity Estimation of Foil Air Journal Bearings for Oil-Free Turbomachinery Applications. *STLE Tribology Transaction*. 2000;43(4):795–801.
- [36] Radil K.C., DellaCorte C.. Foil Bearing Starting Considerations and Requirements for Rotorcraft Engine Applications. *Army Research Laboratory Technical Report*. 2009;ARL-TR-4873:1-14.

- [37] DellaCorte C., Radil K.. A Preliminary Foil Gas Bearing Performance Map. NASA Technical Report. 2006;NASA/TM-2006-214343 :1-16.
- [38] Cunningham R.E., Fleming D.P., Anderson W.J.. Experiments of stability of Herringbone-grooved gas lubricated journal bearings to high compressibility numbers. NASA Technical Note. 1968;NASA TN D-4440:1-20.
- [39] Reitsma T.W.. Lifting off friction [Internet]. September 1, 2006. Available from: <http://machinedesign.com/archive/lifting-friction>
- [40] Montague G., Jansen M., Provenza A., Jansen R., Ebihara B., Palazzolo A.. Room Temperature Characterization of a Magnetic Bearing for Turbomachinery. NASA Technical Report. 2002;NASA/TM—2002-211904:1-9.
- [41] Montague G., Jansen M., Provenza A., Palazzolo A., Jansen R., Ebihara B.. Experimental High Temperature Characterization of a Magnetic Bearing for Turbomachinery. NASA Technical Report. 2003;NASA/TM—2003-212183:1-12.
- [42] Paden B., Groom N., Antaki J.F.. Design Formulas for Permanent-Magnet Bearings. ASME Journal of Mechanical Design. 2003;125:734-738.
- [43] Capstone Turbine, Advanced MicroTurbine System (AMTS) - C200 MicroTurbine - Ultra-Low Emissions MicroTurbine, DOE Project ID # DE-FC26-00CH11058.
- [44] K. Ashihara, A. Goto, S. Guo , H. Okamoto, Optimization of Microturbine Aerodynamic Using CFD, Inverse Design and FEM Structural Analysis. ASME Paper,GT-2004-53431, 2004
- [45] C. S. Smugeresky, An Integrated Combined Heat and Power Distributed Energy Resource Solution for Modular Applications. ASME Paper GT-2007-28294, 2007
- [46] Mueller, L., Alsalihi, Z., Verstraete, T., 2013, "Multidisciplinary Optimization of a Turbocharger Radial Turbine", Journal of Turbomachinery, Volume 135
- [47] Pierret S., Demeulenaere A., Gouverneura B., Hirsch C.,2001, "A flexible and automatic design environment applied to the optimization of turbomachinery blades", ISABE Paper No. 2001-1054
- [48] Verstraete, T., Alsalihi, Z., Van den Braembussche R., 2010, "Multidisciplinary Optimization of a Radial Compressor for Microgas Turbine Applications", Journal of Turbomachinery, Volume 132
- [49] Vavra, M. H., 1974, "Aero-Thermodynamics and Flow in Turbomachines", Robert E. Krieger Publishing Company
- [50] Cumpsty, N., 2004, "Compressor aerodynamics", Krieger Publishing Company
- [51] Baskharone, E. A., 2006, "Principles of Turbomachinery in Air Breathing Engines", Cambridge University Press
- [52] Deng,Q, Niu, J., Mao, J, FENG, Z., 2007, "Experimental and numerical investigation on overall performance of a radial inflow turbine for 100 kW microturbine", ASME Turbo Expo GT2007-27707
- [53] R. A. Miranda Carrillo, R. A., Nascimento, M. A. R., Gutiérrez Velásquez, E. I., Moura, N. R., 2010, "Radial inflow turbine one and tridimensional design analysis of a 600 kW simple cycle gas turbine engine", ASME Turbo ExpoGT2010-22951
- [54] Rodgers, C., 2012, "Aerothermodynamic development of a 70 kW microturbine", ASME Turbo ExpoGT2012-68195
- [55] Whitfield, A., Baines, N.C., Design of Radial Turbomachines, Pearson Education Limited, 1990.

- [56] Fu, L., Shi, Y., DENG, Q., Li, H., Feng, Z., 2011, "Integrated Optimization Design for a Radial Turbine Wheel of a 100kW-Class Microturbine", ASME Turbo ExpoGT2011-46140
- [57] Xu, D., Deng, Q., Feng, Z., 2011, "Numerical Investigation on Rotor Tip Leakage Control by Casing Air Injection for a Radial Inflow Turbine", ASME Turbo ExpoGT2011-46123
- [58] Meitner, P. L., Glassman, A. J., 1980, "Off-Design Performance Loss Model for Radial Turbines With Pivoting, Variable-Area Stators", NASA Technical Paper 1708
- [59] Kofskey, M. G., Nusbaum, W. J., 1971, "Effects of specific speed on the experimental performance of a radial-inflow turbine", NASA technical note D-6182
- [60] Frigne, P., Van Den Braembussche, R., 1979, "One dimensional design of centrifugal compressors taking into account flow separation in the impeller", VKI Technical note 129
- [61] NUMECA, User's manual, academic R&D license 2014
- [62] [www.calculix.de](http://www.calculix.de)
- [63] Pierret S., Demeulenaere A., Gouverneur B., Hirsch C., Van den Braembussche R., 2000, "Designing turbomachinery blades with the function approximation concept and the Navier-Stokes equations", AIAA Paper No. 2000-4879
- [64] Demeulenaere A., Pierret S., Hirsch C., 2003, "An integrated optimization system for turbomachinery blades", Eurogen2003, 5th Conference on Evolutionary Methods for Design, Optimization, Control with Applications to Industrial and Societal Problems
- [65] Demeulenaere A., Purwanto A., Ligout A., Hirsch C., Dijkers R., Visser F., 2005, "Design and optimization of an industrial pump: application of genetic algorithms and neural network", ASME FEDSM Paper No. 2005-77487
- [66] Kueny J.L., Lestriez R., Helali A., Hirsch C., 2004, "Optimal design of a small hydraulic turbine", 22nd IAHR Symposium on Hydraulic Machinery and Systems, Stockholm, Sweden
- [67] Reising S., Font Brossa J., Schiffer H.P., 2009, "CFD analysis of hub-corner stall and secondary flow in a transonic compressor stage with non-axisymmetric end wall", 8th European Turbomachinery Conference, Graz, Austria
- [68] Demeulenaere A., Ligout A., Hirsch C., 2004, "Application of multipoint optimization to the design of turbomachinery blades", ASME GT Paper No. 2004-52110
- [69] Barsi, D., Costa, C., Cravero, C., Ricci, G., 2014, "Aerodynamic design of a centrifugal compressor stage using an automatic optimization strategy", ASME paper No. GT2014-26456
- [70] Geuzaine, C., Remacle, J. F., 2009, "Gmsh: a three-dimensional finite element mesh generator with built-in pre- and post-processing facilities", International Journal for Numerical Methods in Engineering, Volume 79, Issue 11, pages 1309-1331.
- [71] [www.geuz.org/gmsh/](http://www.geuz.org/gmsh/)
- [72] Honisch, P., Kuhhorn, A., Beirow, B., 2011, "Experimental and Numerical Analyses of Radial Turbine Blisks with regard to Mistuning", GT2011-45359, Proceedings of ASME Turbo Expo 2011, June 6-10, 2011, Vancouver, British Columbia, Canada.
- [73] Singh, M.P., Vargo, J.J., Schiffer, D.M., and Dello, J.D., 2000, "SAFE Diagram – A Design and Reliability Tool for Turbine Blading," Technical Paper 024, Dresser-Rand Company.

- [74] Singh, M.P., 2000, "SAFE Diagram – A Dresser-Rand Evaluation Tool for Packeted Bladed Disc Assembly," Technical Paper 025, Dresser-Rand Company.
- [75] Kushner, F., Richard, S.J., and Strickland, R.A., 2000, "Critical Review of Compressor Impeller Vibration Parameters for Failure Prevention," Proceedings of the 29th Turbomachinery Symposium, Turbomachinery Laboratory, Texas A&M University
- [76] Carnö, Johanna, Adrin Cavani, and Leif Liinanki. "Micro gas turbine for combined heat and power in distributed generation." ASME 1998 International Gas Turbine and Aeroengine Congress and Exhibition. American Society of Mechanical Engineers, 1998.
- [77] Dickmann, H., Secall Wimmel, T., Szwedowicz, J., Filsinger, D., Roduner, C., "Unsteady flow in a turbocharger centrifugal compressor: Three-dimensional computational fluid dynamics simulation and numerical and experimental analysis of impeller blade vibration." *Journal of Turbomachinery* 128.3 (2006): 455-465.
- [78] Trébinjac, I., Kulisa, P., Bulot, N., Rochuon, N., "Effect of unsteadiness on the performance of a transonic centrifugal compressor stage." *Journal of Turbomachinery* 131.4 (2009): 041011.
- [79] Came, P. M., C. J. Robinson. "Centrifugal compressor design." *Proceedings of the Institution of Mechanical Engineers, Part C: Journal of Mechanical Engineering Science* 213.2 (1998): 139-155.
- [80] Ibaraki, Seiichi, "Aerodynamics of a transonic centrifugal compressor impeller." *ASME Turbo Expo 2002: Power for Land, Sea, and Air*. American Society of Mechanical Engineers, 2002.
- [81] Ma, Y., "Improved centrifugal compressor impeller optimization with a radial basis function network and principle component analysis." *Proceedings of the institution of mechanical engineers, Part C: Journal of mechanical engineering science* 224.4 (2010): 935-945.
- [82] Shibata, Takanori, et al. "Performance improvement of a centrifugal compressor stage by increasing degree of reaction and optimizing blade loading of a 3D impeller." *Journal of Turbomachinery* 133.2 (2011): 021004.
- [83] Wang, X. F., Guang Xi, and Z. H. Wang. "Aerodynamic optimization design of centrifugal compressor's impeller with Kriging model." *Proceedings of the institution of mechanical engineers, Part A: Journal of power and energy* 220.6 (2006): 589-597.
- [84] Kim, J. H., et al. "Multi-objective optimization of a centrifugal compressor impeller through evolutionary algorithms." *Proceedings of the Institution of Mechanical Engineers, Part A: Journal of Power and Energy* 224.5 (2010): 711-721.
- [85] Benini, Ernesto. "Three-dimensional multi-objective design optimization of a transonic compressor rotor." *Journal of Propulsion and Power* 20.3 (2004): 559-565.
- [86] Pierret, Stéphane, and R. A. Van den Braembussche. "Turbomachinery blade design using a Navier-Stokes solver and artificial neural network." *ASME 1998 International Gas Turbine and Aeroengine Congress and Exhibition*. American Society of Mechanical Engineers, 1998.
- [87] Ashihara, Kosuke, et al. "Optimization of Microturbine Aerodynamics Using CFD, Inverse Design and FEM Structural Analysis: 1st Report—Compressor Design." *ASME Turbo Expo 2004: Power for Land, Sea, and Air*. American Society of Mechanical Engineers, 2004.

- [88] Barsi, D., Perrone, A., Ratto, L., Simoni, D., Zunino, P., "Radial Inflow Turbine Design Through Multi-Disciplinary Optimization Technique." ASME Turbo Expo 2015: Turbine Technical Conference and Exposition. American Society of Mechanical Engineers, 2015.
- [89] Mueller, L., Alsalihi, Z., Verstraete, T., "Multidisciplinary optimization of a turbocharger radial turbine." Journal of Turbomachinery 135.2 (2013): 021022.
- [90] T. Verstraete, Z. Alsalihi, R.A. Van den Braembussche 2010, "Multidisciplinary Optimization of a Radial Compressor for Microgas Turbine Applications", Journal of Turbomachinery, Volume 132.
- [91] Vavra M. H., "Basic elements for advanced designs of radial flow compressors", AGARD Lecture Series No 39, 1970.
- [92] Higashimori, H., Hasagawa, K., Sumida, K., & Suita, T. (2004, January). Detailed flow study of Mach number 1.6 high transonic flow with a shock wave in a pressure ratio 11 centrifugal compressor impeller. In ASME Turbo Expo 2004: Power for Land, Sea, and Air (pp. 771-779). American Society of Mechanical Engineers.
- [93] Stanitz J. D., "Some Theoretical Aerodynamic Investigations of Impellers in Radial and Mixed-Flow Centrifugal Compressors", TRANS. ASME, vol. 74(4), pp.473-497, 1952
- [94] NUMECA, User manuals. Academic R&D license 2015.
- [95] Hirsch C., Lacor C., Rizzi A., Eliasson P., Lindblad I. and Haeuser J., "A multiblock/multigrid code for the efficient solution of complex 3D Navier-Stokes flows", Aerothermodynamics for Space Vehicles 1, pp. 415-420, SEE N92-14973 06-02, 1991
- [96] Bourgeois JA, Martinuzzi RJ, Savory E, Zhang C, Roberts DA. Assessment of Turbulence Model Predictions for an Aero-Engine Centrifugal Compressor. ASME. J. Turbomach. 2010, 133(1).
- [97] Mangani L, Casartelli E, Mauri S. Assessment of Various Turbulence Models in a High Pressure Ratio Centrifugal Compressor With an Object Oriented CFD Code. ASME. J. Turbomach. 2012, 134(6).
- [98] R.A. Van den Braembussche, J. Prinsier, A. Di Sante, Experimental and numerical investigation of the flow in rotating diverging channels, Journal of Thermal Science. Volume 19, Issue 2, 115-119.
- [99] C. Geuzaine and J.-F. Remacle, 2009, "*Gmsh: a three-dimensional finite element mesh generator with built-in pre- and post-processing facilities*", International Journal for Numerical Methods in Engineering, Volume 79, Issue 11, pages 1309-1331.
- [100] J.-F. Remacle, C. Geuzaine, G. Compère and E. Marchandise, "High-quality surface remeshing using harmonic maps". International Journal for Numerical Methods in Engineering 83(4), pp. 403-425, 2010.
- [101] Singh, M.P., Vargo, J.J., Schiffer, D.M., and Dello, J.D., 2000, "SAFE Diagram – A Design and Reliability Tool for Turbine Blading," Technical Paper 024, Dresser-Rand Company.
- [102] Singh, M.P., 2000, "SAFE Diagram – A Dresser-Rand Evaluation Tool for Packeted Bladed Disc Assembly," Technical Paper 025, Dresser-Rand Company.
- [103] Honisch, P., Kuhhorn, A., Beirow, B., 2011, "Experimental and Numerical Analyses of Radial Turbine Blisks with regard to Mistuning", GT2011-45359,

Proceedings of ASME Turbo Expo 2011, June 6-10, 2011, Vancouver, British Columbia, Canada.

- [104] Guido Dhondt, "CalculiX CrunchiX User's manual v2.9", November 2015.
- [105] Pierret, S., Demeulenaere, A., Gouverneur, B., Hirsch, C., & Van den Braembussche, R. (2000). Designing turbomachinery blades with the function approximation concept and the navier-stokes equations. AIAA paper, 4879.
- [106] Krain, H., G. Karpinski, and M. Beversdorff. "Flow analysis in a transonic centrifugal compressor rotor using 3-component laser velocimetry." ASME Turbo Expo 2001: Power for Land, Sea, and Air. American Society of Mechanical Engineers, 2001.
- [107] Marconcini, M., Rubecchini, F., Arnone, A., & Ibaraki, S. (2010). Numerical analysis of the vaned diffuser of a transonic centrifugal compressor. Journal of Turbomachinery, 132(4), 041012.